Holographic recording and dynamic range improvement in lithium niobate crystals

Thesis by

Yunping Yang

In Partial Fulfillment of the Requirements

for the Degree of

Doctor of Philosophy

California Institute of Technology

Pasadena, California

2003

(Defended June 27, 2002)

Acknowledgments

First, I would like to express my most sincere appreciation to my advisor, Prof. Demetri Psaltis, for his support of my research as well as expert guidance on the direction and goals of my research. I am very grateful to him for his patience and encouragement when I struggled, and his enthusiasm with my gradual accomplishments over the years of my work in his group. Undoubtedly, none of the results in this thesis would have been possible without his guidance and support.

I am greatly indebted to Prof. Karsten Buse, who has been guiding and collaborating with me for the past three years. I could not have accomplished this without his help and guidance. His extensive knowledge and deep insights into photorefractive phenomena have been my resources and the collaborations and discussions with him have always been productive and enjoyable. I would like to thank Prof. Ali Adibi for his collaborations and discussions on the comparison of the 90-degree and transmission geometries. I also owe thanks to Dr. Ingoo Nee for many helpful discussions on the dark decay mechanisms when he was in this group as a visiting student and Marc Lünnemann, Dirk Berben, Ulrich Hartwig for conducting some experiments on $LiNbO_3$:Mn.

For technical support in keeping the labs running and equipment in fine condition for my experiments, I would like to thank Ya-yun Liu. I also owe thanks to Lucinda Acosta for her enthusiastically assisting with administrative matters.

I'd like to thank all of the Psaltis group members, past and present, for helping to create a professional and stimulating research environment. These include Dr. George Barbastathis, Dr. Greg Billock, Dr. Ernest Chuang, Emmanouil-Panagiotis Fitrakis, Vijay Gupta, Dr. Michael Levene, Dr. Wenhai Liu, Dr. Zhiwen Liu, Zhenyu Li, Hua Long, Irena Maravic, Todd Meyrath, Dr. Chris Moser, Dr. Jose Mumbru, George Panotopoulos, Dr. Allen Pu, Dimitris Sakellariou, Dr. Xu Wang, and anyone else I might have unintentionally missed. I would like to give special thanks to Dr. Xin An for helping me in getting integrated into the group during my first several months at Caltech and teaching me many of the skills necessary to carry out sophisticated experiments in the labs.

I would like to thank all the members of Buse group at Bonn University in Germany for their friendship and helps that made my stay in Germany as a visiting student easier and more enjoyable. These include Dr. Akos Hoffmann, Dr. Elisabeth Soergel, Raja Bernard, Nils Benter, Ralph Bertram, Manfred Müller, Johannes Spanier, Marc Lünnemann, Dirk Berben, and Ulrich Hartwig.

I want to thank my parents for their continued encouragement through all the years of my education. I would like to convey my deep appreciation to my wife, Xiaoling, for her years of patience and understanding while I was off working long hours in the labs. Her unwavering support and love have been a tremendous motivation for me.

Abstract

This thesis presents the results of research centered on the topic of improvement of dynamic range and sensitivity in volume holographic recording using photorefractive lithium niobate ($LiNbO_3$) crystals. The dynamic range (M/#) is one of the most important system metrics for holographic storage systems. The larger the M/#, the higher the storage capacity and the better system performances for holographic memories. In general, there are two approaches to improving the dynamic range. One is at system level, for example, in $LiNbO_3$:Fe-based holographic storage system by using transmission geometry instead of the 90-degree geometry, we can boost the M/# by a factor of 10. The other approach is at material level. For $LiNbO_3$-based holographic memories, the most important material parameters are dopant and doping level. Usually, the higher the doping level, the larger the M/#. However, there is a limit on the highest practical doping level in $LiNbO_3$:Fe and the limiting factor is dark decay due to electron tunneling. By using deeper center than Fe, e.g., Mn, the effect of electron tunneling is much smaller and we can use higher doping levels and obtain larger M/#.

The second chapter compares the system performances of two holographic recording geometries (the 90-degree and transmission geometries) using iron-doped lithium niobate. The comparison is based on dynamic range (M/#), sensitivity, scattering noise, inter-pixel noise, and storage capacity. The M/# and sensitivity are larger in transmission geometry than those in the 90-degree geometry. The measured M/# and sensitivity of transmission geometry are 10 times as large as those of the 90-degree geometry for $LiNbO_3$:Fe crystals with almost same doping levels and oxidation states available in our labs. Although the scattering noise level in transmission geometry is larger, considering the remarkable gain in the M/#, the signal to scattering noise ratio (SSNR) in transmission geometry is better than that in the 90-degree geometry. The inter-pixel noises of the 90-degree and transmission geometries are comparable. Although the angular selectivity in the 90-degree geometry is higher, for dynamic range limited holographic storage systems, transmission geometry has higher capacity than the 90-degree geometry.

The third chapter investigates dark decay mechanisms in lithium niobate crystals. Two mechanisms of the dark decay, proton compensation and electron tunneling with activation energies of 1.0 eV and 0.28 eV, respectively, are identified. In crystals with doping levels less than 0.05 wt% Fe_2O_3, proton compensation dominates the dark decay and extrapolation of lifetimes by an Arrhenius law to room temperature is valid. The time constant of this type of dark decay is inversely proportional to the proton concentration. For crystals with doping levels as high as 0.25 wt% Fe_2O_3, electron tunneling dominates the dark decay. This type of dark decay also limits the highest practical doping level in $LiNbO_3$ crystals. For crystals with medium doping levels, e.g., between 0.05 and 0.25 wt% Fe_2O_3, both proton compensation and electron tunneling contribute significantly to the dark decay, and the single Arrhenius law does not hold with a single activation energy.

In the fourth chapter, holographic data storage experiments are performed using manganese-doped lithium niobate crystals. The idea to use manganese-doped lithium niobate crystals for holographic storage is the direct result of the understanding of dark decay mechanisms discussed in Chapter 3. The experimental results of dark decay, M/#, sensitivity, multiplexing, thermal fixing, and holographic scattering for $LiNbO_3$: 0.2 atomic% Mn and $LiNbO_3$: 0.5 wt% $MnCO_3$ are presented. The experimental results show that manganese-doped lithium niobate crystals are well suited for holographic storage.

In the final chapter attention is focused on photorefractive properties of manganese-doped lithium niobate crystals. Material parameters, such as the distribution coefficient, are determined. Absorption measurements are used to obtain some information about several charge transport parameters. The dynamic range(M/#) and sensitivity for crystals of different doping levels, different oxidation states, and for different light polarizations have been measured.

Table of Contents

List of Figures

CHAPTER 1 Introduction

CHAPTER 2 Comparison of the 90-degree and transmission geometry

CHAPTER 3 Dark decay mechanisms in lithium niobate crystals

CHAPTER 4 Holographic storage using manganese-doped lithium niobate crystals

CHAPTER 5 Charge transport model for manganese-doped lithium niobate crystals

List of Tables

1 Introduction

1.1 Holography

Holography was first invented by Dennis Gabor in 1948,[1-1] when he proposed an approach to record and retrieve a wavefront in a manner that preserved both the phase and amplitude information of the original wave. The basic idea of holography is that when two coherent beams of light, of which one is called reference beam, the other is called signal beam, interfere with each other, the resulting intensity of interference pattern contains both the amplitude and phase information of the two beams. By placing an appropriate photorefractive material at the point of interference, the intensity of the interference pattern can be recorded inside the material. This recorded grating is referred to as a hologram. Subsequently illuminated by the same reference beam which was used for recording, the hologram causes light to be diffracted in the direction of the signal beam containing both the amplitude and phase information of that original signal beam.

In the early stages of research on holography Gabor and others used in-line holograms, which meant that both real and virtual image components were reconstructed simultaneously and along the same direction as the transmitted reference beam.[1-2]-[1-4] This resulted in poor image fidelity of the reconstructed signal beam. The invention of the laser and an off-axis technique gave a huge boost to holography in the early 1960's. In 1962 Leith and Upatnieks realized that holography could be used as a 3-D visual medium. They significantly improved upon Gabor's original idea of holography by using laser and the off-

axis technique, whereby the interfering beams were angularly offset to allow the various diffracted components of the output light to be spatially separated, resulting in the first laser transmission hologram of 3-D objects with good reconstruction quality.[1-5][1-6]

1.2 Volume holographic storage

The material used in most early experiments in holography was photographic film, which is typically a thin, two-dimensional layer of recording material.[1-7][1-8] The holograms recorded inside photographic film were essentially planar, and thus lacked sensitivity to changes in the angle of the reconstruction beam. The development of 3-dimensional volume holography in 1962 by Denisyuk improved the quality of the reconstructed images by taking advantage of Bragg effects to attenuate the unwanted conjugate component of the reconstructed image.[1-9][1-10] Also, because the interference pattern is recorded throughout the whole volume of the storage material, volume holograms are sensitive to changes in the propagation properties of the readout beam, which makes it possible to record multiple holograms within the same volume of material. Unlike in planar holograms, wave-coupling effects must be considered for volume holograms. Kogelnik first developed the coupled-wave theory for volume holograms in 1969, predicting diffraction efficiency and Bragg selectivity for thick gratings.[1-11] Later analysis examined the theory applied to the regime between thick and thin holograms.[1-12][1-13] Using the Bragg selectivity inherent to volume holography, multiple holograms can be stored and retrieved independently in the same volume by changing the propagation properties of the reference beam. As a result, the information storage capacity is greatly increased by volume holography. Van Heerden examined the potential storage capacity of holography and found the theoretical limit to be

on the order of V/λ^3, where V is the volume of the recording medium and λ is the wavelength of light.[1-14] In addition to the promise of massive storage capacity, holographic memories also held the attraction of a potential data transfer rate of the order of gigabits per second with page access.

In spite of the potential massive storage capacity and high date transfer rate, the lack of efficient input and readout devices at the time, as well as the problem of obtaining appropriate lasers, made it difficult to achieve a practical holographic storage system. Although storage capacities as high as 500 holograms were demonstrated in some early work on holographic storage,[1-15]-[1-18] it was not until the development of more advanced components, such as lasers, detectors, and liquid crystal spatial light modulators, that more ambitious projects were taken. Recently, demonstrations of storing and retrieving many thousands of holograms in lithium niobate crystals have been performed.[1-19]-[1-21] Much of the progress can be attributed to advancements in our understanding of ways to take advantage of the Bragg selectivity of 3-D recording to multiplex holograms, as well as continued research in holographic material properties and dynamics.

1.3 Multiplexing techniques

For volume holograms, the reconstructed signal beam on readout is highly sensitive to the changes of propagation properties in the readout beam. If the reference beam is modified sufficiently, the diffracted light contributions from different portion of the grating volume will lead to destructive interference effect and the diffraction from previously recorded holograms will be attenuated to zero. Then a new hologram can be written in the same volume of recording medium with the new reference beam. Multiplexing techniques

based on phase mismatches between the diffracted light contributions from different portions of volume hologram include angle,[1-22] wavelength,[1-23]-[1-27] phase code,[1-28]-[1-34] and shift multiplexing.[1-35] There is another class of multiplexing techniques, by which more than one hologram can be accessed by the same reference beam. The reconstructions from the same reference beam do not overlap in spatial frequencies, so the undesired ones can be eliminated by spatial filtering. These techniques include fractal[1-36][1-37] and peristrophic multiplexing.[1-38] By combining several multiplexing techniques, thousands of holograms can be multiplexed in the same volume of recording material. For example, angle and fractal multiplexing techniques were used to record 10,000 holograms at the same location of one lithium niobate crystal.[1-39] Considering all the available multiplexing techniques, it is easy to find a combination to meet the demand of multiplexing for most large-scale holographic storage systems. This makes the issue of improvement of dynamic range of recording material more important.

1.4 Photorefractive materials: Dynamic range

The two commonly used storage material are polymer films[1-40]-[1-42] and photorefractive crystals. Most polymers are suited for read-only memories (ROM) or write-once-read-many (WORM) systems. The potential of photorefractive crystals as holographic recording materials has been investigated since the early 1960's. Typical photorefractive materials include lithium niobate ($LiNbO_3$),[1-43][1-44] barium titanate ($BaTiO_3$) [1-45][1-46] and strontium barium niobate (SBN).[1-47][1-48] A considerable amount of research has been conducted in analyzing the dynamics of the grating formation in photo-

refractive materials. The most widely accepted is the one-center band transport model developed by Kukhtarev.[1-49][1-50]

For saturable recording materials, the grating strength A of a hologram as it is recorded grows exponentially as

$$A(t) = A_0\left[1 - \exp\left(-\frac{t}{\tau_w}\right)\right], \tag{1-1}$$

where A_0 is the saturation grating strength and τ_w is the writing time constant. The holograms decay under illumination as

$$A(t) = A_i \exp\left(-\frac{t}{\tau_e}\right), \tag{1-2}$$

where A_i is the initial amplitude of the grating when erasure begins and τ_e is the erasure time constant. We often use M/#, which is defined as

$$M/\# \equiv \frac{A_0}{\tau_r} \times \tau_e, \tag{1-3}$$

as a figure-of-merit for the dynamic range of a particular holographic storage system.[1-51] By using appropriate exposure schedule, the diffraction efficiencies of the multiplexed holograms can be equalized with diffraction efficiency η given by

$$\eta = \left(\frac{M/\#}{M}\right)^2, \tag{1-4}$$

where M is the number of holograms multiplexed. Given the diffraction efficiency η, the larger the M/#, the more holograms we may store in the recording material. It is always desirable to have large M/#.

1.5 Thesis overview

This thesis presents the results of research centered on the topic of improvement of dynamic range in volume holographic recording using photorefractive lithium niobate ($LiNbO_3$) crystals. The dynamic range (M/#) is one of the most important system metrics for holographic storage system. The larger the M/#, the higher the storage capacity and the better system performance for holographic memories. In general, there are two approaches to improving the dynamic range. One is at system level, for example, in $LiNbO_3$:Fe-based holographic storage system by using transmission geometry instead of the 90-degree geometry, we can boost the M/# by a factor of 10. The other approach is at material level. For $LiNbO_3$-based holographic memories, the most important material parameters are dopant and doping level. Usually, the higher the doping level, the larger the M/#. However, there is a limit on the highest practical doping level for $LiNbO_3$:Fe and the limiting factor is dark decay due to electron tunneling. By using deeper center than Fe, e.g., Mn, the effect of electron tunneling is much smaller and we can use higher doping levels and obtain larger M/#.

The second chapter compares the system performances of two holographic recording geometries (the 90-degree and transmission geometries) using iron-doped lithium niobate. The comparison is based on dynamic range (M/#), sensitivity, scattering noise, interpixel noise, and storage capacity. The M/# and sensitivity are larger in transmission geometry than those in the 90-degree geometry. The measured M/# and sensitivity of transmission geometry are 10 times as large as those of the 90-degree geometry for $LiNbO_3$:Fe crystals with almost same doping levels and oxidation states available in our labs. Although the scattering noise level in transmission geometry is larger, considering the remarkable gain in the M/#, the signal to scattering noise ratio (SSNR) is better in transmission geom-

etry than that in the 90-degree geometry. The inter-pixel noises of the 90-degree and transmission geometries are comparable. Although the angular selectivity in the 90-degree geometry is higher, for dynamic range limited holographic storage system, transmission geometry has higher capacity than the 90-degree geometry.

The third chapter investigates dark decay mechanisms in lithium niobate crystals. Two mechanisms of the dark decay, proton compensation and electron tunneling with activation energies of 1.0 eV and 0.28 eV, respectively, are identified. In crystals with doping levels less than 0.05 wt% Fe_2O_3, proton compensation dominates the dark decay and extrapolation of lifetimes by an Arrhenius law to room temperature is valid. The time constant of this type of dark decay is inversely proportional to the proton concentration. For crystals with doping levels as high as 0.25 wt% Fe_2O_3, electron tunneling dominates the dark decay. This type of dark decay also limits the highest practical doping level in $LiNbO_3$ crystals. For crystals with medium doping levels, e.g., between 0.05 and 0.25 wt% Fe_2O_3, both proton compensation and electron tunneling contribute significantly to the dark decay, and the single Arrhenius law does not hold with a single activation energy.

In the fourth chapter, holographic data storage experiments are performed using manganese-doped lithium niobate crystals. The idea to use manganese-doped lithium niobate crystals for holographic storage is the direct result of the understanding of dark decay mechanisms discussed in Chapter 3. The experimental results of dark decay, sensitivity, M/#, multiplexing, thermal fixing, and holographic scattering for lithium niobate crystals doped with 0.2 atomic% Mn and lithium niobate crystals doped with 0.5 wt% $MnCO_3$ are presented. The experimental results show that manganese-doped lithium niobate crystals are well suited for holographic storage.

In the final chapter attention is focused on photorefractive properties of manganese-doped lithium niobate crystals. Material parameters, such as the distribution coefficient, are determined. Absorption measurements are used to obtain some information about several charge transport parameters. The dynamic range(M/#) and sensitivity for crystals of different doping levels, different oxidation states, and for different light polarizations have been measured.

References

[1-1] D. Gabor, "A new microscope principle," Nature **161**, 777-778 (1948).

[1-2] D. Gabor, "Microscopy by reconstructed wavefronts," Proceeding of the Royal Society **A 197**, 454-487 (1949).

[1-3] G. L. Rogers, "Gabor diffraction microscopy," Nature **166**, 237 (1950).

[1-4] A. Lohmann, "Optical single-sideband transmission applied to the Gabor microscope," Optical Acta **3**, 97-103 (1956).

[1-5] E. N. Leith and J. Upatnieks, "Reconstructed wavefronts and communication theory," J. Opt. Soc. Am. **52**, 1123-1130 (1962).

[1-6] E. N. Leith and J. Upatnieks, "Wavefront reconstruction with diffused illumination and three-dimensional objects," J. Opt. Soc. Am. **54**, 1295-1301 (1964).

[1-7] R. F. van Ligten, "Influence of photographic film on wavefront reconstruction. I: Plane wavefronts," J. Opt. Soc. Am. **56**, 1-7 (1966).

[1-8] J. W. Goodman, "Effects of film nonlinearities in holography," J. Opt. Soc. Am. **57**, 560-564 (1967).

[1-9] Y. N. Denisyuk, "Photographic reconstruction of the optical properties of an object in its own scattered radiation field," Sov. Phys. Dokl. **7**, 543 (1962).

[1-10] W. L. Bragg, "The X-ray microscope," Nature **149**, 470-475 (1942).

[1-11] H. Kogelnik, "Coupled wave theory for thick hologram gratings," Bell Sys. Tech. J. **48**, 2909-2945 (1969).

[1-12] B. Benlarbi, D. J. Cooke, and L. Solymar, "Higher order modes in thick phase gratings," Optica Acta **27**, 885-895 (1980).

[1-13] M. G. Moharam, T. K. Gaylord, and R. Magnusson, "Diffraction characteristics of three-dimensional crossed-beam volume gratings," J. Opt. Soc. Am. **70**, 437-442 (1980).

[1-14] P. J. van Heerden, "Theory of optical information storage in solids," Appl. Opt. **2**, 393-400 (1963).

[1-15] F. S. Chen, J. T. LaMacchia, and D. B. Fraser, "Holographic storage in lithium niobate," Appl. Phys. Lett. **13**, 223-225 (1968).

[1-16] J. J. Amodei and D. L. Staebler, "Holographic recording in lithium niobate," RCA Review **33**, 71-93 (1972).

[1-17] D. L. Staebler, J. J. Amodei, and W. Philips, "Multiple storage of thick phase holograms in $LiNbO_3$," IEEE J. of Quan. Elect. **QE 8**, 611 (1972).

[1-18] D. L. Staebler, W. J. Burke, W. Philips, and J. J. Amodei, "Multiple storage and erasure of fixed holograms in Fe-doped $LiNbO_3$," Appl. Phys. Lett. **26**, 182-184 (1975).

[1-19] F. H. Mok, "Angle-multiplexed storage of 5000 holograms in lithium niobate," Opt. Lett. **18**, 915-917 (1991).

[1-20] G. W. Burr, F. H. Mok, and D. Psaltis, "Angle and space multiplexed holographic storage using the 90-degree geometry," Opt. Comm. **117**, 49-55 (1995).

[1-21] X. An, D. Psaltis, and G. W. Burr, "Thermal fixing of 10,000 holograms in $LiNbO_3$: Fe," Appl. Opt. **38**, 386-393 (1999).

[1-22] P. J. van Heerden, "A new optical method of storing and retrieving information," Appl. Opt. **2**, 387-392 (1963).

[1-23] F. T. S. Yu, S. Wu, A. W. Mayers, and S. Rajan, "Wavelength multiplexed reflection matched spatial filters using $LiNbO_3$," Opt. Comm. **81**, 343-347 (1991).

[1-24] G. A. Rakuljic, V. Leyva, and A. Yariv, "Optical data storage by using orthogonal wavelength-multiplexed volume holograms," Opt. Lett. **17**, 1471-1473 (1992).

[1-25] J. Rosen, M. Segev, and A. Yariv, "Wavelength-multiplexed computer-generated volume holography," Opt. Lett. **18**, 744-746 (1993).

[1-26] S. Yin, H. Zhou, F. Zhao, M. Wen, Z. Zhang, and F. T. S. Yu, "Wavelength-multiplexed holographic storage in a sensitive photorefractive crystal using a visible-light tunable diode laser," Opt. Comm. **101** (1993).

[1-27] F. Zhao, H. Zhou, S. Yin, and F. T. S. Yu, "Wavelength-multiplexed holographic storage by using the minimum wavelength channel separation in a photorefractive crystal fiber," Opt. Comm. **103** (1993).

[1-28] J. T. LaMacchia and D. L. White, "Coded multiple exposure holograms," Appl. Opt. **7**, 91-94 (1977).

[1-29] T. F. Krile, M. O. Hagler, W. D. Redus, and J. F. Walkup, "Multiplex holography with chirp-modulated binary phase-coded reference-beam masks," Appl. Opt. **18**, 52-56 (1979).

[1-30] J. E. Ford, Y. Fainman, and S. H. Lee, "Array interconnection by phase-coded optical correlation," Opt. Lett. **15**, 1088-1090 (1990).

[1-31] C. Denz, G. Pauliat, G. Roosen, and T. Tschudi, "Volume hologram multiplexing using a deterministic phase encoding method," Opt. Comm. **85**, 171-176 (1991).

[1-32] C. Alves, G. Pauliat, and G. Roosen, "Dynamic phase-encoding storage of 64 images in $BaTiO_3$," Opt. Lett. **19**, 1894-1896 (1994).

[1-33] J. F. Heanue, M. C. Bashaw, and L. Hesselink, "Recall of linear combinations of stored data pages based on phase-code multiplexing in volume holography," Opt. Lett. **19**, 1079-1081 (1994).

[1-34] J. F. Heanue, M. C. Bashaw, and L. Hesselink, "Encrypted holographic data storage based on orthogonal-phase-code multiplexing," Appl. Opt., **34**, 6012-6015 (1995).

[1-35] D. Psaltis, M. Levene, A. Pu, G. Barbastathis, and K. Curtis, "Holographic storage using shift multiplexing," Opt. Lett. **20**, 782-784 (1995).

[1-36] D. Psaltis, D. Brady, and K. Wagner, "Adaptive optical networks using photorefractive crystals," Appl. Opt. **27**, 1752-1759 (1988).

[1-37] D. Psaltis, D. Brady, X. G. Gu, and S. Lin, "Holography in artificial neural networks," Nature **343**, 6526 (1990).

[1-38] K. Curtis, A. Pu, D. Psaltis, "Method for holographic storage using peristrophic multiplexing," Opt. Lett. **19**, 993-994 (1994).

[1-39] G. Burr, *Volume holographic storage using the 90-degree geometry*, Ph.D. thesis, California Institute of Technology, 1997.

[1-40] J. A. Jenny, "Holographic recording with photopolymers," J. Opt. Soc. Am. **60**, 1155-1161 (1970).

[1-41] W. S. Colburn and K. A. Haines, "Volume holographic formation in photopolymer materials," Appl. Opt. **10**, 1636-1641 (1971).

[1-42] K. Curtis and D. Psaltis, "Characterization of the DuPont photoplymer for three-dimensional holographic storage," Appl. Opt. **33**, 5396-5399 (1994).

[1-43] G. E. Peterson, A. M. Glass, and T. J. Negran, "Control of the susceptibility of lithium niobate to laser-induced refractive index changes," Appl. Phys. Lett. **19**, 130-132 (1971).

[1-44] W. Philipis, J. J. Amodei, and D. L. Staebler, "Optical and holographic storage properties of transition metal doped lithium niobate," RCA Review **33**, 94-109 (1972).

[1-45] D. Rytz, B. A. Weschler, M. H. Garret, C. C. Nelson, and R. N. Schwartz, "Photorefractive properties of $BaTiO_3$:Co," J. Opt. Soc. Am **B 7**, 2245-2254 (1990).

[1-46] M. Zgonik, K. Nakagawa, and P. Günter, "Electro-optic and dielectric properties of photorefractive $BaTiO_3$ and $KNbO_3$," J. Opt. Soc. Am **B 12**, 1416-1421 (1995).

[1-47] K. Sayano, G. A. Rakuljic, A. Agranat, A Yariv, and R. R. Neurgaonkar, "Photorefractive dark conductivity in Cr-doped strontium barium niobate," Opt. Lett. **14**, 459-461 (1989).

[1-48] J. E. Ford, Y. Fainman, S. H. Lee, Y. Taketomi, D. Bize, and R. R. Neurgaonkar, "Multiplex holography in strotium barium niobate with applied field," J. Opt. Soc. Am **A 9**, 1183-1192 (1992).

[1-49] N. V. Kukhtarev, V. B. Markov, S. G. Odoulo, M. S. Soskin, and V. L. Vinetskii, "Holographic storage in electrooptic crystals. I. Steady state," Ferroelctrics **22**, 949-960 (1979).

[1-50] P. Yeh, *Introduction to Photorefractive Nonlinear Optics,* Wiley, New York, 1993.

[1-51] F. Mok, G. Burr, and D. Psaltis, "System metric for holographic memory systems," Opt. Lett. **21**, 896-898 (1996).

2 Comparison of the 90-degree and transmission geometry

2.1 Introduction

Holographic memories have been of intense interest[2-1]-[2-10] and have advantages compared with conventional memories in that they offer a data storage density of up to a few hundred gigabits per cubic centimeter through multiplexing and a data transfer rate of the order of gigabits per second with page access.[2-5] Recently, a lot of research has been conducted on $LiNbO_3$-based holographic storage systems, and several multiplexing methods have been proposed and demonstrated.[2-2][2-6][2-7][2-10]-[2-14] By multiplexing, tens of thousands holograms with information of gigabits can be stored in the same volume of recording medium to achieve large-scale holographic storage system. Many of the large-scale holographic recording demonstrations based on photorefractive crystals were performed using the 90-degree geometry, in which the two recording beams interfere inside the crystal by an angle of around 90 degrees.[2-3][2-7][2-10][2-14] The grating vector (or the K-vector) of hologram recorded inside the crystal is defined as the resultant vector of the wave vectors of two recording beams. In the 90-degree geometry the K-vector is almost fixed, while the K-vector in transmission geometry can be varied by changing the outside angle between the two recording beams. Figure 2-1 shows the schematic setups for the 90-degree and transmission geometries. Previous results suggest that the 90-degree geometry has high angular selectivity and relative insensitivity to holographic scattering

and fanning.[2-14] However, the 90-geometry has small dynamic range and recording speed. For example, typical values of the dynamic range measure (M /#) and sensitivity (S)

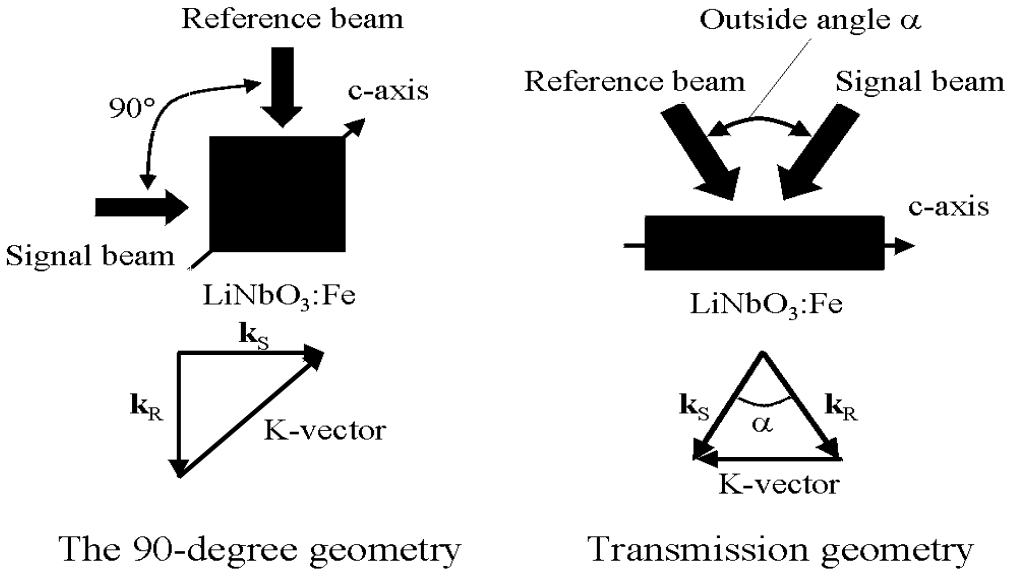

Fig. 2-1. The 90-degree geometry vs. transmission geometry. The K-vector in the 90-degree geometry is almost fixed, while the K-vector in transmission geometry can be varied by changing the outside angle between the two receding beams and is smaller than that of the 90-degree geometry.

of the 90-degree geometry with lightly iron-doped lithium niobate are 2.0 cm^{-1} and 0.02 cm/J, respectively.[2-14] For practical applications, larger values of M /# and *S* are required (M /# ~ 10 cm^{-1} and *S* ~ 1 cm/J).

One approach to boosting the M /# and sensitivity for the $LiNbO_3$-based holographic storage system is to increase the doping level. However, there is a limit on the practical doping level that we can use in $LiNbO_3$ crystals, above which no more dynamic range can be obtained. For example, for $LiNbO_3$:Fe crystals, the highest practical doping level is about 0.06 wt% Fe_2O_3 and is limited by dark decay.[2-15]-[2-17] It also has been found

that by using Mn instead of Fe as dopant, the practical highest doping level can be increased considerably to obtain larger M/# and sensitivity.[2-18] This is because in highly-doped $LiNbO_3$ crystals the limiting factor for doping level, which is the dark decay, is dominated by electron tunneling. Since Mn is a deeper center than Fe, the probability of electron tunneling in $LiNbO_3$:Mn is less than that in $LiNbO_3$:Fe. Therefore we can use higher doping levels in $LiNbO_3$:Mn crystals to obtain larger M/# and higher sensitivity. Another way to boost the M/# and sensitivity for the $LiNbO_3$-based holographic storage system is to use transmission geometry instead of the 90-degree geometry. In this chapter, we compare the system performances of the 90-degree and transmission holographic recording geometries using iron-doped lithium niobate. The comparison measures are dynamic range (M/#), sensitivity (S), scattering noise, inter-pixel noise, and storage capacity. We find that transmission geometry is better because the attainable dynamic range (M/#) is much higher. The only drawback of transmission geometry is the buildup of fanning, particularly during readout. Material solutions that reduce fanning, such as doubly-doped photorefractive crystals, make transmission geometry the clear winner.

2.2 M/# and sensitivity

One of the most important system metrics for holographic storage systems is the dynamic range (M/#). When M holograms are multiplexed using an appropriate recording schedule,[2-19] equalized diffraction efficiencies for these M holograms can be achieved. The equalized diffraction efficiency of each hologram, η, is given by[2-20]

$$\eta = \left(\frac{M/\#}{M}\right)^2, \tag{2-1}$$

where M/# is defined as the dynamic range measure of the holographic storage system. Equation (2-1) suggests that in multiplexing holograms with a prescribed diffraction efficiency η, increase of the M/# results in increase of the number of holograms that can be multiplexed (M), thus the capacity of the holographic storage system. On the other hand, with fixed number of holograms multiplexed, larger M/# results in higher diffraction efficiency for each hologram, therefore, higher signal to noise ratio (SNR) and data transfer rate. Another important system metric for a holographic storage system is sensitivity, which determines the recording speed. The larger the sensitivity, the faster we can record the hologram with a fixed recording intensity. For a holographic storage system, it is always desirable to have the largest possible M/# and sensitivity.

Dynamic range (M/#) and sensitivity (S) can be measured by single-hologram recording and erasure experiments.[2-20] From the single-hologram recording and erasure curves, we can calculate M/# and S using

$$M/\# = \left(\frac{d}{dt}\sqrt{\eta}\Big|_{t=0}\right) \times \tau_e, \tag{2-2}$$

$$S = \left(\frac{d}{dt}\sqrt{\eta}\Big|_{t=0}\right) / (IL), \tag{2-3}$$

where τ_e, I, and L are the erasure time constant, total recording intensity, and the crystal thickness, respectively. In our experiments of measuring M/# and sensitivity, an argon-ion laser beam with the wavelength of 488 nm was used to record and erase holograms. The crystal was placed on a rotation stage. The laser beam was split into two equal-intensity beams with the intensity of each beam being about 10 mW/cm^2. The grating vector is always aligned along the c-axis. During recording, one beam was blocked from

time to time to measure the holographic diffraction efficiency. We used Bragg-mismatched erasure, i.e., during erasure the sample was rotated far away from the Bragg-matched position (by at least 50 times of the selectivity) and illuminated by the same two beams that were used to record holograms. This guaranteed that the spurious gratings recorded during erasure would have little effect on the measurement of M/# and sensitivity. Moreover, in order to avoid building strong spurious holograms and fanning, the sample was rotated 0.02 degree every 10 seconds during erasure. At the end of each period of erasure, the diffraction efficiency was measured by scanning over an adequate range of angle (which covered the Bragg-matched position) and finding the maximum diffraction efficiency with only the reference beam on. Table 2-1 and Table 2-2 summarize measured M/# and sensitivity for three $LiNbO_3$:Fe crystals of the 90-degree geometry and three $LiNbO_3$:Fe crystals of transmission geometry available in our labs.

Table 2-1. Measured M/# and sensitivity for the 90-degree geometry crystals.

Sample	Doping level (mol%)	Thickness (mm)	M/# (per cm)	S (cm/J)
S1	0.01	20	2.30	0.02
S2	0.015	20	2.25	0.02
S3	0.015	20	3.34	0.03

Table 2-2. Measured M/# and sensitivity for transmission geometry crystals (extraordinary polarization, outside angle: 20^o).

sample	Doping level (mol%)	Thickness (mm)	M/# (per cm)	S (cm/J)
S4	0.01	5.0	14.46	0.22
S5	0.015	4.5	24.01	0.14
S6	0.03	5.0	35.72	0.34

From Table 2-1 and Table 2-2, we can see that both M/# and sensitivity in transmission geometry are considerably larger than those in the 90-degree geometry. The measured M/#'s of transmission geometry crystals are about 10 times as large as those of the 90-degree geometry crystals. The measured sensitivities of transmission geometry crystals are also about 10 times as large as those of the 90-degree geometry crystals. Three factors contribute to the larger M/# and sensitivity in transmission geometry: smaller K-vector, larger effective electrooptic coefficient r_{eff}, and higher average modulation depth. Accordingly, we can represent M/# as the product of three terms corresponding to these three factors:[2-14]

$$M/\# = M_1(K)M_2(r_{eff})M_3(m, \alpha) \equiv (E_{sc} \times \tau_e / \tau_r)\left(\frac{1}{2} \times k_0 n^3 r_{eff}\right)M_3(m, \alpha). \qquad (2\text{-}4)$$

The first term

$$M_1(K) = E_{sc} \times \tau_e / \tau_r \qquad (2\text{-}5)$$

is a function of the K-vector and can be obtained by solving linearized Kukhtarev equations,[2-21][2-22] where E_{sc}, τ_r, and τ_e are the saturation space-charge field for unity modulation depth (m=1), the recording time constant, and the erasure time constant, respectively. The second term

$$M_2(r_{eff}) = \frac{1}{2} \times k_0 n^3 r_{eff} \qquad (2\text{-}6)$$

is related to the polarization and wavelength of light beams, where k_0 is the amplitude of K-vector in vacuum, n is the refractive index of the crystal. The third term $M_3(m, \alpha)$ is somehow complicated. It is a function of geometrical parameters, outside modulation depth m and absorption coefficient α. We can consider $M_3(m, \alpha)$ as the effective modulation

depth.[2-14] The theoretical derivation of the M/# in transmission geometry using extraordinary polarization is presented in Appendix of this chapter.

Using the first-order approximation, we can analytically solve the Kukhtarev equations, which govern the photorefractive effect in iron-doped lithium niobate crystals, to obtain E_{sc} and $M_1(K)$ as in the following:

$$E_{sc} = E_q \sqrt{\frac{E_{ph}^2 + E_d^2}{[(N_A/N_D) \times E_{ph}]^2 + (E_d + E_q)^2}}, \tag{2-7}$$

$$M_1(K) = E_q \times \frac{\sqrt{E_{ph}^2 + E_d^2}}{E_d + E_q}, \tag{2-8}$$

where N_D and N_A are the total concentration of the deep (i.e., Fe) traps and the concentration of the ionized deep traps (i.e., Fe^{3+}), respectively.[2-21][2-22] In these equations, the saturation field E_q, the photovoltaic field E_{ph}, and the diffusion field E_d are given by

$$E_q = \frac{qN_A(N_D - N_A)}{\varepsilon K N_D}, \tag{2-9}$$

$$E_{ph} = \frac{p\gamma_A N_A}{q\mu s}, \tag{2-10}$$

$$E_d = \left(\frac{k_B T}{q}\right) \times K, \tag{2-11}$$

with γ_A, s and p being the recombination rate of electrons in the conduction band, the absorption cross section for the excitation of electrons from the deep traps to the conduction band and the photovoltaic constant of the deep traps (both at the recording wavelength), respectively. Electron charge, Boltzman constant, and absolute temperature are represented by q, k_B, and T, respectively. The magnitude of the K-vector is denoted by K.

Figure 2-2 shows E_d, E_q, E_{ph} and E_{sc} as functions of K for a $LiNbO_3$:Fe crystal with

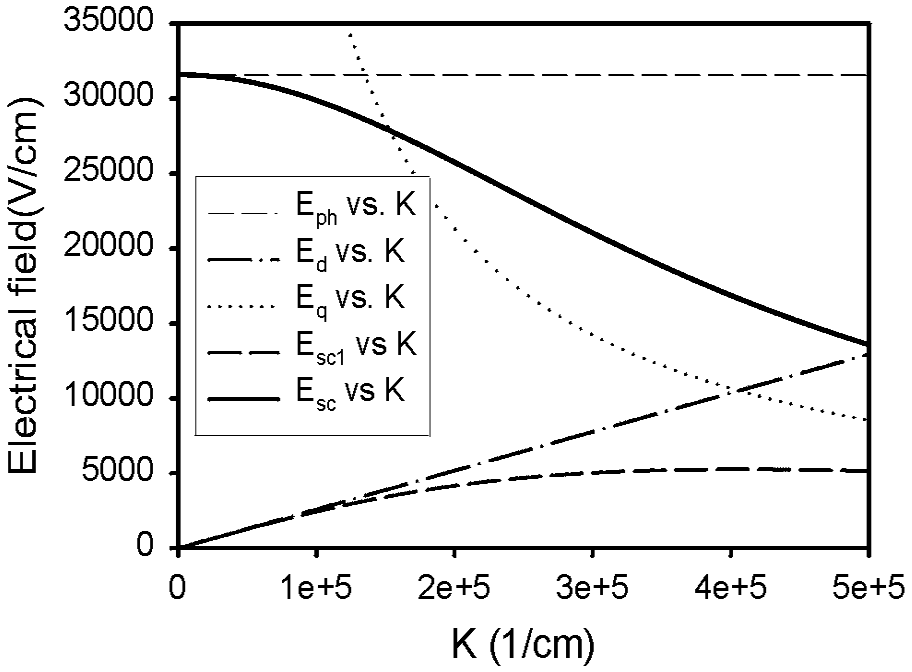

Fig. 2-2. E_d, E_q, E_{ph} and E_{sc} as functions of K-vector for a $LiNbO_3$:Fe crystal. The amplitude of K-vector in the 90-degree geometry is about 427900cm^{-1}, while the amplitude of K-vector of transmission geometry can be varied between 0 to 257508 cm^{-1}.

the doping level of 0.015 mol% and the oxidation state of $C_{Fe^{2+}}/C_{Fe^{3+}} = 0.03$. The magnitude of the K-vector (i.e., K) in the 90-degree geometry at the wavelength of 488 nm is about 427900 cm^{-1}, while K for transmission geometry can be varied between 0 and 257508 cm^{-1} at the same wavelength. For transmission geometry in $LiNbO_3$ (in which K is small) the photovoltaic field E_{ph} dominates the photorefractive effect, while for the 90-degree geometry (where K is relatively large) the space charge field E_{sc} is limited by the saturation field E_q. In the crystals we used, the photovoltaic field E_{ph} (i.e., the dominant

field in transmission geometry) is larger than the saturation field of the 90-degree geometry. Therefore, $M_1(K)$ is larger in transmission geometry than that in the 90-degree geometry. Figure 2-3 shows the theoretical and experimental normalized $M_1(K)$ (with the normalized

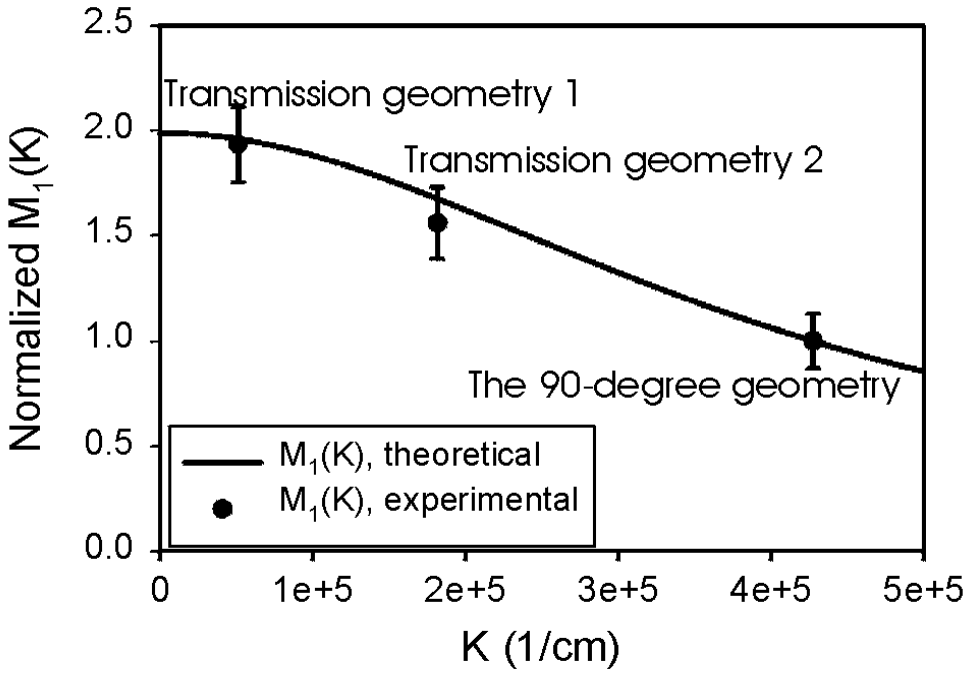

Fig. 2-3. Theoretical (solid curve) and experimental (circles) normalized $M_1(K)$ for transmission geometry as functions of K (with the normalized $M_1(K)$ of the 90-degree geometry equal to 1). For the transmission geometry 1, the smaller K contributes to an increase in the M/# by a factor of 2 compared to that of the 90-degree geometry.

$M_1(K)$ of the 90-degree geometry equal to 1) as functions of K. From Figure 2-3 we can see that for transmission geometry 1, in which the outside angle between two recording beams is 20^o, the smaller K contributes to an increase in the M/# by a factor of 2 compared to that of the 90-degree geometry.

Due to the large refractive index of the $LiNbO_3$ crystal (n = 2.3 for visible light), the angle between two recording beams inside the crystal in transmission geometry is small even when the outside angle is close to 180^o. This fact allows us to use both ordinary and extraordinary polarizations in transmission geometry, which is shown in Figure 2-4. The

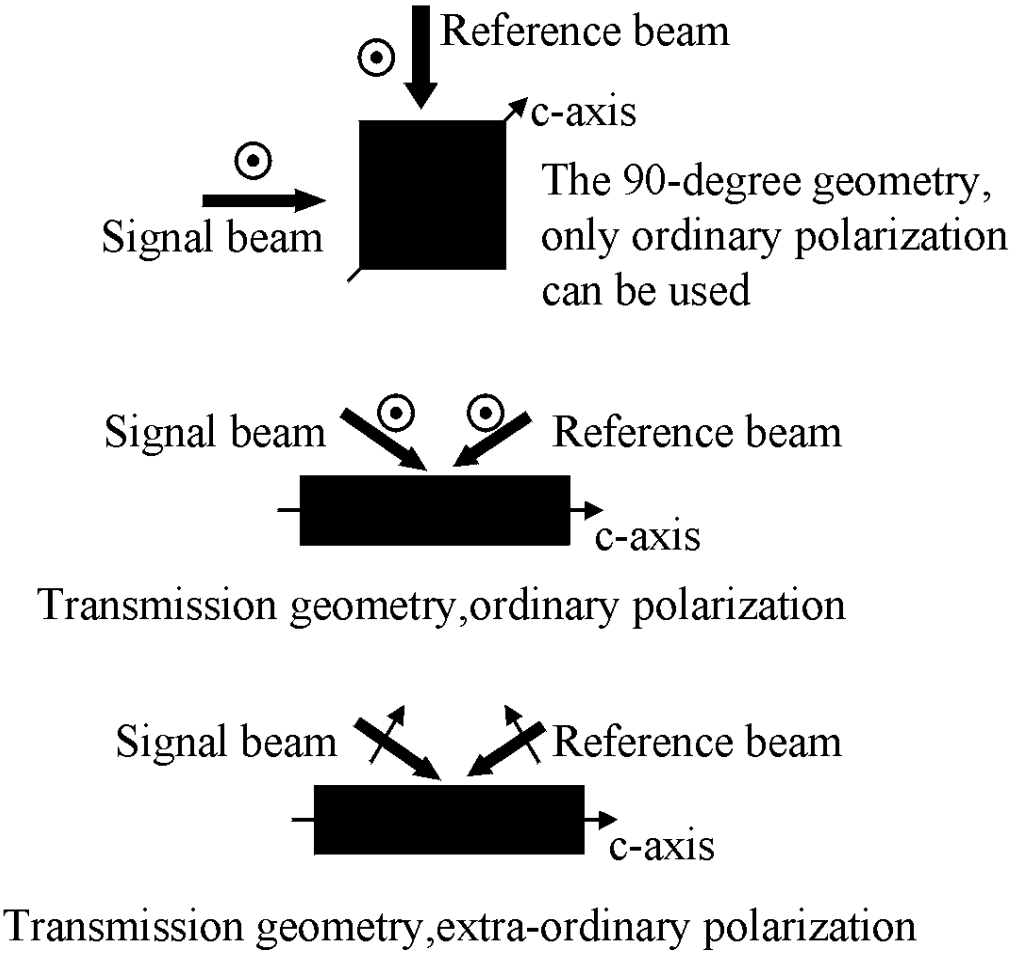

Fig. 2-4. The angle between signal and reference beams inside crystal in transmission geometry is small, which allows us to use both extraordinary and ordinary polarizations. The angle between signal and reference beams inside crystals in the 90-degree geometry is 90^o, where only ordinary polarization can be used.

electrooptic coefficient of $LiNbO_3$ for extraordinary polarization is about three times as large as that for ordinary polarization ($r_{33} = 3\,r_{13}$). In the 90-degree geometry the angle between two recording beams is around 90^o. Therefore we can only use ordinary polarization. Since the angle between two beams inside the crystal is small in transmission geometry, the effective electrooptic coefficient for transmission geometry with extraordinary polarization is about 3 times as large as that in the 90-degree geometry, which means that $M_2(r_{eff})$ for transmission geometry is also about 3 times as large as that of the 90-degree geometry. Therefore, by using extraordinary polarization in transmission geometry we can boost M/# by a factor of about 3.

Another factor that contributes to the larger M/# and sensitivity in transmission geometry is that the local modulation depth in transmission geometry is always close to 1, which is optimal for holographic recording. On the other hand, the local modulation depth in the 90-degree geometry is always less than 1 because of the optical absorption and geometrical asymmetry, except for a very small portion of the crystal. This is illustrated in Figure 2-5. In the crystals we used, the average modulation depth of transmission geometry, $M_3(m, \alpha)$, is about 2 times as large as that of the 90-degree geometry, which boosts the M/# of transmission geometry by another factor of 2.

From Equation (2-2) and Equation (2-3) we can see that the only difference between M/# (normalized to thickness L) and S is that M/# is proportional to erasure time constant τ_e, while S is inversely proportional to the total intensity of recording I. It is known that erasure time constant τ_e is inversely proportional to the total intensity, therefore we would expect the same dependence of S on the above three factors as that of M/#. The three factors mentioned previously, i.e., smaller K-vector, larger effective electrooptic coefficient

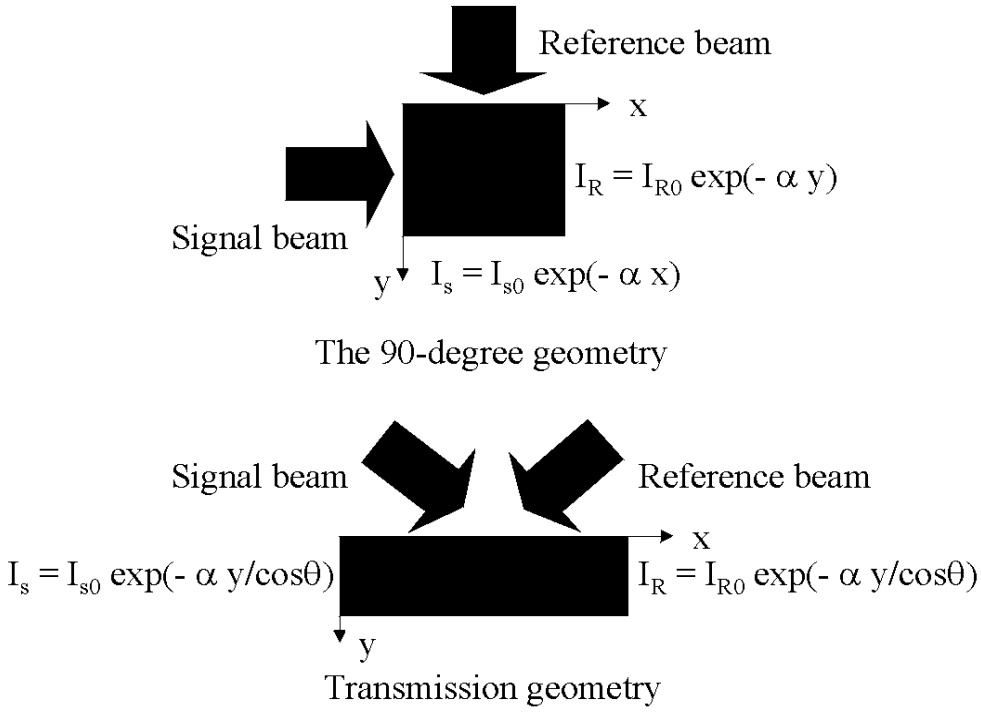

Fig. 2-5. In symmetric transmission geometry, the local modulation depth is always 1, which is optimal for holographic recording. On the other hand, the local modulation depth in the 90-degree geometry is always less than 1 because of the optical absorption and geometrical asymmetry, except for a very small portion of the crystal.

γ_{eff}, and higher average modulation depth, contribute to the boost for sensitivity in the same way for M/# in transmission geometry. This explains the results shown in Table 2-1 and Table 2-2.

2.3 Scattering noise

Noise in holographic storage systems is very important since it determines the overall system performance. In a noise-limited system, lowering the noise level is equivalent to increasing the storage capacity and/or obtaining better SNR. One of the main noise sources

in holographic storage systems is scattering noise. This kind of noise is the result of the scattering of the reading beam by imperfections within the recording material (i.e., $LiNbO_3$). Scattering noise is a strong function of the angle between the scattering and the scattered beams. Figure 2-6 shows the experimental setup for measuring scattering of a typical $LiNbO_3$:Fe crystal, of which the thickness is 15 mm and the doping level is 0.015 mol% Fe_2O_3. The surfaces of the crystal have been polished to optical quality. One beam of plane

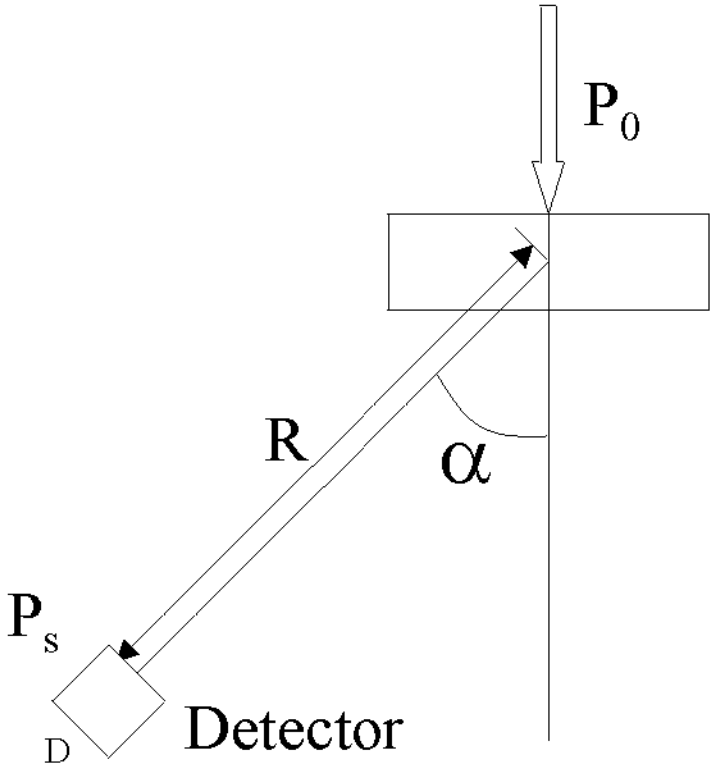

Fig. 2-6. Experimental setup for measuring scattering as a function of angle. One beam of plane wave with the wavelength of 488 nm and optical power of P_0 illuminates the center of the crystal at normal incidence. A detector with aperture diameter D is placed at a distance R from the center of the crystal to measure the scattering power P_s.

wave with the wavelength of 488 nm and optical power of P_0 illuminates the center of the

crystal at normal incidence. A detector with aperture diameter D is placed at a distance R from the center of the crystal to measure the scattering power P_s. The scattering efficiency per steradian η_s is calculated as

$$\eta_s = \left(\frac{P_s}{P_0}\right) \Big/ \frac{\pi(D/2)^2}{R^2} \tag{2-12}$$

In practice, it is the standard deviation of scattering noise that matters. In order to obtain the standard deviation of scattering noise, it would require that the probability distribution of scattering noise be known, which is sometimes very difficult. Here we use the average value of the scattering noise as a convenient indication of the standard deviation of scatting noise. Figure 2-7 shows the measured scattering efficiency per steradian and the exponential fit as a function of the angle. We can see from Figure 2-7 that the scattering efficiency decreases exponentially as the scattering angle α changes from 0 to 90^o. The scattering noise in transmission geometry is much larger than that in the 90-degree geometry, especially when the angle between the two recording beams is very small. However, what matters in holographic storage systems is signal-to-noise ratio, not the absolute noise level or scattering efficiency. Considering the boost of M/# in transmission geometry and the fact that the reconstructed signal level is proportional to $(M/\#)^2$, the signal to scattering noise ratio (SSNR) in transmission geometry could be better than that in the 90-degree geometry. Figure 2-8 shows the normalized signal level, the scattering noise level, and SSNR in transmission geometry as functions of the angle between the recording beams inside the crystal. The data in all three curves are normalized to the corresponding values in the 90-degree geometry. In other words, the normalized values of the signal level, the scattering noise level, and SSNR for the 90-degree geometry are all equal to 1. In this sim-

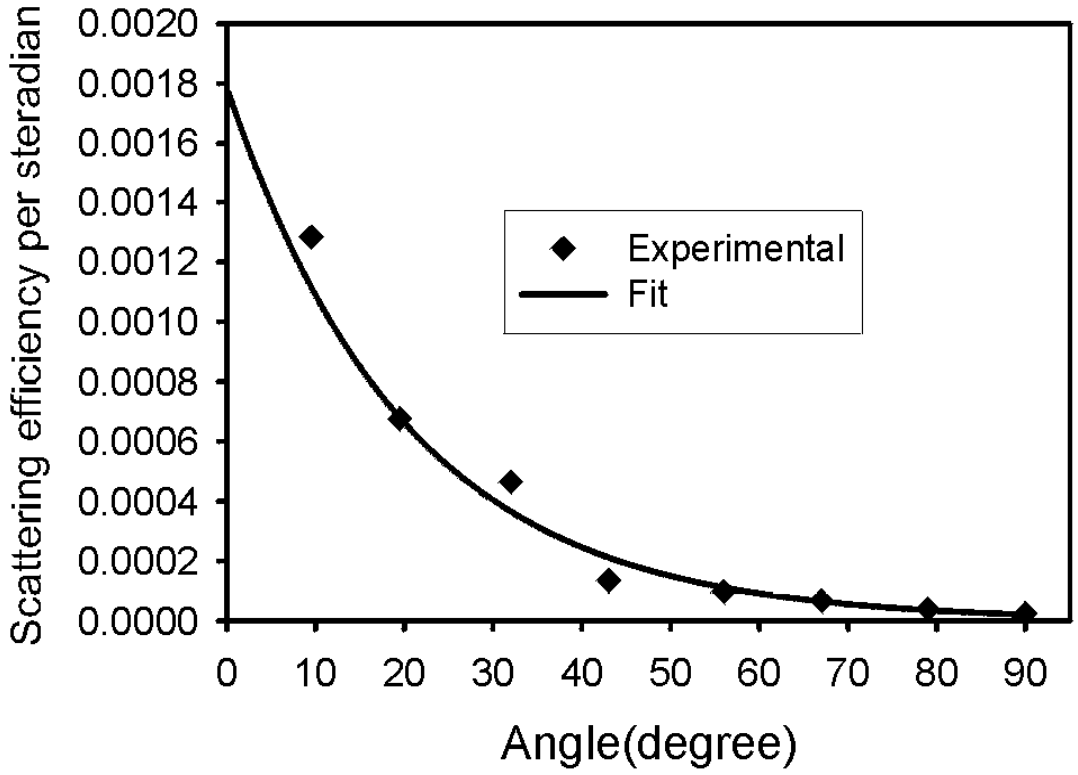

Fig. 2-7. Measured scattering efficiency per steradian as a function of angle. The solid line represents an exponential fit to the experimental results. The scattering noise in transmission geometry is larger than that in the 90-degree geometry, especially when the angle between the two recording beams is small.

ulation, we used the doping level of 0.06 wt% Fe_2O_3, the thickness of 2 cm for the $LiNbO_3$ crystal. The results shown in Figure 2-8 were calculated by first optimizing the M/# in the 90-degree geometry (through the appropriate choice of the optical absorption, or oxidation state). Then, the absorption of transmission geometry crystal was chosen to obtain the same sensitivity as that of the 90-degree geometry crystal. Using this absorption, the M/# and other parameters of the transmission geometry crystal were calculated and plotted in Figure 2-8. The signal level is proportional to $(M/\#)^2$. As we can see from Figure 2-8, the SSNR in transmission geometry is better than that in the 90-degree geometry even though the scat-

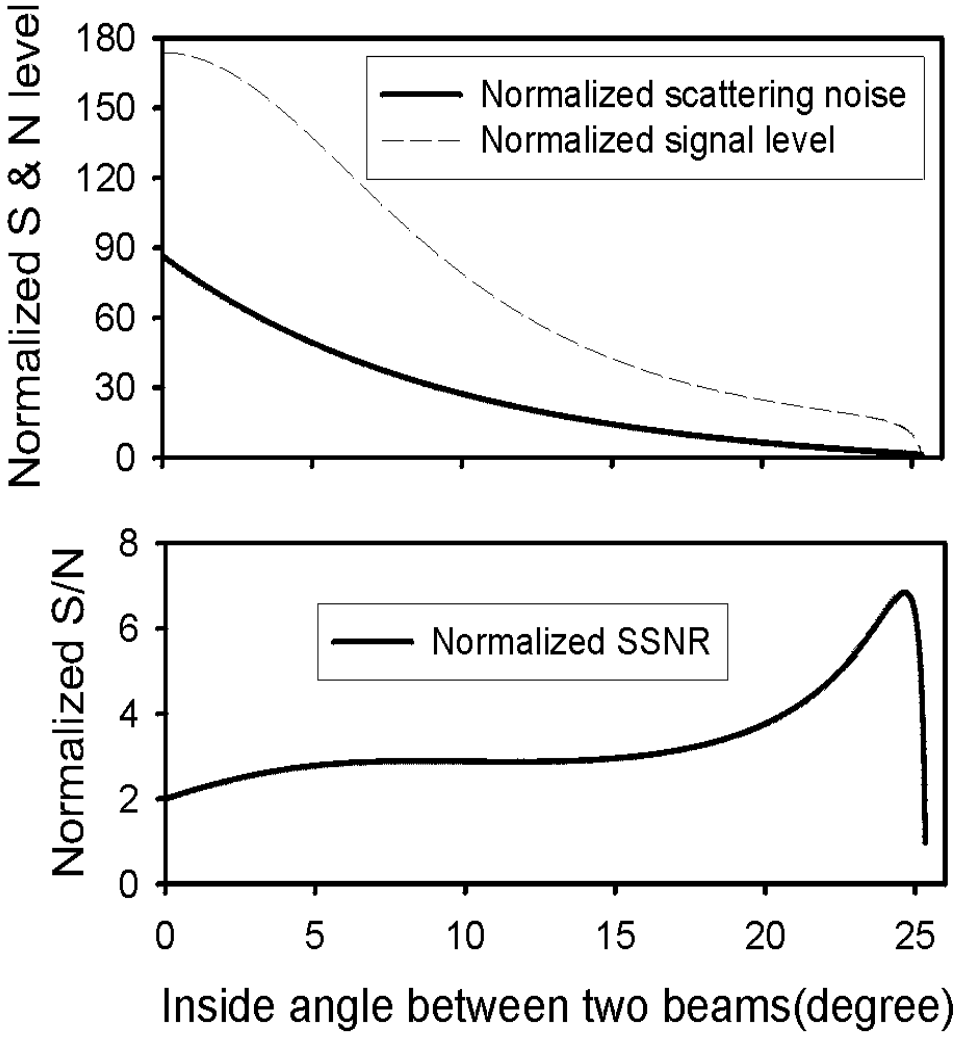

Fig. 2-8. Normalized signal level, scattering noise, and signal to scattering noise ratio (SSNR) in transmission geometry as functions of the angle between the two recording beams inside the crystal with all the corresponding values in the 90-degree geometry normalized to 1. The SSNR in transmission geometry is better than that in the 90-degree geometry even though the scattering noise level is higher in transmission geometry.

tering noise level is higher in transmission geometry. This is due to the larger M /# in transmission geometry.

Scattering can also occur because of fanning, which builds up during recording or readout. In general, fanning is a more serious problem than static scattering because it is unpredictable and if allowed to build up for a long time it will eventually lead to complete

deterioration of the performance. It is well known that the reason many of the large scale demonstrations of holographic memory were done in the 90-degree geometry is that fanning is less of a problem.[2-3][2-7][2-10] Therefore fanning is a very important consideration when we compare the two recording geometries. We performed an experiment to quantitatively assess the fanning behavior. The optical setup is shown in Figure 2-9 show-

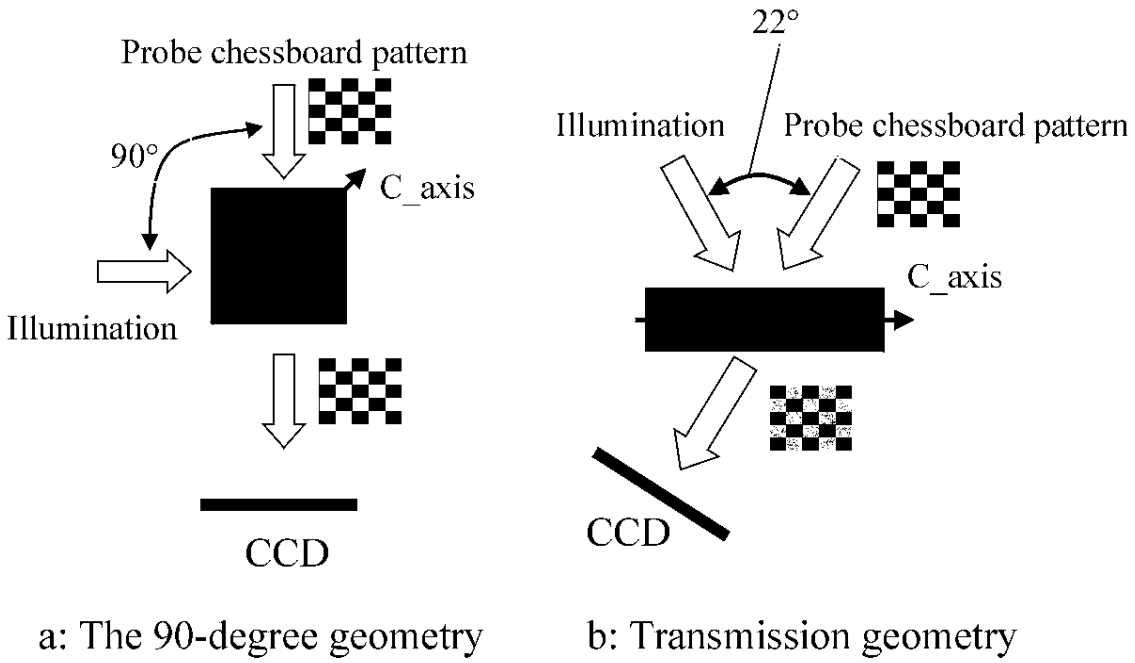

Fig. 2-9. Optical setup of holographic recording geometries for the 90-degree (a) and transmission (b) geometries for the measurement of fanning.

ing the standard holographic recording geometries for the 90-degree (Figure 2-9a) and transmission (Figure 2-9b) geometries. The crystals used were $LiNbO_3:Fe$ with a doping level 0.015 mol% in both cases. The oxidation state was approximately the same in both cases (measured absorption coefficient at $\lambda = 488\,\text{nm}$ was $0.5\,\text{cm}^{-1}$). In the first measurement only the reference beam (a plane wave, 488 nm, 7 mW/cm^2, ordinary polarization, 11^o

with respect to the crystal normal for the transmission case) was present. The light was monitored by a CCD at the plane where we would normally observe the reconstruction of the data page (see Figure 2-9). Initially only the static scattering was picked up by the CCD but as time goes on the fanning builds up and the CCD signal grows. In Figure 2-10 we plot

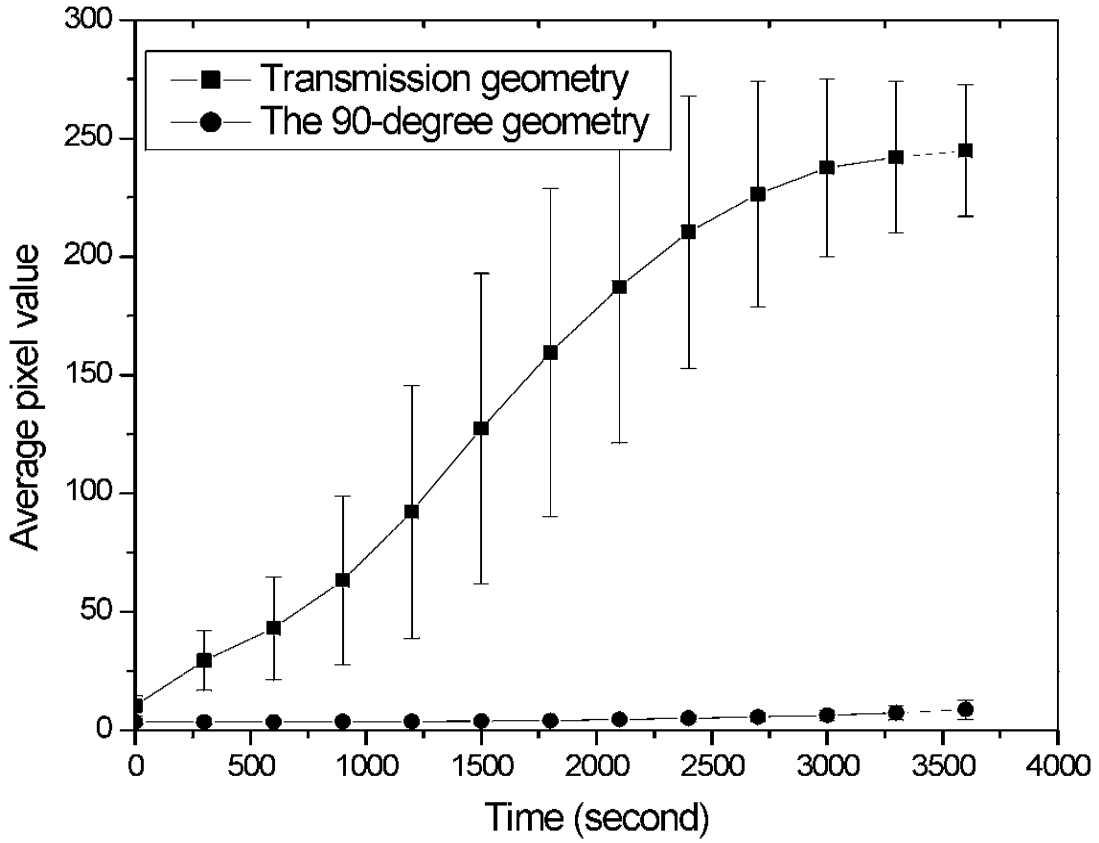

Fig. 2-10. Averaged pixel value and standard deviation of the CCD signal as a function of time. Within an hour the fanning of transmission geometry grows to a saturation level whereas the 90-degree geometry remains almost unaffected after one hour.

the averaged pixel value of the CCD signal as a function of time. Also shown in Figure 2-10 is the standard deviation of the calculated average signal. Clearly, within an hour the fanning of transmission geometry grows to a saturation level whereas the 90-degree geom-

etry remains almost unaffected after one hour. We also assess the impact of the fanning on system performance by introducing probe beam which is a chessboard pattern that modulates the signal beam. For this measurement we desire to measure the SNR between the probe and the fanning noise as it is read out by the reference beam. We avoid recording a hologram containing the chessboard by using orthogonal polarizations in the signal and reference beams and minimizing the simultaneous exposure time. The intensity of the probe beam was set to 10^{-4} mW/cm^2 simulating a hologram with diffraction efficiency equal to 10^{-5} illuminated by a beam with 10mW/cm^2. As shown in Figure 2-11, the SNR remains

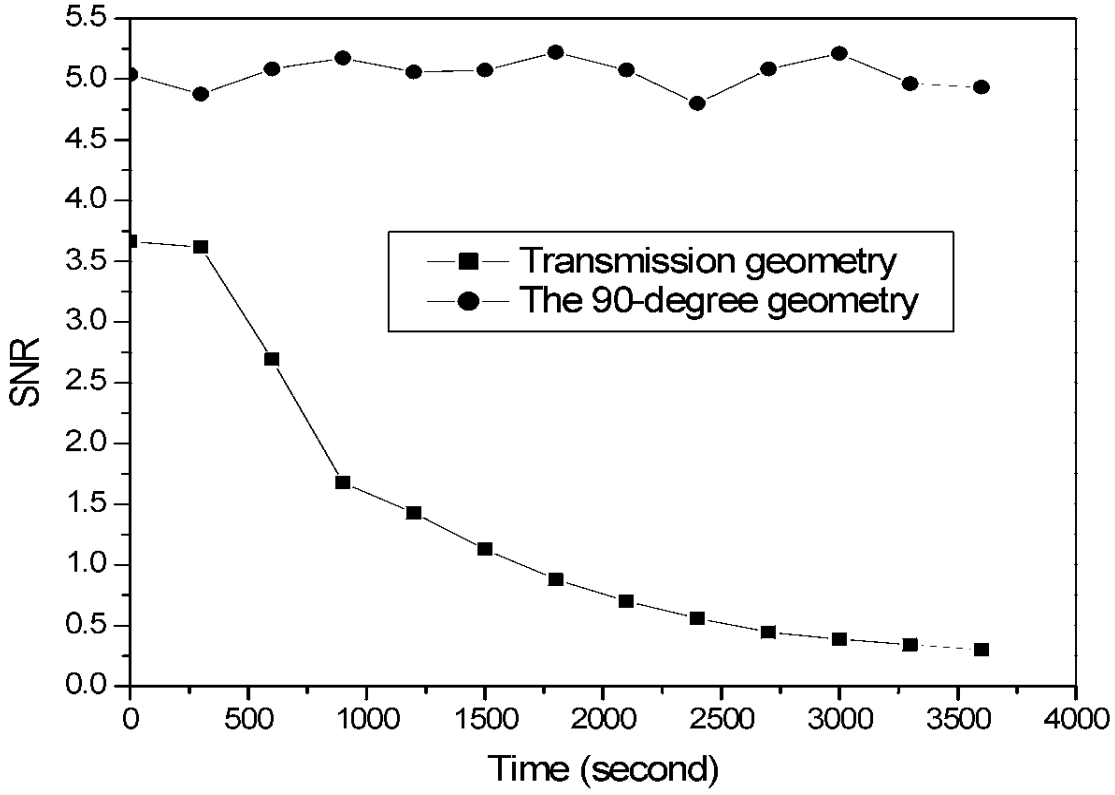

Fig. 2-11. Measured SNR degradation due to fanning. The SNR remains virtually unchanged for the 90-degree geometry whereas it deteriorates to virtually zero within an hour for transmission geometry.

virtually unchanged for the 90-degree geometry whereas it deteriorates to virtually zero within an hour for transmission geometry.

From these measurements we see that indeed fanning is the major drawback of transmission geometry. The reduced fanning of the 90-degree geometry in $LiNbO_3$: Fe can be attributed partially to the lower sensitivity of this geometry and the large angle between the two recording beams as we already discussed.

Fanning depends on the choice of material property as well as the geometry. For instance fanning is not observed in doubly-doped lithium niobate when it is recorded in the presence of a blue sensitizing beam and readout in the red.[2-23][2-24] This can be attributed to the erasure of the fanning signal by the blue beam during recording and the low sensitivity of the crystal in the red during readout. Fanning is also dramatically reduced in $LiNbO_3$: Mn crystals recorded in the blue.[2-18]

As discussed in the previous section, the sensitivity with extraordinary polarization is larger than that with ordinary polarization. It is known that the buildup of fanning is faster with larger sensitivity. With the same recording time, the buildup of fanning with extraordinary polarization is faster than that with ordinary polarization. Nevertheless, it will take less time with extraordinary polarization to achieve the same diffraction efficiency than that with ordinary polarization and the fanning will be comparable with both extraordinary and ordinary polarizations during recording. In this sense, the speeds of buildup of fanning with extraordinary and ordinary polarizations in transmission geometry are comparable.

2.4 Inter-pixel noise

Another main source of noise in holographic storage systems is inter-pixel noise. Inter-pixel grating is a very important yet largely ignored form of holographic noise. It is caused by rediffraction of the diffracted signal from the gratings formed between the multiple plane-wave (spatial-frequency) components of the signal beam. Inter-pixel grating noise can be considered as crosstalk noise between the pixels (bits) within a page of information, similar to a class of higher-order crosstalk noise in volume holographic interconnection.[2-25][2-26] In the setup of Fourier-plane recording where the holographic recording medium is placed at the Fourier-transform plane of the SLM, inter-pixel grating noise occurs directly between the pixels on the SLM. Individual pixels are converted into plane waves inside the storage medium. During holographic recording, these plane waves interfere with the reference beam to form the desired information hologram. In the meantime, they interfere with each other to create inter-pixel noise gratings. Upon readout, the same reference beam is used to reconstruct the plane waves, which are converted back to the corresponding pixels for data retrieval by imaging optics. In addition, these reconstructed plane waves give rise to secondary diffraction via the inter-pixel gratings, resulting in inter-pixel grating noise. This inter-pixel noise is the main source of noise for large-scale holographic memories.

Figure 2-12 shows the orientations of inter-pixel grating vectors and the c-axis in transmission geometry and in the 90-degree geometry. Due to the symmetry of the SLM pixels and the fact that the spatial frequencies of the pixels are relatively small, the inter-pixel grating vectors in both transmission geometry and the 90-degree geometry can be considered to be perpendicular to the propagating direction of the signal beam. In transmis-

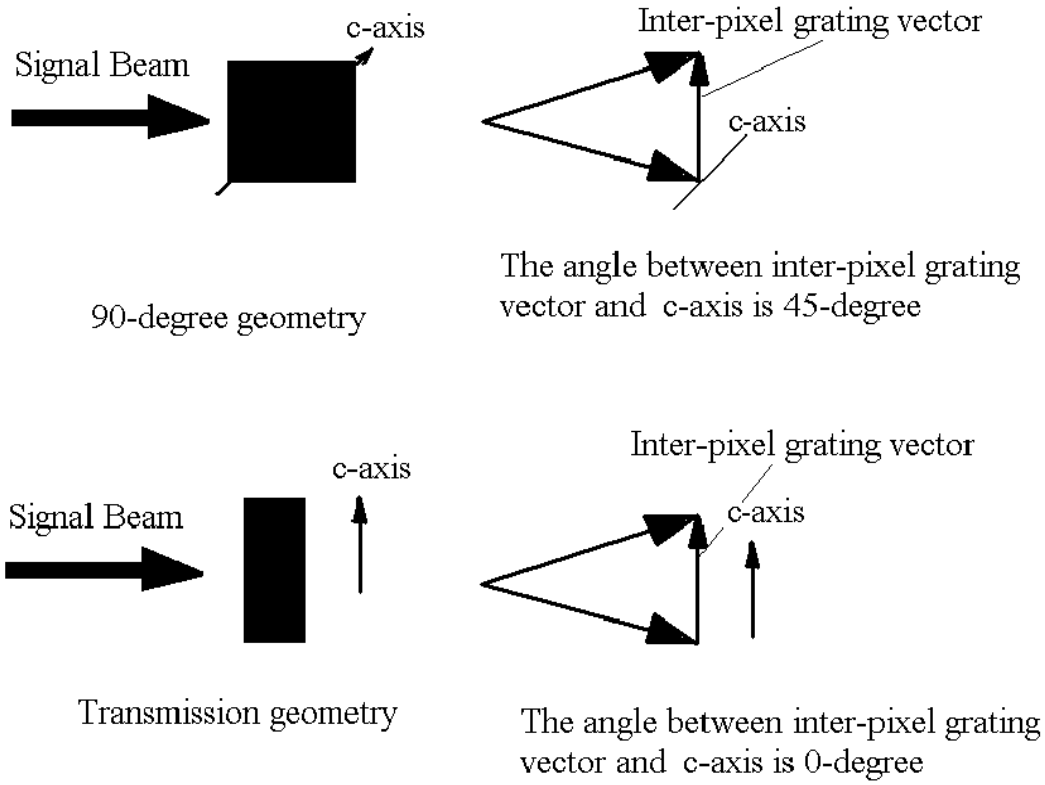

Fig. 2-12. Inter-pixel grating for the 90-degree geometry and transmission geometry. In transmission geometry, the inter-pixel grating vector is parallel to the c-axis of the crystal, while the angle between inter-pixel grating vector and the c-axis of the crystal of the 90-degree geometry is 45^{o}.

sion geometry, the inter-pixel grating vector is parallel to the c-axis of the crystal, while the angle between inter-pixel grating vector and the c-axis of the crystal in the 90-degree geometry is 45^{o}. The grating strength is proportional to the cosine of the angle between the grating vector and the c-axis of the crystal, and the diffraction efficiency is proportional to the square of the grating strength. Therefore, we would expect the inter-pixel grating noise in transmission geometry to be larger than that in the 90-degree geometry by a factor of 2.

One approach to monitoring the evolution of the inter-pixel noise gratings is to measure the degradation of SNR of a testing pattern, e.g., chessboard, through the crystal during

the recording. Figure 2-13 shows the experimental setup for measuring the evolution of inter-pixel noise gratings inside the crystal. The SLM, which is illuminated by a plane wave, is imaged to the CCD plane by a 4-f system consisting of two lenses. The crystal is

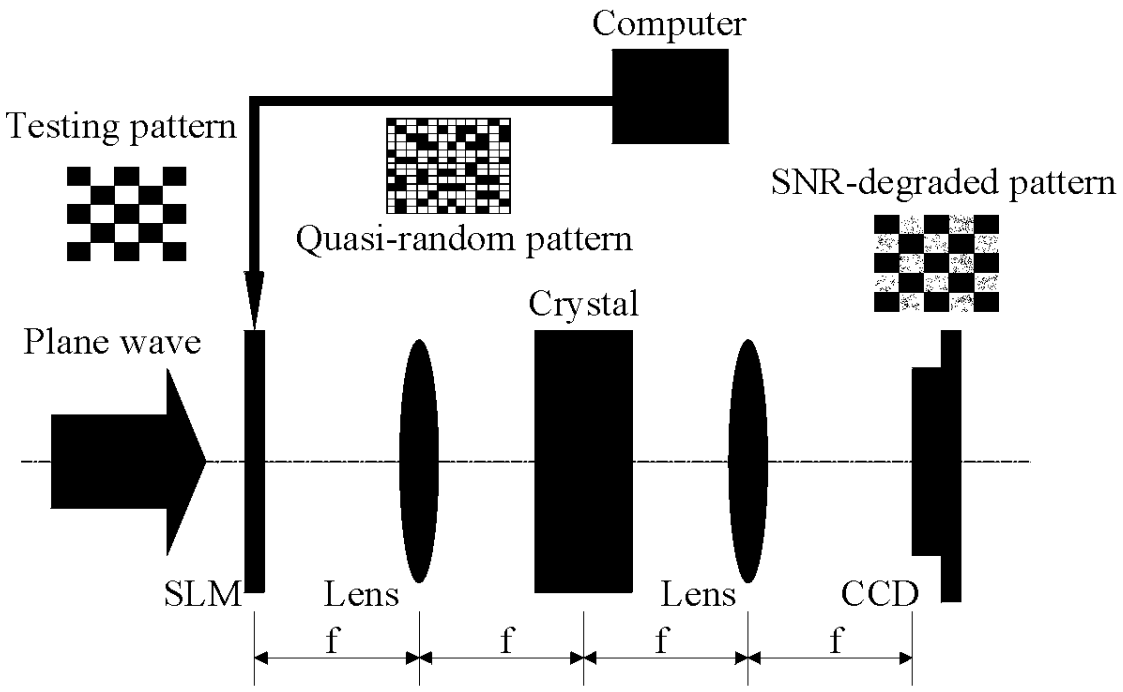

Fig. 2-13. Experimental setup for monitoring the evolution of inter-pixel noise grating. The SLM, which is illuminated by a plane wave, is imaged to the CCD plane by a 4-f system consisting of two lenses. The crystal is placed at the Fourier-transform plane of the SLM.

placed at the Fourier-transform plane of the SLM. Each pixel of SLM generates a plane wave with different spatial frequency through the crystal. These plane waves interfere with each other to form the inter-pixel noise grating. Figure 2-14 shows the measured SNR degradations due to inter-pixel noise as a function of time for one of the 90-degree geometry and one of the transmission geometry $LiNbO_3$:Fe crystals. The doping levels of both the

90-degree and the transmission geometry crystals are the same: 0.015 mol% Fe_2O_3. Also, the absorption coefficients of these two crystals at 488 nm are almost the same, 0.5 cm^{-1}, which means that both crystals have approximately the same oxidation states. The interaction length of the 90-degree geometry crystal is 20 mm while that of transmission geometry crystal is 4.5 mm. The intensity of the plane wave that illuminates the SLM for both crystals is the same. To obtain the results shown in Figure 2-14, quasi-random patterns were

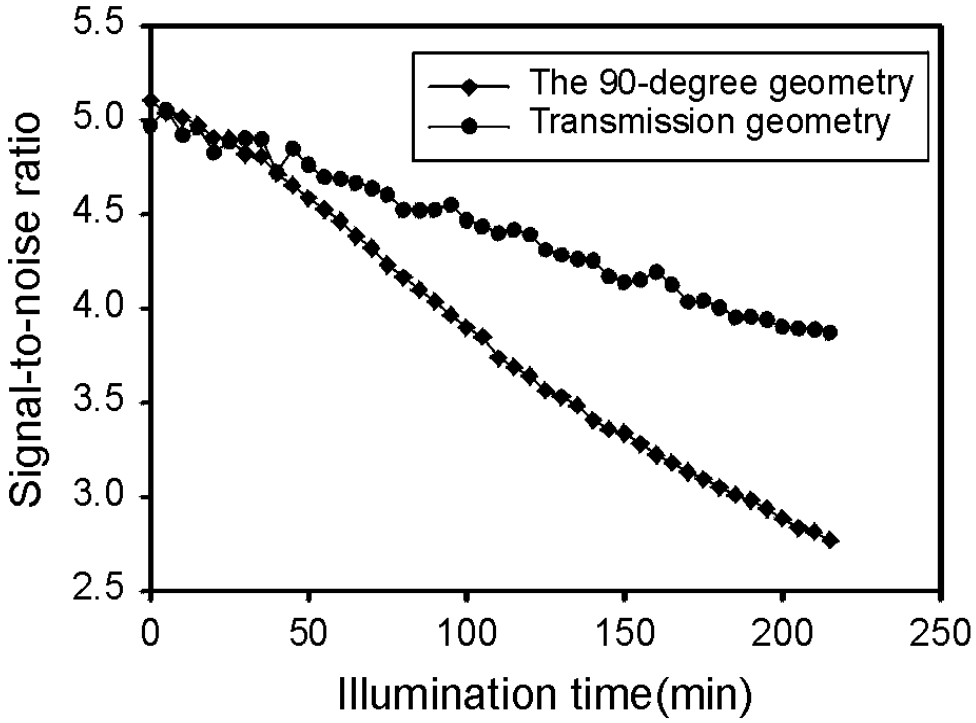

Fig. 2-14. Measured SNR degradations due to inter-pixel noise as functions of time for one of the 90-degree geometry and one of the transmission geometry $LiNbO_3$:Fe crystals. The interaction length of the 90-degree geometry crystal is 20 mm while that of the transmission geometry crystal is 4.5 mm.

imprinted to the SLM by a computer. From time to time, a big chessboard pattern was used to monitor the degradation of the SNR of the image behind the crystal. Note that in this experiment, we illuminate the crystal with only the signal beam. We changed the quasi-random pattern every 10 seconds to simulate the actual recording process and to minimize the build-up of holographic scattering noise. Therefore, we expect that any degradation in the SNR (shown in Figure 2-14) of a single image going through the crystal is due to the inter-pixel noise. The SNR is calculated as:

$$\mathrm{SNR} = \frac{\mu_1 - \mu_0}{\sqrt{\sigma_1^2 + \sigma_0^2}}, \tag{2-13}$$

where μ_1, σ_1, μ_0, and σ_0, are the average pixel value of ON pixels, the standard derivation of pixel value of ON pixels, the average pixel value of OFF pixels, and the standard derivation of pixel value of OFF pixels, respectively. From Figure 2-14 we can see that the speed of degradation of SNR in the 90-degree geometry crystal is about 2 times as large as that in the transmission geometry crystal. The inter-pixel noise intensity is proportional to $L^2[\exp(-\alpha L)]^2$ with α and L being the intensity absorption coefficient and the thickness of the crystal, respectively. The oxidation state of the 90-degree geometry crystal was optimized to obtain the best M/#. The optimum absorption coefficient for the 90-degree geometry crystal with thickness L = 2 cm is $\alpha = 1/L = 0.5\ \mathrm{cm}^{-1}$. The absorption coefficient of the transmission geometry crystal was very close to that of the 90-degree geometry crystal (due to similar doping concentration and similar annealing treatment). Therefore, we expect the ratio of the interpixel noise levels (N_{IP}) in the two cases to be

$$\frac{N_{IP}\big|_{90-\mathrm{degree}}}{N_{IP}\big|_{\mathrm{Transmission}}} = [\cos(45°)]^2 \frac{(2)^2 \exp(-0.5 \times 2 \times 2)}{(0.45)^2 \exp(-0.5 \times 0.45 \times 2)} = 2.1, \tag{2-14}$$

which is in good agreement with the results shown in Figure 2-14. Therefore, the apparent worse inter-pixel noise in the 90-degree geometry is due to the larger thickness of the crystal. If we use the same thickness for the crystals used in the two geometries, we will get

$$\frac{N_{IP}|_{90-degree}}{N_{IP}|_{Transmission}} = [\cos(45°)]^2 = \frac{1}{2} \tag{2-15}$$

Our results suggest that under the same conditions (same doping level, same thickness, etc.), the inter-pixel noise level in transmission geometry is twice that in the 90-degree geometry. The comparison of the measure of signal to inter-pixel noise ratio, which is more important for holographic storage systems, must be performed with precautions. If we record the same number of holograms in both geometries, the diffracted signal level of each hologram is much larger in transmission geometry due to the larger M/#. This gives transmission geometry a better inter-pixel signal to noise performance. However, if we record as many holograms as possible in both geometries to obtain the highest capacity with the minimum acceptable diffraction efficiency, the signal to inter-pixel noise performance of the 90-degree becomes better than that of transmission geometry. This is because the signal level in both cases are the same while the noise level in the 90-degree geometry is smaller. The longer recording time of transmission geometry (due to recording of more holograms) will increase the inter-pixel noise level further. For a case between the two extremes discussed, either geometry can have better signal to inter-pixel noise performance depending on the number of holograms that are recorded. If we are not very close to the two extremes, we expect the inter-pixel noise performance in the 90-degree geometry and in transmission geometry to be comparable.

2.5 Storage capacity

Storage capacity is a key performance measure in holographic storage systems. One of the advantages of transmission geometry is that we can use extraordinary polarization for recording and read-out beam. By switching to extraordinary polarization from ordinary polarization, we increase the M/# (and therefore, the number of multiplexed holograms) by a factor of about 3. The angular selectivities in transmission geometry with both polarizations are almost equal, which means that using extraordinary polarization will not sacrifice the capacity in transmission geometry. This is shown in Figure 2-15, which depicts the experimentally measured and theoretically calculated angular selectivity curves for one transmission geometry $LiNbO_3$:Fe crystal with extraordinary and ordinary polarizations.

The angular selectivity of the 90-degree geometry is

$$\Delta\theta = \frac{\lambda}{L}, \tag{2-16}$$

while the angular selectivity of transmission geometry is

$$\Delta\theta = \frac{\lambda\cos\theta_s}{L\sin(\theta_s + \theta_r)}, \tag{2-17}$$

where λ is the reading wavelength outside the crystal; L is the interaction length; and θ_s and θ_r are the incident angles (inside the crystal) of the signal and the reference beam, respectively. With the same interaction length of crystal, the angular selectivity of the 90-degree geometry is better than that of transmission geometry. This may suggest that more holograms can be angularly multiplexed using the 90-degree geometry, and that the 90-degree geometry has a larger capacity than transmission geometry. However, this conclusion is based on the assumption that the holographic system has enough dynamic range to record

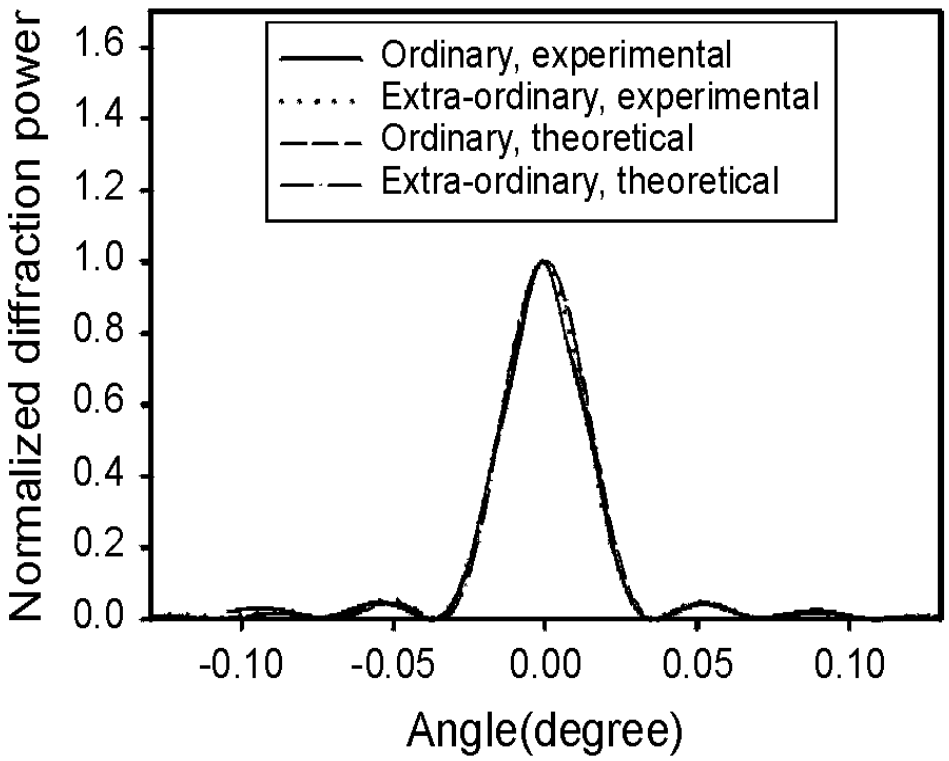

Fig. 2-15. Experimentally measured and theoretically calculated angular selectivities for one transmission geometry crystal with both extraordinary and ordinary polarizations. No apparent difference between the angular selectivities of the two cases is seen.

as many holograms as the angular selectivity allows. In reality, the number of holograms that can be multiplexed in a $LiNbO_3$ crystal is limited by the dynamic range M/# and not by the angular selectivity. As a quantitative example, consider a 1 cm X 1 cm X 1 cm $LiNbO_3$ crystal with M/# = 10 for recording wavelength $\lambda = 532$ nm. Also, assume that the minimum acceptable diffraction efficiency of each hologram is $\eta_{min} = 10^{-4}$. This allows the multiplexing of M = 1000 in the crystal. If we use angular multiplexing and allow a range of 40 degrees for the variation of the angle of the reference beam outside the crystal, we

need to put the reference beams of the different holograms 40/1000 = 0.04 ^{o} apart. The angular selectivity of the crystal for the 90-degree geometry is 532 nm/1 cm = 5.32 X 10^{-5} radians = 0.003 ^{o}. This selectivity allows for the recording of much more than 1000 holograms. Thus, with current values of M/#, angular selectivity is not a limiting factor in angularly multiplexing of holograms in $LiNbO_3$ crystals. Therefore, for dynamic range limited holographic storage system, transmission geometry offers a higher storage capacity than the 90-degree geometry.

2.6 Discussions

The results presented in the previous sections suggest that transmission geometry is a better choice for holographic storage mainly due to its higher dynamic range (M/#) and sensitivity. The main advantages of the 90-degree geometry are insensitivity to holographic scattering and fanning[2-3][2-7][2-10] as well as the possibility of designing compact memory modules.[2-27]

Strong fanning in sensitive singly-doped $LiNbO_3$ crystals has been a major obstacle in the implementation of holographic memories in transmission geometry. All the read-write memory systems demonstrated to date use the 90-degree geometry to avoid fanning, thereby sacrificing both M/# and S. The holograms recorded using both geometries are not persistent, i.e., they are erased during read-out. Recently, two-center recording has been proposed as a method for recording persistent holograms in doubly-doped $LiNbO_3$ crystals.[2-23][2-24] Two-center recording is a special case of gated holographic recording[2-28][2-29][2-30] in which a hologram is recorded by two recording beams only when a sensitizing (or gating) beam is present. The hologram is read by one of the recording

beams with sensitizing beam absent. Therefore, the holograms are not erased during read-out. In addition to persistence, gated holographic recording reduces the fanning and holographic recording considerably. Holographic scattering and fanning are highly suppressed in two-center recording both during recording phase (due to the presence of the sensitizing beam) and during reading phase (due to the insensitivity of the crystal to the reading wavelength in absence of the sensitizing beam. Therefore, the advantage of the 90-degree over the transmission geometry disappears in two-center recording.

Another advantage of the 90-degree geometry is that the reference and signal beams propagate in two perpendicular directions. This allows the design of compact architectures for holographic memory module.[2-27] It also makes the implementation of the phase-conjugate read-out much easier compared to transmission geometry.[2-31][2-32]

The choice of the recording geometry involves a trade-off between the larger capacity and sensitivity on one hand and the architecture design on the other hand. If maximum capacity and speed is the first priority, transmission geometry with more sophisticated architecture must be chosen. However, for compact low-cost holographic memory module, the 90-degree geometry is a better choice at the expense of reduction in storage capacity and speed.[2-27]

2.7 Conclusions

The system performances of two holographic recording geometries (the 90-degree and transmission geometries) using iron-doped lithium niobate were compared here. The comparison was based on dynamic range (M/#), sensitivity, scattering noise, inter-pixel noise, and storage capacity. The M/# and sensitivity are larger in transmission geometry

than those in the 90-degree geometry. The measured M/# and sensitivity of transmission geometry are 10 times as large as those of the 90-degree geometry for $LiNbO_3$:Fe crystals with almost same doping levels and oxidation states available in our labs. Three factors contribute to the larger M/# and sensitivity in transmission geometry: smaller K-vector, larger effective electrooptic coefficient γ_{eff}, and higher average modulation depth. Although the scattering noise level in transmission geometry is larger, considering the remarkable gain in the M/#, the signal to scattering noise ratio (SSNR) is better in transmission geometry than that in the 90-degree geometry. The inter-pixel noises of the 90-degree and transmission geometries are comparable. Although the angular selectivity in the 90-degree geometry is higher, for dynamic range limited holographic storage system, transmission geometry has higher capacity than the 90-degree geometry.

2.8 Appendix: Derivation of the model of M/# in transmission geometry

The main purpose of this appendix is to develop a theoretical model of M/# in $LiNbO_3$:Fe for transmission geometry using extraordinary polarization. The procedure of the derivation is similar to that in Ref. [2-14].

Figure 2-16 shows the coordinate system of transmission geometry. We assume that the dimension along y direction is infinite. The c-axis of the crystal is along x direction and the thickness is L. For the sake of simplification, we consider the case in which the two recording beams illuminate the crystal symmetrically and the reference beam covers the signal beam inside the crystal. The incident angles for both reference and signal beams are θ. Extraordinary polarization is used for both signal and reference beams. As shown in

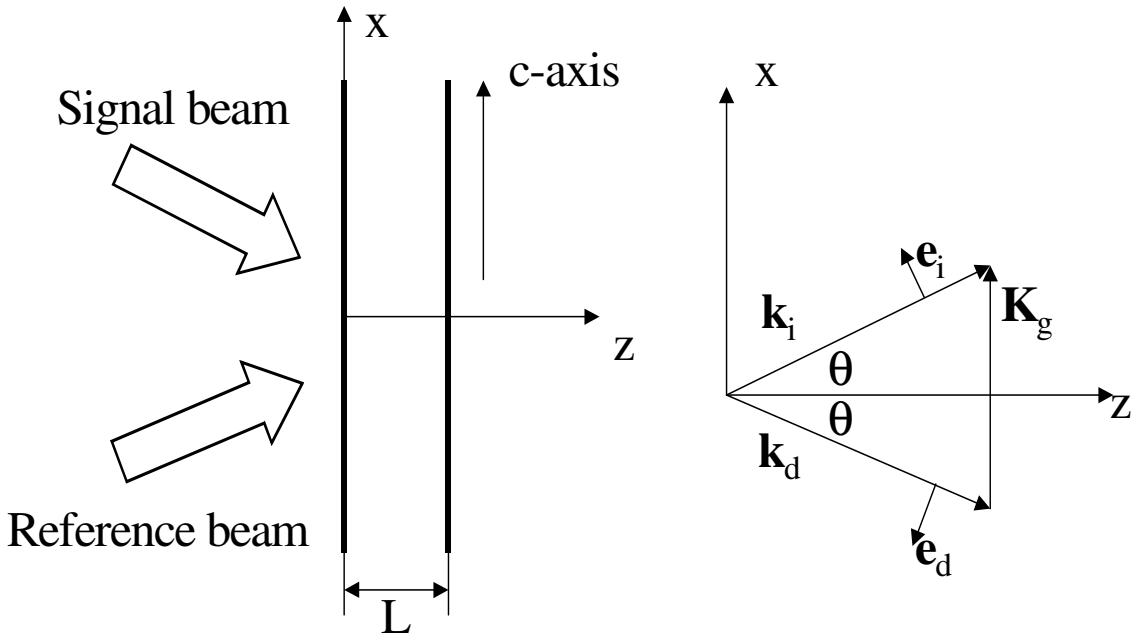

Fig. 2-16. Transmission geometry.

Figure 2-16, $\mathbf{k}_i$, $\mathbf{k}_d$, $\mathbf{K}_g$, $\mathbf{e}_i$, and $\mathbf{e}_d$ are wave vector of reference beam, wave vector of signal beam, grating vector, unit polarization vector of reference beam, and unit polarization vector of signal beam, respectively.

Using the Born approximation, we have

$$\mathbf{E}_d = \mathbf{S}\iint dk_{dx}dk_{dy}A(\mathbf{k}_i, \mathbf{k}_d)\exp(j\mathbf{k_d} \bullet \mathbf{r}), \tag{2-18}$$

where

$$A(\mathbf{k}_i, \mathbf{k}_d) \equiv \iiint \frac{\Delta\varepsilon(\mathbf{r}')R_0 S_\alpha(\mathbf{r}')\exp(j\mathbf{k}_i \bullet \mathbf{r}')\exp(-j\mathbf{k}_d \bullet \mathbf{r}')}{2j\sqrt{k^2 - k_{dx}^2 - k_{dy}^2}} d\mathbf{r}', \tag{2-19}$$

$$\mathbf{S} = \frac{\mathbf{K}_g \bullet \mathbf{e}_i}{\varepsilon_0}(\mathbf{k}_i + \mathbf{K}_g) - \omega^2\mu_0\mathbf{e}_i, \tag{2-20}$$

and

$$\Delta\varepsilon(\mathbf{r}') = \Delta\varepsilon_1(\mathbf{r}')\exp(j\mathbf{k}_s \bullet \mathbf{r}')\exp(-j\mathbf{k}_j \bullet \mathbf{r}'). \tag{2-21}$$

Here $\mathbf{k}_s$, $\mathbf{k}_j$ are the wave vectors of the signal and reference beams, respectively, used for recording, R_0 is the amplitude of reference beam, S_α is the local constant related to absorption. Since we are interested in the diffraction efficiency when using a Bragg-matched reference beam, we can cancel all the phase terms by setting $\mathbf{k}_i = \mathbf{k}_j$, $\mathbf{k}_d = \mathbf{k}_s$. The first of these corresponds to the Bragg-matching condition; the second means that the integral now represents only the light diffracted in the direction of the original signal plane wave. Then we have:

$$\mathbf{S} = \frac{\mathbf{K}_g \bullet \mathbf{e}_i}{\varepsilon_0}(\mathbf{k}_i + \mathbf{K}_g) - \omega^2\mu_0\mathbf{e}_i = \omega^2\mu_0\cos(2\theta)\mathbf{e}_s = \frac{k_0^2}{\varepsilon_0}\cos(2\theta)\mathbf{e}_s, \tag{2-22}$$

$$\Delta\varepsilon_1(\mathbf{r}') = -\varepsilon_0 n_e^4 r_{33} E_1(\mathbf{r}'), \tag{2-23}$$

$$E_d = -\frac{k_0 n_e^3 r_{33}}{2j\cos\theta}\cos(2\theta)\exp(jk_0 x\sin\theta + jk_0 x\sin\theta)R_0\int_0^L S_\alpha(z)E_1(z)dz, \tag{2-24}$$

where

$$S_\alpha(z) \equiv \exp\left(-\frac{\alpha L}{2\cos\theta}\right). \tag{2-25}$$

The initial evolution of $E_1(z)$ can be obtained by solving the linearized Kukhtarev equations as:

$$E_1(z) = m(z)E_{sc}\left[1 - \exp\left(-\frac{t}{\tau_1(z)} - j\omega_1(z)t\right)\right], \tag{2-26}$$

where

$$m(z) \equiv \frac{2S_0W_0}{S_0^2 + W_0^2} \equiv m, \tag{2-27}$$

$$E_{sc} = E_q \sqrt{\frac{E_{ph}^2 + E_D^2}{[(N_A/N_D) \times E_{ph}]^2 + (E_D + E_q)^2}}, \tag{2-28}$$

$$\tau_l(z) = \tau_{di}(z) \frac{1 + (E_D/E_\mu)}{1 + (E_D/E_q)} = \frac{\tau_x}{I_0(z)}, \tag{2-29}$$

$$\omega_l(z) = \frac{1}{\tau_{di}(z)} \frac{N_A Eph}{N_D E_q} \frac{1}{1 + (E_D/E_\mu)}, \tag{2-30}$$

$$\tau_{di}(z) = \frac{\varepsilon}{q\mu s I_0 (N_D - N_A)} \frac{\gamma_R N_A}{} \exp\left(\frac{\alpha z}{\cos\theta}\right). \tag{2-31}$$

Plugging all the terms into Equation (2-24) we obtain the initial slope of diffraction efficiency during recording as:

$$\left.\frac{d\sqrt{\eta(t)}}{dt}\right|_{t=0} \equiv \left.\frac{d}{dt}\left(\frac{|E_d|}{R_0}\right)\right|_{t=0} \tag{2-32}$$
$$= \frac{S_0 W_0 k_0 n_e^3 r_{33} \cos(2\theta)}{2\alpha\tau_x} \left[\exp\left(-\frac{\alpha L}{2\cos\theta}\right) - \exp\left(-\frac{3\alpha L}{2\cos\theta}\right)\right] \frac{E_q \sqrt{E_{ph}^2 + E_D^2}}{E_D + E_q}$$

During the erasure, the evolution of diffraction efficiency is:

$$\eta(t) \propto \int_0^L \exp\left(-\frac{\alpha z}{\cos\theta}\right) \exp\left(-\frac{2t}{\tau_x} I_0(z)\right) dz \tag{2-33}$$

The erasure time constant τ_e can be obtained approximately by:

$$\frac{2}{\tau_e} \equiv \frac{-\left.\frac{d\eta}{dt}\right|_{t=0}}{\eta|_{t=0}} = \frac{I_0}{\tau_x}\left[1 + \exp\left(-\frac{\alpha z}{\cos\theta}\right)\right]. \tag{2-34}$$

Therefore, the M/# in transmission geometry is:

$$M/\# \equiv \left(\left. \frac{d\sqrt{\eta(t)}}{dt} \right|_{t=0} \right) \times \tau_e \quad . \tag{2-35}$$

$$= \frac{k_0 n_e^3 r_{33} \cos(2\theta)}{2} \frac{m\left[\exp\left(-\frac{\alpha L}{2\cos\theta}\right) - \exp\left(-\frac{3\alpha L}{2\cos\theta}\right)\right]}{\alpha\left[1 + \exp\left(-\frac{\alpha L}{\cos\theta}\right)\right]} \frac{E_q \sqrt{E_{ph}^2 + E_D^2}}{E_D + E_q}$$

Obviously, in transmission geometry using extraordinary polarization, we have:

$$r_{eff} \equiv r_{33} \cos(2\theta) , \tag{2-36}$$

and

$$M_3(m) \equiv m \times \frac{\left[\exp\left(-\frac{\alpha L}{2\cos\theta}\right) - \exp\left(-\frac{3\alpha L}{2\cos\theta}\right)\right]}{\alpha\left[1 + \exp\left(-\frac{\alpha L}{\cos\theta}\right)\right]} . \tag{2-37}$$

References

[2-1] F. Mok, M. Tackitt, and H. Stoll, "Storage of 500 high-resolution holograms in a $LiNbO_3$ crystal," Opt. Lett. **8**, 605-607 (1991).

[2-2] G. Rakujic, V. Levya, and A. Yariv, "Optical data storage by using wavelength multiplexed volume holograms," Opt. Lett. **17**, 1471-1473 (1992).

[2-3] F. Mok, "Angle-multiplexed storage of 5,000 holograms in lithium niobate," Opt. Lett. **18**, 915-917 (1993).

[2-4] J. F. Heanue, M. C. Bashaw, and L. Hesselink, "Volume holographic storage and retrieval of digital data," Science **265**, 749-752 (1994).

[2-5] D. Psaltis and F. Mok, "Holographic memories," Sci. Am. **273,** 70-76 (1995).

[2-6] J. H. Hong, I. McMichael, T. Y. Chang, W. Christian, and E. G. Paek, "Volume holographic memory system: techniques and architectures," Opt. Eng. **34**, 2193-2203 (1995).

[2-7] G. Burr, F. Mok and D. Psaltis, "Angle and space multiplexed holographic storage using the 90-degree geometry," Opt. Comm. **117**, 49-55 (1995).

[2-8] I. McMichael, W. Christian, D. Pletcher, T. Y. Chang, and J. H. Hong, "Compact holographic storage demonstrator with rapid access," Appl. Opt. **35**, 2375-2379 (1996).

[2-9] R. M. Shelby, J. A. Hoffnagle, G. W. Burr, C. M. Jefferson, M.-P. Bernal, H. Coufal, R. K. Grygier, H. Gunther, R. M. Macfarlane, and G. T. Sincerbox, "Pixel-matched holographic data storage with megabit pages," Opt. Lett. **22**, 1509-1511 (1997).

[2-10] X. An, D. Psaltis, and G. Burr, "Thermal fixing of 10,000 holograms in $LiNbO_3:Fe$," Appl. Opt. **38**, 386-393 (1999).

[2-11] C. Denz, G. Pauliat, G. Roosen, and T. Tschudi, "Volume hologram multiplexing using a deterministic phase encoding method," Opt. Comm. **85**, 171-176 (1991).

[2-12] K. Curtis, A. Pu, and D. Psaltis, "Method for holographic storage using peristrophic multiplexing," Opt. Lett. **19**, 993-994 (1994).

[2-13] D. Psaltis, M. Levene, A. Pu, G. Barbastathis, and K. Curtis, "Holographic storage using shift multiplexing," Opt. Lett. **20**, 782-784 (1995).

[2-14] G. Burr, *Volume holographic storage using the 90^o geometry*, Ph.D Thesis, California Institute of Technology, 1996.

[2-15] K. Peithmann, A. Wiebrock, and K. Buse, "Photorefractive properties of highly-doped lithium niobate crystals in the visible and near-infrared," Appl. Phys. **B 68**, 777-784 (1999).

[2-16] I. Nee, M. Muller, K. Buse, and E. Kratzig, "Role of iron in lithium-niobate crystals for the dark-storage time of holograms," J. Appl. Phys. **88**, 4282-4286 (2000).

[2-17] Y. Yang, I. Nee, K. Buse, and D. Psaltis, "Ionic and electronic dark decay of holograms in $LiNbO_3$:Fe crystals," Appl. Phys. Lett. **78**, 4076-4078 (2001).

[2-18] Y. Yang, K. Buse, and D. Psaltis, "Photorefractive recording in $LiNbO_3$:Mn," Opt. Lett., **27**, 158-160 (2002).

[2-19] D. Psaltis, D. Brady, and K. Wagner, "Adaptive optical networks using photorefractive crystals," Applied Optics, **27**, 1752-1759 (1988).

[2-20] F. Mok, G. Burr, and D. Psaltis, "System metric for holographic memory systems," Opt. Lett. **21**, 896-898 (1996).

[2-21] N. V. Kukhtarev, V. B. Markov, S. G. Odulov, M. S. Soskin, and V. L. Vintekii, "Holographic storage in electrooptic crystals, 1. steady-state," Ferroelectrics **22**, 949-960 (1979).

[2-22] P. Yeh, *Introduction to Photorefractive Nonlinear Optics*, John Wiley & Sons, Inc., 1993.

[2-23] K. Buse, A. Adibi, and D. Psaltis, "Non-volatile holographic storage in doubly doped lithium niobate crystals," Nature **393**, 665-668 (1998).

[2-24] A. Adibi, K. Buse, and D. Psaltis, "Two-center holographic recording," JOSA B **18**, 584-601 (2001).

[2-25] X. Yi, P. Yeh, and C. Gu, "Statistical-analysis of cross-talk noise and storage capacity in volume holographic memory," Opt. Lett. **19**, 1580-1582 (1994).

[2-26] M. P. Bernal, G. W. Burr, H. Coufal, and M. Quintanilla, "Balancing interpixel cross talk and detector noise to optimize areal density in holographic storage systems," Appl. Opt. **37**, 5377-5385 (1998).

[2-27] J.-J. P. Drolet, E. Chuang, G. Barbastathis, and D. Psaltis, "Compact, integrated dynamic holographic memory with refreshed holograms," Opt. Lett. **22**, 552-554 (1997).

[2-28] D. von der Linde, A. M. Glass, and K. F. Rodgers, "Multiphoton photorefractive processes for optical storage in $LiNbO_3$," Appl. Phys. Lett. **25**, 155-157 (1974).

[2-29] H. Guenther, R. Macfarlane, Y. Furukawa, K. Kitamura, and R. Neurgaonkar, "Two--color holography in reduced near--stoichiometric lithium niobate," Appl. Opt. **37**, 7611-7623 (1998).

[2-30] L. Hesselink, S. S. Orlov, A. Liu, A. Akella, D. Lande, and R. R. Neugaonkar, "Photorefractive materials for nonvolatile volume holographic data storage," Science **282**, 1089--1094 (1998).

[2-31] W. Liu, and D. Psaltis, "Pixel size limit in holographic memories," Opt. Lett. **24**, 1340-1342 (1999).

[2-32] G. W. Burr, and I. Leyva, "Multiplexed phase-conjugate holographic data storage with a buffer hologram," Opt. Lett. **25**, 499-501 (2000).

3 Dark decay mechanisms in lithium niobate crystals

3.1 Introduction

Photorefractive materials have been widely investigated for applications of holographic data storage [3-1][3-2] and optical add/drop filters for optical telecommunications.[3-3]-[3-5] Inhomogeneous illumination of these materials redistributes charge, builds up internal electric fields and so changes the refractive index. Usually, inhomogeneous illumination is generated by interfering two coherent light beams inside these materials, of which one is called reference beam, the other is called signal beam. Subsequent illumination with one light beam that satisfies the Bragg condition results in light diffraction and reconstructs the information encoded in the original interference pattern. A variety of inorganic and organic photorefractive materials are known, among which inorganic oxide $LiNbO_3$ crystals have been of intense interest due to their reversibility, moderate sensitivity, and availability in large size and good quality.

One of the most important issues of photorefractive materials is volatility: the stored information decays with time, either under the illumination of readout beam or in the dark. The same mechanism as photorefractive recording is responsible for the volatility under the illumination of readout and several techniques, such as thermal fixing, electrical fixing, two-color recording, and two-center recording, have been developed to deal with this kind of volatility.[3-6]-[3-9] While the issue of volatility due to optical erasure of read-

out illumination has been addressed intensively, there have been only a few literatures dealing with the volatility in the dark, i.e., dark decay, partly due to the fact that dark decay rate is relatively slow and the issue of dark decay is not so urgent. Nevertheless the issue of dark decay is very important, especially for optical add/drop filters, where the main source of volatility is dark decay because the wavelengths of light used in telecommunications are around 1.5 μm and this kind of infra-red illumination causes little optical erasure. Furthermore, it is desirable to have lithium niobate crystals with high doping level to obtain large dynamic range and high sensitivity, but it is known that in iron-doped lithium niobate crystals with doping levels above 0.3 wt% Fe_2O_3 the dark decay time constant, i.e., lifetime of hologram in the dark, is just a few minutes , which is too short for practical applications. A good understanding of dark decay mechanisms in lithium niobate crystals is needed to improve the dark decay and tailor the material parameters to obtain optimal system performance for $LiNbO_3$-based holographic data storage system and optical add/drop filters for optical telecommunications.

Recently it has been found that in the dark and at room temperature electron tunneling between iron sites occurs in highly-doped lithium niobate crystals and is the dominant mechanism of dark decay in these crystals. [3-10][3-14] It is generally accepted that in the temperature range between 150 and 200^{o}C the proton conductivity is enlarged by several orders of magnitude compared to that at room temperature. This behavior is used for thermal fixing.[3-15][3-16] Although the proton conductivity at room temperature is very small, the same mechanism of thermal fixing, i.e., proton compensation, is the major source of dark decay in lithium niobate crystals with low doping levels.[3-10] For temperatures higher than 200^{o}C, excitation of electrons into the conduction band is supposed to be

another main process of dark decay.[3-16] Up to now the thermal activation energy of the electron tunneling process is unknown. A study of the process at and close to room temperature is of special importance. Lifetime estimates of holograms stored in lithium niobate are frequently based on extrapolation of high temperature data. This is risky because proper thermal activation energies must be used. In this chapter, the dark decay mechanisms of non-fixed holograms in lithium niobate crystals with different dopants, doping levels and oxidation states in the range of temperature from room temperature to 180°C are investigated.

3.2 Dark decay mechanisms in lithium niobate crystals

3.2.1 Fundamentals

The characteristic relaxation time constant of a macroscopic electric field due to dark conduction, τ_d, is related to the dark conductivity σ_d as:

$$\tau_d = \varepsilon\varepsilon_0 / \sigma_d \tag{3-1}$$

where $\varepsilon\varepsilon_0$ is the dielectric constant. For single dark decay mechanism, dark conductivity σ_d can be calculated by:

$$\sigma_d = q\mu n \tag{3-2}$$

where q is the absolute value of the electron charge, μ is the mobility of the charge carrier responsible for dark decay, and n is the concentration of charge carrier.

If there are more than one mechanism that contributes to the dark decay with the dark conductivities σ_{d1}, σ_{d2}, σ_{d3}, ..., and characteristic relaxation time constants τ_{d1}, τ_{d2},

τ_{d3}, ..., then the dark conductivity is the sum of the conductivities of each dark decay mechanism:

$$\sigma_d = \sigma_{d1} + \sigma_{d2} + \sigma_{d3} + \dots \tag{3-3}$$

and the overall characteristic relaxation time constant τ_d is related to the individual characteristic time constant as:

$$\frac{1}{\tau_d} = \frac{1}{\tau_{d1}} + \frac{1}{\tau_{d2}} + \frac{1}{\tau_{d3}} + \dots \tag{3-4}$$

The temperature dependence of the dark conductivity σ_d has been investigated in a number of experimental papers.[3-15][3-16] Typically a so-called Arrhenius law is observed for this temperature dependence:

$$\sigma_d = \sigma_0 \exp\left(-\frac{E_a}{k_B T}\right) \tag{3-5}$$

where E_a is activation energy, k_B is Boltzman constant, T is absolute temperature, and σ_0 is pre-exponential conductivity factor.

Different dark decay mechanism has different activation energy. We can use the characteristic activation energy to differentiate dark decay mechanism. Furthermore, the pre-exponential factor of Arrhenius law is directly proportional to the concentration of the charge carriers. We can also extract some useful information of dark decay mechanism if we can manipulate the concentration of the charge carrier responsible for the dark decay.

3.2.2 Thermal fixing and proton compensation

In lithium niobate crystals grown by Czochralski method hydrogen is often present forming hydroxyl ions (OH^-) with oxygen. It is assumed that the incorporated hydrogen ion, i.e., proton, is responsible for the reduction of photorefractive laser damage and the

thermal fixing of holograms in lithium niobate crystals. In interpreting the low-high-low thermal fixing of holograms Amodei and Staebler suggested that ions become mobile at elevated temperature above 150^{o}C and compensate the modulated electronic space charge fields which are recorded at room temperature previously.[3-15] For low-high-low thermal

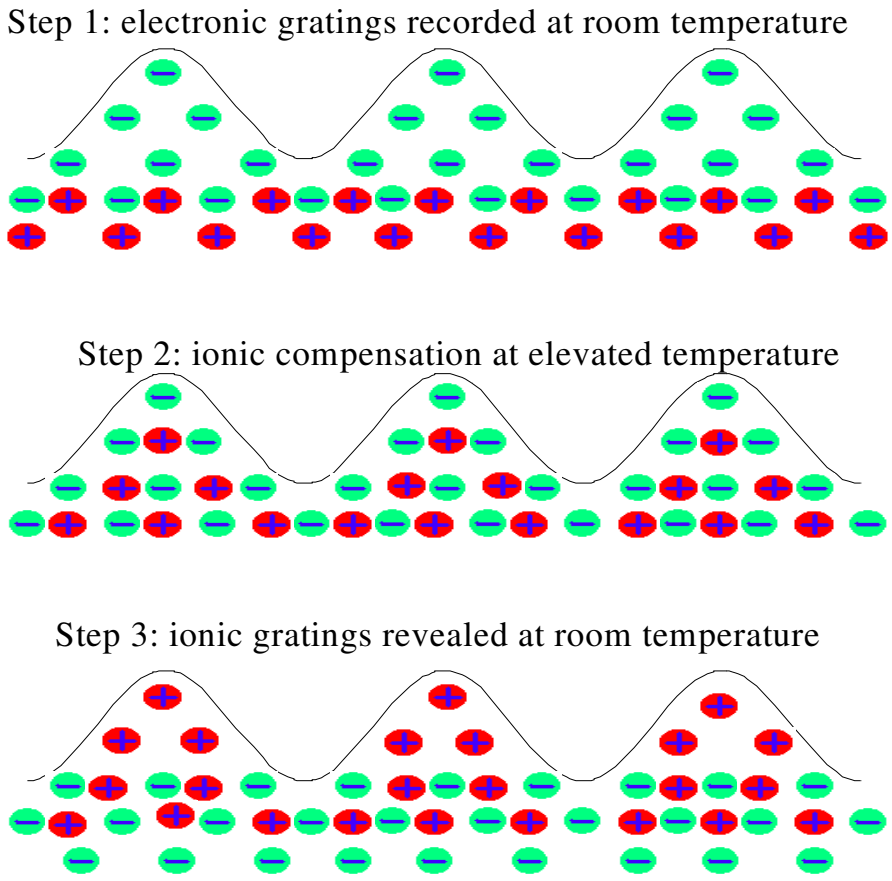

Fig. 3-1. Low-high-low thermal fixing of holograms in photorefractive lithium niobate crystal. Ionic compensation at room temperature is one of the dark decay mechanisms.

fixing, after electronic gratings are recorded at room temperature, the crystal is heated to an elevated temperature and kept at the elevated temperature for some time. Then the crystal is cooled down to room temperature and uniform illumination is used to erase the electronic

gratings and leave the ionic gratings, which are stable against erasure during readout at room temperature. These ions were identified as protons by spatially resolved infra-red absorption. Figure 3-1 shows that process of thermal fixing.

It is found that the mobility of proton in lithium niobate crystals follows an Arrhenius-like behavior with an activation energy 1.0-1.2eV:

$$\mu = \mu_0 \exp\left(-\frac{E_a}{k_B T}\right) \tag{3-6}$$

where E_a is activation energy, k_B is Boltzman constant, T is absolute temperature, and μ_0 is pre-exponential mobility factor which is expressed as:

$$\mu_0 = \frac{q}{k_B T} \times D_0 \tag{3-7}$$

where D_0 is diffusion constant, a virtually constant. The rate of proton compensation at room temperature is much smaller than that at elevated temperature and is directly proportional to the concentration of protons. This proton compensation is the main dark decay mechanism in lithium niobate crystals with low doping levels.

The concentration of proton in lithium niobate crystals can be obtained from the measurement of infra-red absorption around 2870 nm. Figure 3-2 shows a typical absorption spectrum of an as grown lithium niobate crystal around 2870nm, which is the infra-red absorption band of the OH^- stretching vibration. The concentration of protons in lithium niobate crystals is calculated as:

$$c_{OH^-} = c_{H^+} = (1.67 \pm 0.09) \times 10^{22} m^{-2} \alpha_{2870nm} \tag{3-8}$$

where α_{2870nm} is the absorption coefficient at 2870 nm (Ref. [3-17]).

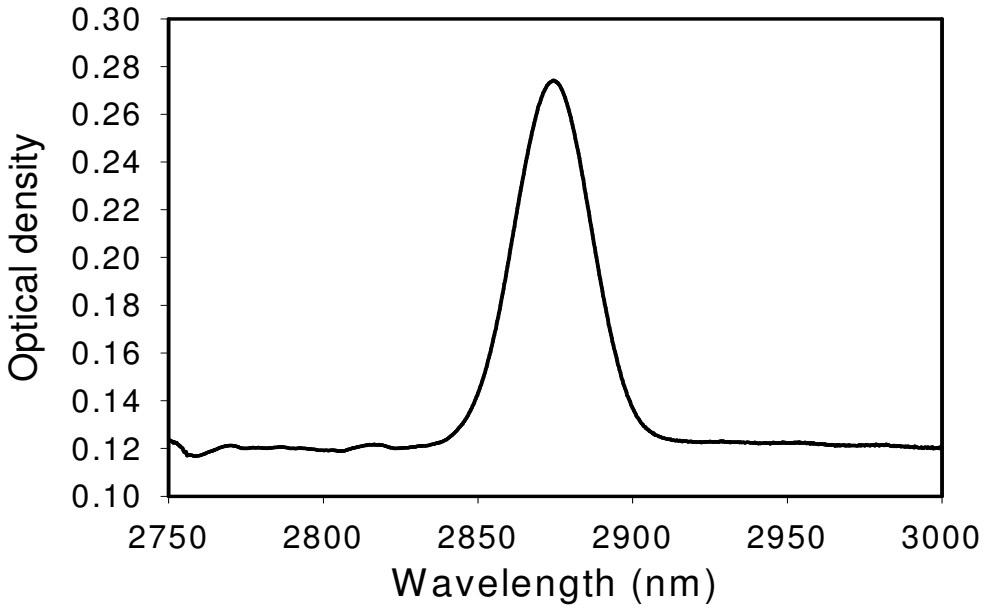

Fig. 3-2. Typical absorption spectrum of an as-grown lithium niobate crystal around 2870nm.

3.2.3 Thermally excited electrons

In thermal equilibrium in the dark the concentration of electrons that are thermally excited from dopants into the conduction band of semiconductors obeys Boltzman distribution:

$$n = n_0 \times \exp\left(-\frac{E_g}{k_B T}\right) \tag{3-9}$$

where E_g is the energy gap between the energy levels of dopants and conduction band, k_B is Boltzman constant, T is absolute temperature, and n_0 is the pre-exponential factor. It is known that the pre-exponential factor n_0 of thermally excited electrons is directly propor-

tional to the concentration of donors (filled traps) and inversely proportional to the concentration of acceptors (empty traps). The conductivity due to thermally excited electrons in the conduction band will cause the dark decay and can be represented as:

$$\sigma = C\mu(T)\frac{c_d}{c_a}\exp\left(-\frac{E_g}{k_B T}\right) \tag{3-10}$$

where C is some constant, $\mu(T)$ is the mobility of electrons in conduction band at temperature T, c_d is the concentration of donors and c_a is the concentration of acceptors.

Sturnman found that the effect of dark decay due to thermally excited electrons in lithium niobate crystals is remarkable and thermally excited electrons are competitive with protons within the temperature range 200-300^{o}C. [3-16] The activation energy of this process is 0.1-0.3eV. It is believed that the thermally excited electrons in this range of temperature are related to small polarons.

3.2.4 Electron tunneling

In doped semiconductors, it is possible that the electron of one donor tunnels through the potential barrier to an nearby acceptor. According to the theory of quantum mechanics, the probability of a particle's tunneling through a square potential barrier is:

$$p = \frac{16E(V-E)}{V^2}\exp\left[-\frac{4\pi L}{h}\sqrt{2m(V-E)}\right] \tag{3-11}$$

where h is the Plank's constant, m is the mass of the particle, E is the energy of the particle, V is the height of the barrier and L is the width of the barrier, as shown in Figure 3-3. In lithium niobate crystals the potential barrier between two nearby dopant sites is not exactly square and it is very hard to get the analytic formula of the probability of electron tunneling for doped lithium niobate crystals. Nevertheless, considering the fact that the average dis-

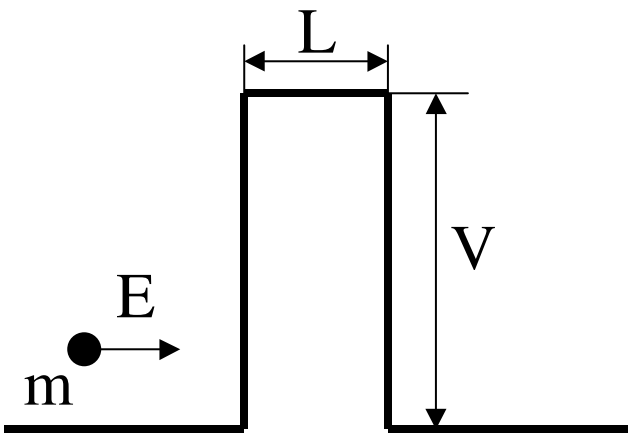

Fig. 3-3. Electron tunneling through a square potential barrier. The probability of tunneling will increase exponentially with the decrease of the width of barrier L.

tance between the nearby dopant sites in lithium niobate crystals with typical doping levels is much larger than the radius of dopants, the model of electron tunneling through a square potential barrier will more or less describe the reality. For example, the radius of ion Fe^{2+} is about 0.12 nm, while the average distance between nearby ion sites in lithium niobate crystal with doping level of 0.25 wt% Fe_2O_3 is about 21 nm. We would expect that the probability of electron tunneling between filled and empty traps will increase exponentially with the decrease of the average distance between nearby dopant sites.

Another characteristic of electron tunneling between dopant sites in lithium niobate crystals is that the probability of tunneling is proportional to the effective trap density which is defined as:

$$N_{eff} = 1 \Big/ \left(\frac{1}{c_X} + \frac{1}{c_{X^+}} \right) \tag{3-12}$$

where c_X is the density of filled traps, c_{X^+} is the density of empty traps. Intuitively, if there are too many filled traps and few empty traps, then electrons from the filled traps have

nowhere to tunnel and the probability is mostly determined by how many empty traps exist. On the other hand, if there are much more empty traps than filled traps, then there are no enough electrons from filled traps to tunnel and the probability is mainly determined by the density of filled traps.

3.3 Experimental setup and method

The experimental optical system that was used to measure dark decay time constants is shown in Figure 3-4. The recording light source was an Argon-ion laser operating at the wavelength of 514 nm. The raw laser beam was spatially filtered and collimated. An optical tunable attenuator was used to decrease the intensity of readout beam. After the optical attenuator is a set of half-wave plates and polarizing beam splitter. The first half-wave plate is used to adjust the power ratio of the beams that are reflected and transmitted by the subsequent polarizing beam splitter. Since a polarizing beam splitter transmits light with a polarization orthogonal to the reflected beam, the second half-wave plate is needed to rotate the beam reflected from the polarizing beam splitter such that the polarizations of both beams are the same. With this configuration, two beams, polarized parallel to the plane that contains them, were generated with a large amount of flexibility in their relative intensities. Extra-ordinary polarization was used for recording and readout because the recording speed and diffraction efficiency is larger than that of ordinary polarization for transmission geometry (See Chapter 2).

The crystals were placed on a heatable plate of a commercial cryostat whose temperature was controlled within 0.1 ^{o}C accuracy. The collimated laser beam with the wavelength of 514 nm was split into two equal-intensity extraordinarily polarized beams that

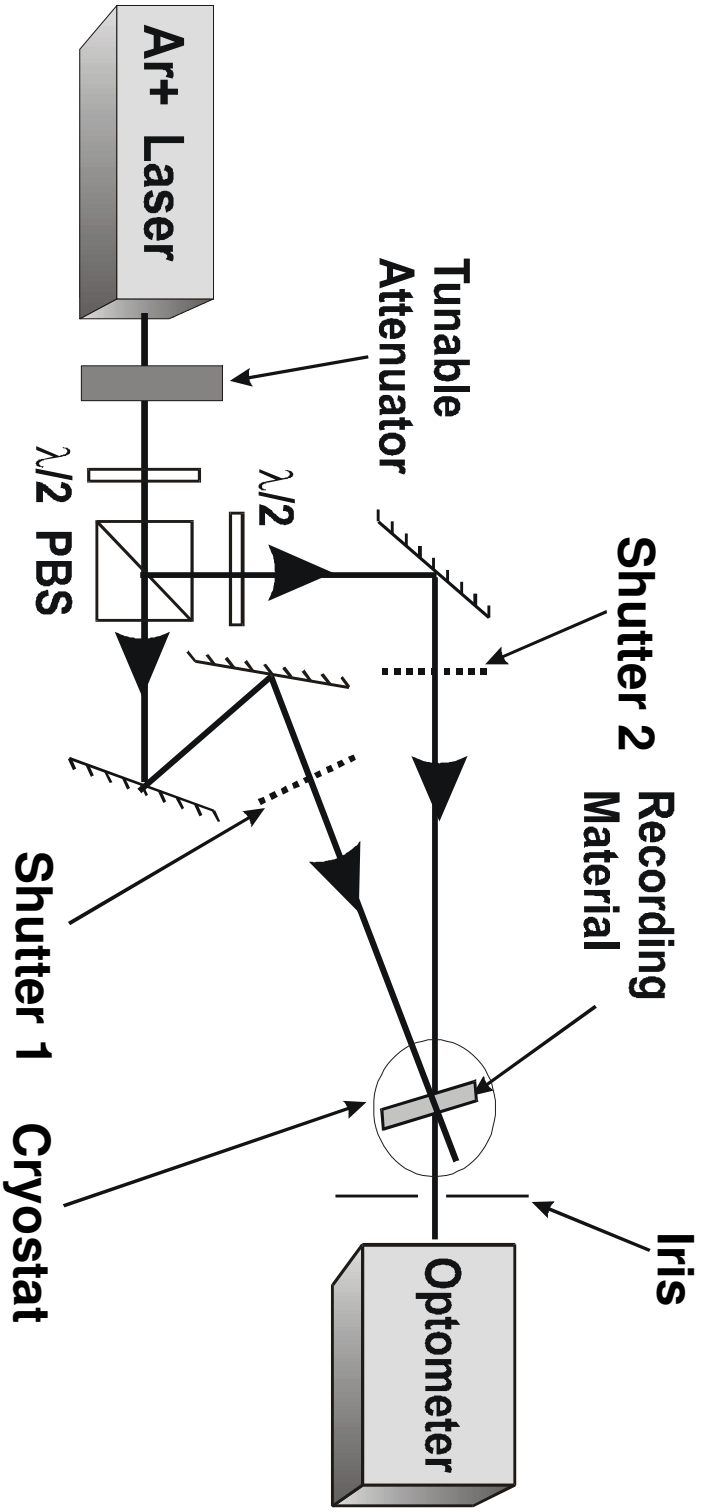

Fig. 3-4. Experimental optical system for measurement of dark decay time constants.

were expanded to cover the whole crystal during recording. The intensity of recording beam was 10 mW/cm^2 per beam. All recorded holograms had a grating period of 1.3 μm and were written with the grating vector oriented along the c-axis. Recording was always performed at room temperature. Afterwards, the crystals were heated to a certain elevated temperature in dark and a weak laser beam of 514 nm, of which the intensity is less than 10 μW/cm^2, was used to monitor the dark decay of holograms by measuring the holographic diffraction efficiency. The weak readout light illuminated the crystal only from time to time, and the intervals between two measurements were long enough to keep the erasure of the holograms by the probing beam negligible. After each experiment the crystal was heated to 230°C and kept at this temperature under uniform illumination for about 45 minutes to erase the gratings completely.

From the experimental data of diffraction efficiency (as a function of time), the dark decay time constants was extracted by fitting the data to the equation:

$$\eta(t) = \eta_0 \exp\left(-\frac{2t}{\tau_d}\right), \tag{3-13}$$

where $\eta(t)$ is the measured diffraction efficiency at time t, η_0 is the diffraction efficiency at $t = 0$, and τ_d is the fitted dark decay time constant. Figure 3-5 shows the typical dark decay curve, of which the temperature is 130°C. The dark decay measurement was repeated for each lithium niobate crystal at different temperature. The dark decay time constants were extracted and plotted as a function of reciprocal temperature 1000/T.

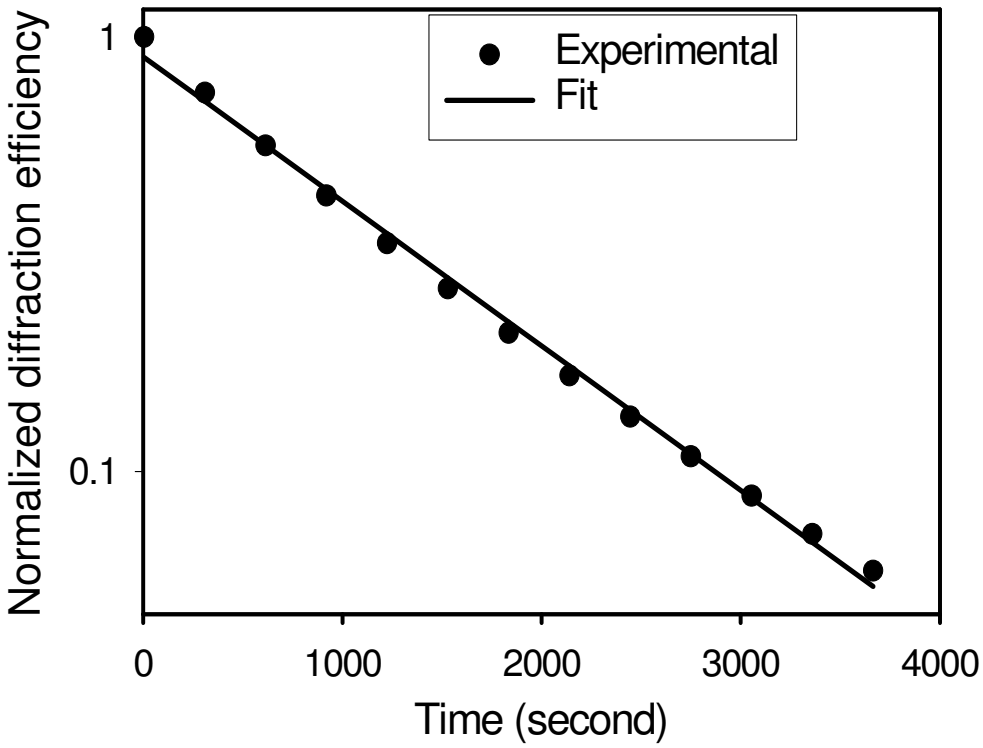

Fig. 3-5. Typical dark decay curve: normalized diffraction efficiency vs. time.

3.4 Experiments and results

3.4.1 Samples and thermal annealing

The lifetimes of non-fixed holograms in lithium niobate crystals with different dopants, different doping levels and different oxidation states have been measured in the temperature range from 30 to 180^{o}C. Congruently melting singly-doped lithium niobate samples were used. Table 3-1 summarizes some parameters of these samples. All these

crystals were x-cut and polished to optical quality. Thermal annealing in various atmo-

Table 3-1. Summary of parameters of the samples.

Sample	Doping level	Oxidation state	Notes
S1, LN:Fe	0.05 wt% Fe_2O_3	$c_{Fe^{2+}}/ c_{Fe^{3+}} = 0.05$	Proton-enriched
S2, LN:Fe	0.05 wt% Fe_2O_3	$c_{Fe^{2+}}/ c_{Fe^{3+}} = 0.21$	Proton-reduced
S3, LN:Mn	0.02 wt% MnO	Medium	As grown
S4, LN:Mn	0.1 wt% MnO	Reduced	Proton-reduced
S5, LN:Mn	0.1 wt% MnO	Oxidized	Proton-reduced
S6, LN:Fe	0.25 wt% Fe_2O_3	$c_{Fe^{2+}}/ c_{Fe^{3+}} = 0.10$	Proton-reduced
S7, LN:Fe	0.138 wt% Fe_2O_3	Variable	As grown
S8, LN:Fe	0.138 wt% Fe_2O_3	$c_{Fe^{2+}}/ c_{Fe^{3+}} = 0.03$	Proton-enriched
S9, LN:Fe	0.138 wt% Fe_2O_3	$c_{Fe^{2+}}/ c_{Fe^{3+}} = 0.03$	Proton-reduced

spheres or vacuum was used to achieve desired oxidation states and proton concentrations. For oxidation the samples were kept in an oven with oxygen atmosphere at elevated temperature, while for reduction the samples were heated to elevated temperature in atmosphere of argon. The duration and temperature of thermal annealing were controlled to obtain desired oxidation states. For proton enrichment, the samples were first annealed in the atmosphere of the mixture of argon and H_2O at around 1000^oC for hours, and then in the atmosphere of oxygen to oxidize the crystals. To reduce the concentration of proton, the samples were kept in vacuum at around 1000^oC for hours, then in dry oxygen to return to the desired oxidation states. The absorption coefficient at the maximum of the OH^- absorption band around 2870 nm is used to calculate the proton concentration.[3-13] Figure 3-6 shows the OH^- absorption spectra of three lithium niobate crystals with the same thickness of 1 mm: sample A is as grown, i.e., no proton reduction or enrichment, sample B is proton-

reduced and sample C is proton-enriched. As we can see from Figure 3-6, the thermal annealing described above to change the concentration of proton in lithium niobate crystals is efficient. The background of the absorption is due to Fresnel reflection. The calculated concentrations of proton in these samples are $3.01 \text{ X } 10^{24}/\text{m}^3$, $0.21 \text{ X } 10^{24}/\text{m}^3$ and $5.72 \text{ X } 10^{24}/\text{m}^3$ for sample A, B, C, respectively.

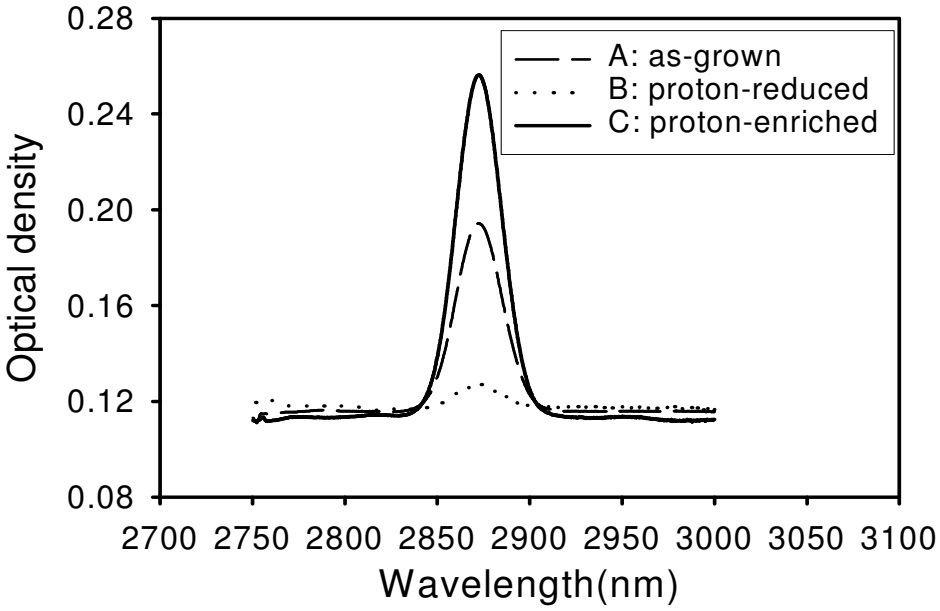

Fig. 3-6. OH^- absorption spectra of three lithium niobate crystals with the same thickness of 1 mm: sample A is as-grown, sample B is proton-reduced, and sample C is proton-enriched.

For $LiNbO_3$:Fe crystals, the Fe^{2+} concentration $c_{Fe^{2+}}$ can be calculated from absorption measurements around 477 nm. Figure 3-7 shows the absorption spectra of two $LiNbO_3$:Fe crystals for ordinary polarization. As we can see that there are obvious absorption peaks around 477nm due to the transition of electron from center Fe^{2+} to conduction

band. Sample D is more reduced than sample E. The formula used to calculate the Fe^{2+} concentration $c_{Fe^{2+}}$ is:

$$c_{Fe^{2+}} = 2.2 \times 10^{21} m^{-2} \times \alpha_{477nm} \quad (3\text{-}14)$$

where α_{477nm} is the absorption at 477 nm in m^{-1}.

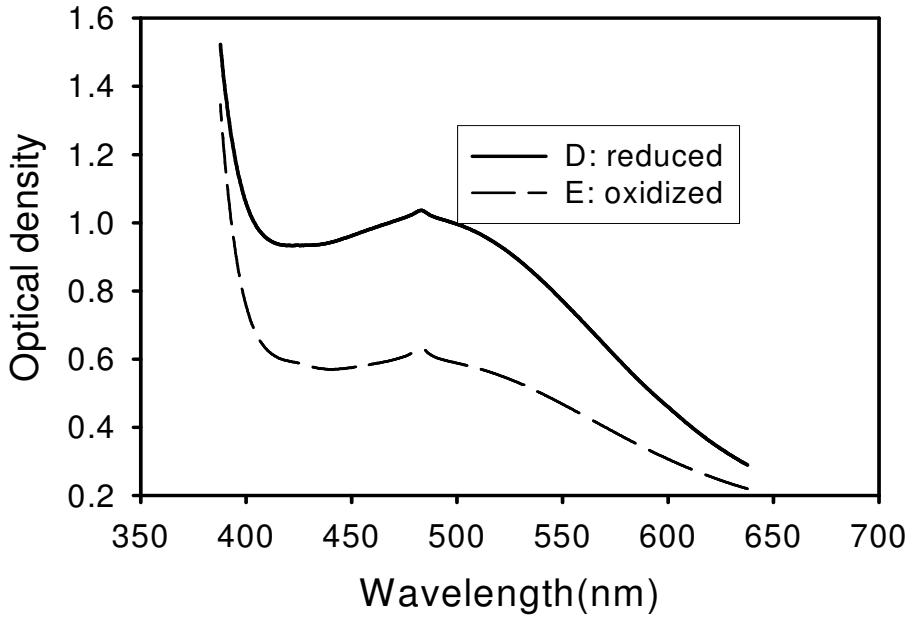

Fig. 3-7. Absorption spectra around 477 nm of two $LiNbO_3$:Fe crystals with different oxidation states: Sample D is more reduced than sample E.

For all $LiNbO_3$:Fe crystals used, the shape of the absorption spectra is the same, i.e., we avoid too strong reduction that generates, e.g., polaron and bipolaron bands. Thus the Fe^{2+} concentration $c_{Fe^{2+}}$ can be calculated from absorption measurements accurately. Because iron occurs only in the valence states 2+ and 3+, the concentration of Fe^{3+} is determined by subtracting $c_{Fe^{2+}}$ from the entire iron concentration c_{Fe}.

For $LiNbO_3$:Mn crystals, the oxidation states are difficult to determine quantitatively since their absorption spectrum are very broad and there is no apparent characteristic absorption band that can be used to calibrate the concentrations of Mn^{2+} or Mn^{3+}. Actually, this is one of the topics of Chapter 4.

3.4.2 Proton compensation: dark decay mechanism in lithium niobate crystals with low doping levels

Generally speaking, in lithium niobate crystals more than one mechanism will contribute to the dark decay and the overall dark conductivity is the sum of the conductivity of each dark decay mechanism. If there is no dominant mechanism, the dependence of dark decay time constant on temperature will not obey single Arrhenius law. However, there exist cases in which there is a dorminant dark decay mechanism, for example, in $LiNbO_3$:Fe crystals with doping levels less than 0.06 wt% Fe_2O_3. The dominant dark decay mechanism in these crystals has been identified as proton compensation.

The dark decay time constants of two $LiNbO_3$:Fe crystals with the doping level 0.05 wt% Fe_2O_3, S1 and S2, have been measured. Both samples were cut from the same boule. Sample S1 was proton-enriched while sample S2 was proton-reduced. Sample S1 was first annealed in the atmosphere of the mixture of argon and H_2O at 900^{o}C for 4 hours, and then in the atmosphere of argon at the same temperature for 4 hours. To reduce the concentration of proton of sample S2, the sample was kept in vacuum at 1000^{o}C for 14 hours, then in dry oxygen at the same temperature for 4 hours to return the desired oxidation states. Some material parameters of S1 and S2 are shown in Table 3-1. The measured proton concentrations of sample S1 and sample S2 were $5.5X10^{18}$ cm^{-3} and $3.1X10^{17}$ cm^{-3}, respectively.

The ratio of Fe^{2+} concentration and Fe^{3+} concentration of S1 and S2 are 0.05 and 0.21, respectively, which means that S1 is more oxidized than S2.

Figure 3-8 shows the measured dark decay time constants of these two crystals vs. reciprocal temperature 1000/T. The temperature ranges in which the dark decay time constants were measured were 40 to 140 °C for S1 and 70 to 180 °C for S2. The reason that the temperate ranges were different is that for S1 in the temperature above 140 °C the dark decay was too fast to obtain accurate measurement while for S2 in the temperature below 70 °C the dark decay was too slow.

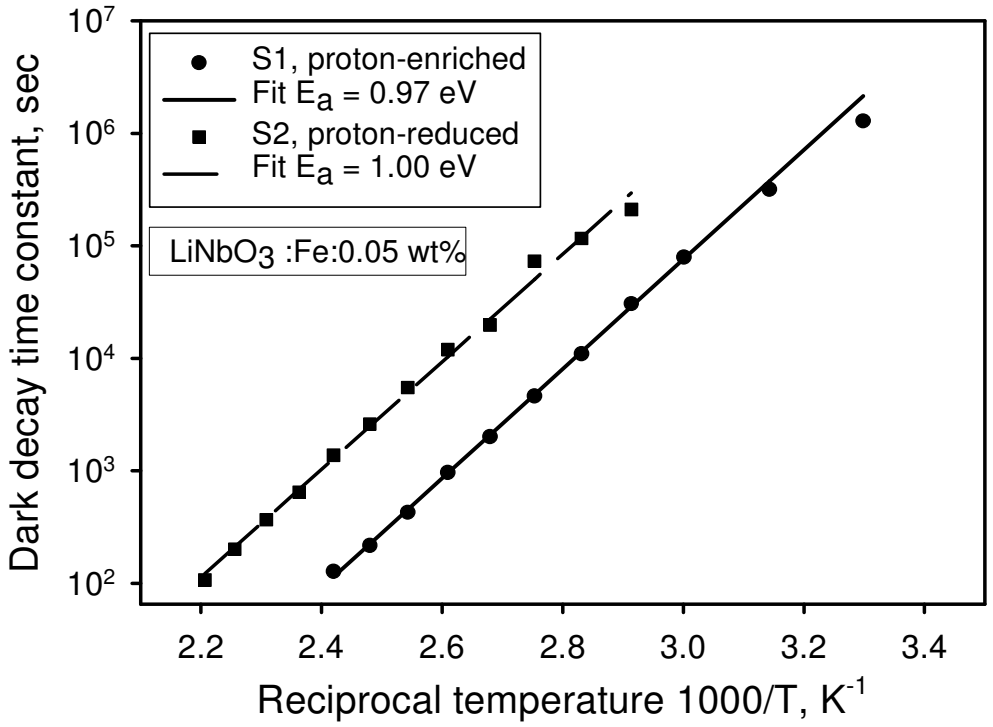

Fig. 3-8. Arrhenius plots of the dark decay time constants of holograms stored in $LiNbO_3$:Fe crystals with a doping level of 0.05 wt% Fe_2O_3, sample S1: proton-enriched, sample S2: proton-reduced.

From Figure 3-8 we can see that the time constants of both samples S1 and S2 obey an Arrhenius-type dependence on the absolute temperature T,

$$\tau = \tau_0 \exp\left(\frac{E_a}{k_B T}\right) \tag{3-15}$$

where τ_0 is the pre-exponential factor, k_B is the Boltzman constant, and E_a is the activation energy. The activation energies obtained for the samples S1 and S2 are almost the same, which means that there is only one dorminant dark decay mechanism in samples S1 and S2. There are several justifications that the dark decay in these two crystals is dominated by proton compensation of the electrical space-charge field. The activation energies obtained for the samples S1 and S2 are almost the same, 0.97 eV and 1.0 eV, respectively, and close to the proton activation energies reported in the literature.[3-15][3-18] The activation energy of 1.0 eV is a characteristic of proton process in lithium niobate crystals. The second reason that the dominant dark decay mechanism in samples S1 and S2 is proton compensation, which is more decisive, is that the ratio of the fitted pre-exponential factors for the samples S2 and S1 is 18.3 and is almost equal to the reciprocal ratio of the proton concentrations of these two samples, namely, 17.7. (See “Thermal fixing and proton compensation” on page 4.) Noting the fact that sample S2 is reduced much more than sample S1 but the pre-exponential factor of sample S1 is even less than that of sample S2, we can rule out the possibility that the dark decay is related to the iron-doping and electronic band transport since the time constant of the dark decay due to band transport should be inversely proportional to the oxidation state $c_{Fe^{2+}}/c_{Fe^{3+}}$.(See “Thermally excited electrons” on page 7.) We would like to emphasize the large range of temperatures used. Measurements were taken from room temperature to 180°C.

In lithium niobate crystals with low doping levels, the dominant dark decay mechanism is proton compensation and should be independent of dopant, doping level or oxidation state. The dark decay time constants in $LiNbO_3$:Mn and $LiNbO_3$:Ce crystals with different doping levels and oxidation states have been measured. Figure 3-9 shows the measured dark decay time constants of three $LiNbO_3$:Mn crystals S3, S4 and S5. Again, the time constants of these crystals obey an Arrhenius-type dependence on the absolute temperature with almost the same activation energy 1.00 eV, which is equal to that of

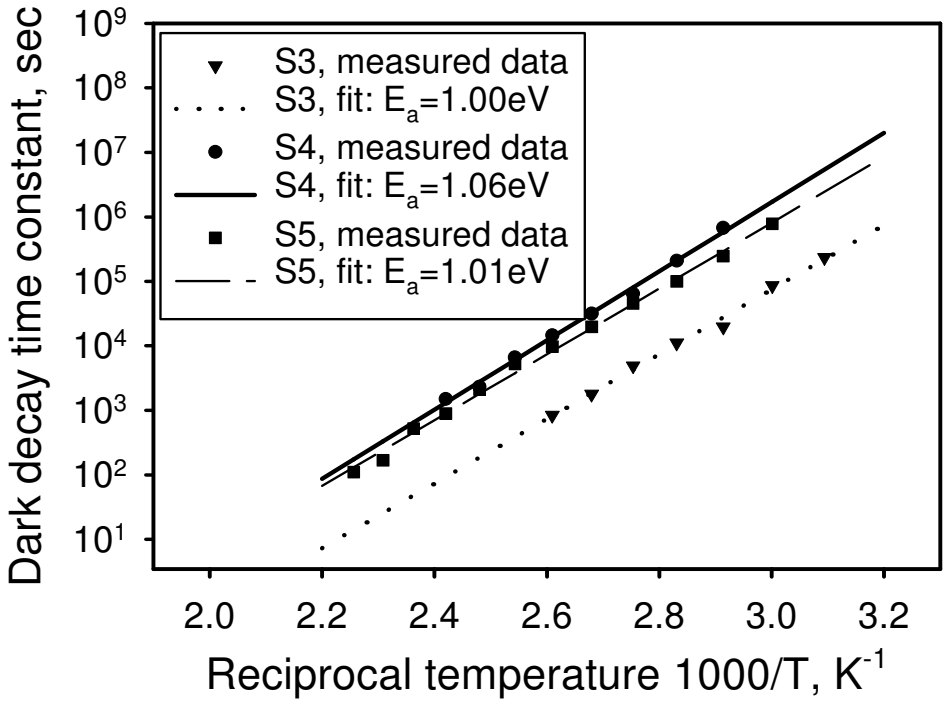

Fig. 3-9. Arrhenius plots of the dark decay time constants of holograms stored in $LiNbO_3$:Mn crystals. Sample S3: 0.02 wt% MnO, as grown; sample S4: 0.1 wt% MnO, proton-reduced; sample S5: 0.1wt% MnO, proton-reduced.

sample S1 and S2. The fitted pre-exponential factors of S3, S4 and S5 are inversely proportional to their proton concentrations. Notice that although the oxidation states of samples S4 and S5 have different oxidation states, the dark decay time constants in these two crystals are more or less the same. We also measured the lifetimes of non-fixed holograms stored in $LiNbO_3$:Ce crystals with the doping level of 0.02 wt% Ce_2O_3. The experimental results of dark decay for the $LiNbO_3$:Ce crystals have shown the same behaviors as those of samples S1-S5, and the dark decay in all these $LiNbO_3$ crystals is due to proton compensation to the space charge field.

3.4.3 Electron tunneling

In lithium niobate crystals with low doping levels, it is proton concentration that dominates the dark decay. With the doping level increasing, the average distance between dopant sites becomes smaller and smaller. Since the probability of electron tunneling from filled traps to empty traps in lithium niobate crystals is an exponential function of the distance between dopant sites, at some point the doping levels will be so large that the effect of electron tunneling will dominate the dark decay. If we plot the dark decay time constant in these crystals vs. reciprocal temperature, we should get Arrhenius law with an activation energy different from that of proton process.

Figure 3-10 shows the measured dark decay time constants for sample S6, a $LiNbO_3$:Fe crystal doped with 0.25 wt% Fe_2O_3, which is 5 times as large as that of S1 and S2. For comparison, the data of S2, which have been shown in Figure 3-8, are also included in Figure 3-10. As we can see that although the plot of sample S6 is still Arrhenius-like, the activation energy, 0.28 eV, is much smaller than that of samples S1 and S2. Obviously,

there is a mechanism other than proton compensation dominating the dark decay in S6. This mechanism has been identified as electron tunneling between sites of Fe^{2+} and

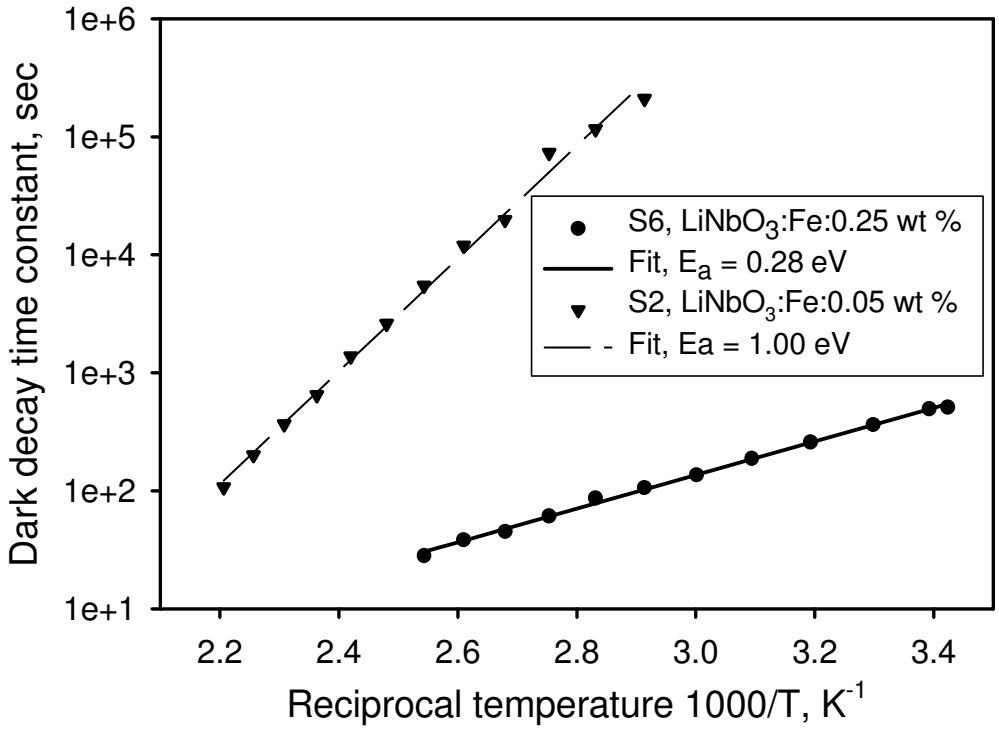

Fig. 3-10. Arrhenius plots of dark decay time constants of holograms in $LiNbO_3$:Fe crystals with a doping level of 0.25 wt% Fe_2O_3, sample S6: proton-reduced. For comparison, the data of S2 are also included.

Fe^{3+}.[3-10][3-14] It is worthwhile to notice that just increasing the doping level by a factor of 5 yields a totally different dark decay mechanism. The reason is that the term $\left(-\frac{4\pi}{h}\sqrt{2m(V-E)}\right)$ is very large in Equation 3-9, even a very small decrease in L will cause dramatic increase of the probability of electron tunneling. This type of dark decay limits the highest practical doping level for $LiNbO_3$:Fe crystals.

One important characteristic of electron tunneling between dopant sites is that the probability of tunneling, thus the dark conductivity due to electron tunneling, depends on effective trap density, N_{eff}, which is defined as in Equation 3-12. For $LiNbO_3$:Fe crystals, c_X is $c_{Fe^{2+}}$, and c_{X^+} is $c_{Fe^{3+}}$. Upon strong thermal reduction (much more Fe^{2+} than Fe^{3+} present), a lack of empty sites diminishes the dark conductivity. The dark conductivity due to electron tunneling is supposed to be roughly proportional to the effective trap density. Figure 3-11shows exactly what we expect. The dark decay time constants of sample S7, a $LiNbO_3$:0.138 wt% Fe_2O_3 crystal, with different oxidation states at room temperature have

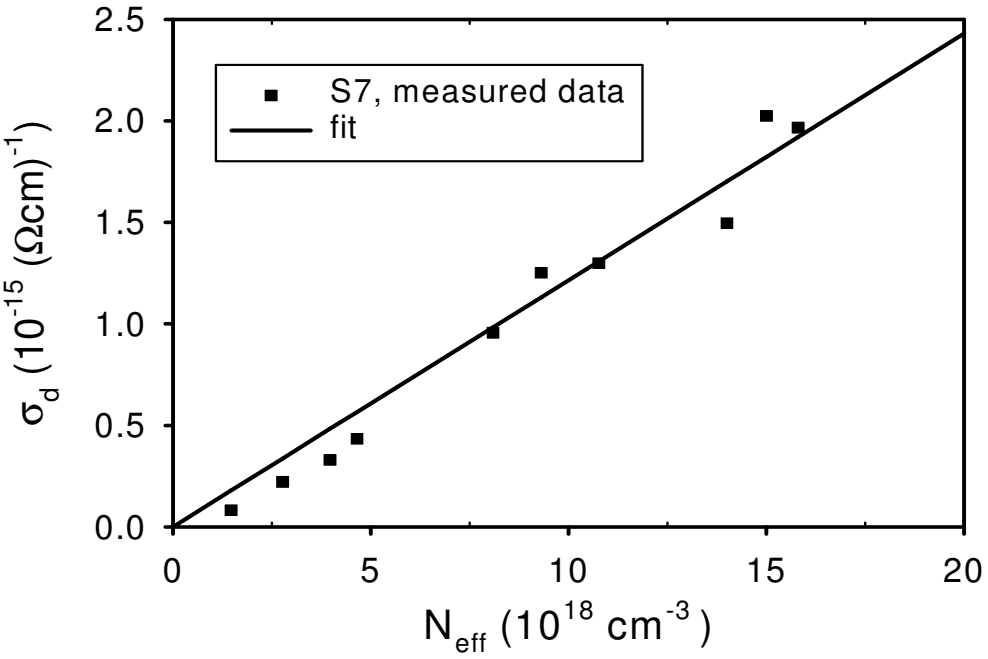

Fig. 3-11. Dark conductivities τ_d vs. effective trap density N_{eff} in sample S7, a $LiNbO_3$:0.138 wt% Fe_2O_3 crystal (Ref. [3-14]).

been measured. The dark conductivities σ_d were calculated as $\sigma_d = \varepsilon_0\varepsilon/\tau_d$ and plotted versus effective trap density N_{eff} in Figure 3-11. The linear relationship between σ_d and N_{eff} is:

$$\sigma_d = \kappa \times N_{eff} + \sigma_{d,0} \tag{3-16}$$

where κ is the slope and $\sigma_{d,0}$ is the interceptor.

Another important characteristic of electron tunneling is that the probability of tunneling is an exponential function of the mean distance between dopant sites. In $LiNbO_3$:Fe crystals, the mean distance between two neighboring Fe sites can be approximately calculated as $(c_{Fe})^{-1/3}$, where c_{Fe} is the entire Fe concentration. Considering the effective trap density, the normalized dark conductivity due to electron tunneling, $(\sigma_d-\sigma_{d,0})/N_{eff}$, which is the slope of linear relationship between σ_d and N_{eff} in Equation 3-16, should be proportional to $\exp[\alpha (c_{Fe})^{-1/3}]$, where α is a constant. That is:

$$(\sigma_d - \sigma_{d,0})/N_{eff} \propto \exp\left(\alpha \times (c_{Fc})^{-\frac{1}{3}}\right) \tag{3-17}$$

Figure 3-12 shows a semi-logarithmic plot of the normalized dark conductivity due to electron tunneling, $(\sigma_d-\sigma_{d,0})/N_{eff}$, versus the third root of the iron concentration, where $\sigma_{d,0}$ is the iron-independent background conductivity, which was obtained from the fitting of Equation 3-16. The experimental data are well described by an exponential growth of the normalized dark conductivity with $(c_{Fe})^{-1/3}$.

Comparing Equation 3-11 and Equation 3-17 we should have:

$$\alpha = \frac{4\pi}{h}\sqrt{2m(V-E)} \tag{3-18}$$

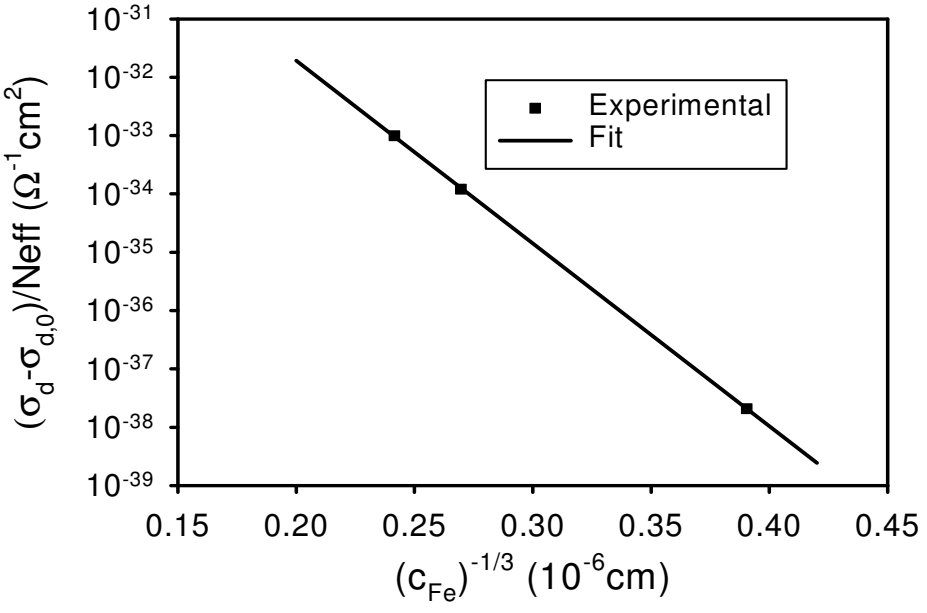

Fig. 3-12. Semi-logarithmic plot of the normalized dark conductivity due to electron tunneling, $(\tau_d - \tau_{d,0})/N_{eff}$, versus the reciprocal of the third root of the iron concentration c_{Fe}.

where h is the Plank's constant, m is the mass of electron, E is the energy of the electron, V is the height of the barrier. From the fitting of Figure 3-12, α is estimated as $7.22 X10^8$/m and V-E is estimated as 0.50 eV. Here we use electron rest mass. Notice that the measured activation energy of electron tunneling is 0.28 eV. The difference of this two energies probably comes from the fact that the effective mass of electron is not equal to the electron rest mass.

3.4.4 Combination of proton compensation and electron tunneling

For $LiNbO_3$ crystals with low doping levels, proton compensation dominates the dark decay, while for those with a doping level as high as 0.25 wt% Fe_2O_3 the dominant mechanism is electron tunneling. It is reasonable to expect both these two effects to be

present in some crystals with doping levels between 0.05 wt% Fe_2O_3 and 0.25 wt% Fe_2O_3. Figure 3-13 shows exactly the picture that we expect. Two crystals, S8 and S9, each with a

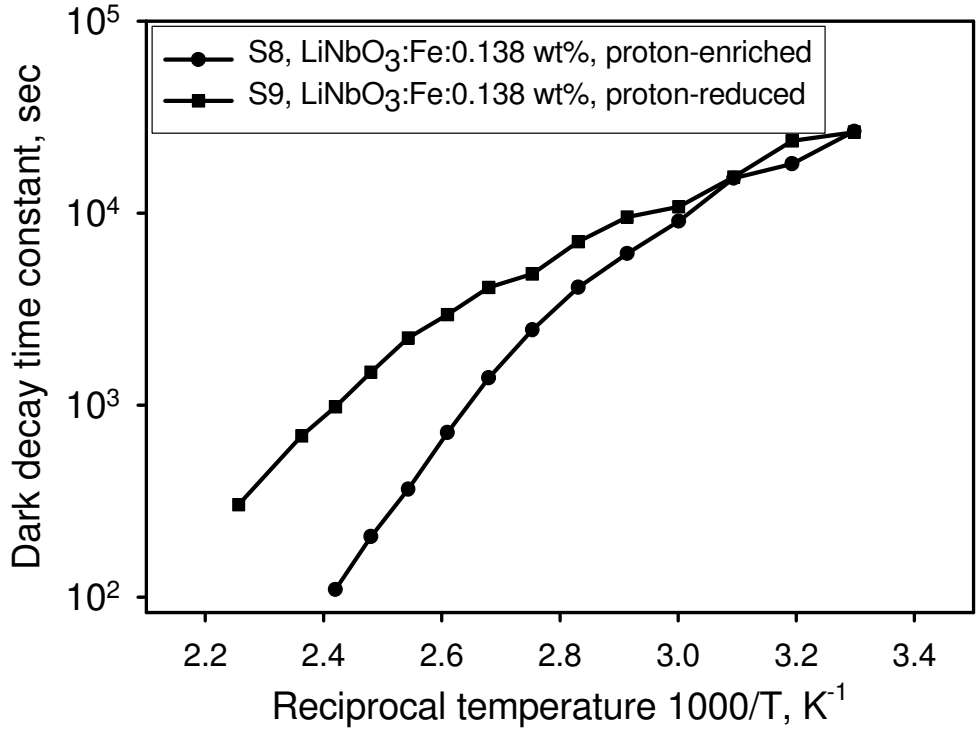

Fig. 3-13. Dark decay time constant versus reciprocal temperature in $LiNbO_3$:Fe crystals with a doping level of 0.138 wt% Fe_2O_3, sample S8: proton-enriched, sample S9: proton-reduced.

doping level of 0.138 wt% Fe_2O_3, have been used. Both of these crystals were cut from the same boule. Sample S8 was proton-enriched and sample S9 was proton-reduced with proton concentrations $5.6X10^{18}$ cm^{-3} and $3.0X10^{17}$ cm^{-3}, respectively. The oxidation states in S8 and S9 are more or less the same.

Since the activation energy of proton compensation is much larger than that of electron tunneling, the dependence of the time constant on the absolute temperature is stronger for proton compensation. At high temperatures, the proton compensation plays a larger role; thus we see the difference between these two crystals in high temperature range due to the different proton contents. At low temperatures, e.g., room temperature, the effect of electron tunneling prevails. Since the crystals have the same doping level and the same oxidation state, we would not see much disparity of the dark decay between the samples S8 and S9 at low temperatures, which is exactly what Figure 3-13 shows. Fitting the data in the low temperature range to an Arrhenius law yields an activation energy close to what we obtained from Figure 3-10, that is 0.28 eV, which means the dominant dark decay mechanism at room temperature in these two crystals is the same as that in crystal S6.

In crystals where both proton compensation and electron tunneling matter, the dark conductivity σ_d should be: $\sigma_d = \sigma_p + \sigma_e$, where σ_p and σ_e are dark conductivities due to proton compensation and electron tunneling, respectively. The decay time constant τ is related to the conductivity σ_d as $\tau = \varepsilon_0\varepsilon/\sigma_d$, so we have:

$$\tau_d = \frac{\tau_p(T) \times \tau_e(T)}{\tau_p(T) + \tau_e(T)} \tag{3-19}$$

where

$$\tau_p(T) = \tau_{0p} \times \exp\left(\frac{E_{ap}}{k_B T}\right) \tag{3-20}$$

and

$$\tau_e(T) = \tau_{0e} \times \exp\left(\frac{E_{ae}}{k_B T}\right) \tag{3-21}$$

We fitted Equation 3-19 to the experimental data obtained with sample S8 using a proton compensation activation energy, E_{ap}, of 0.97 eV and an electron tunneling activation energy, E_{ae}, of 0.28 eV. The result is shown in Figure 3-14, which is, as we can see, very good. We also did the fitting with the data obtained with sample S9. From the fitted pre-exponential factors of the proton compensation we estimate that the ratio of the proton concentrations of samples S8 and S9 is about 22, which agrees very well with the factor of 19 determined by absorption measurements.

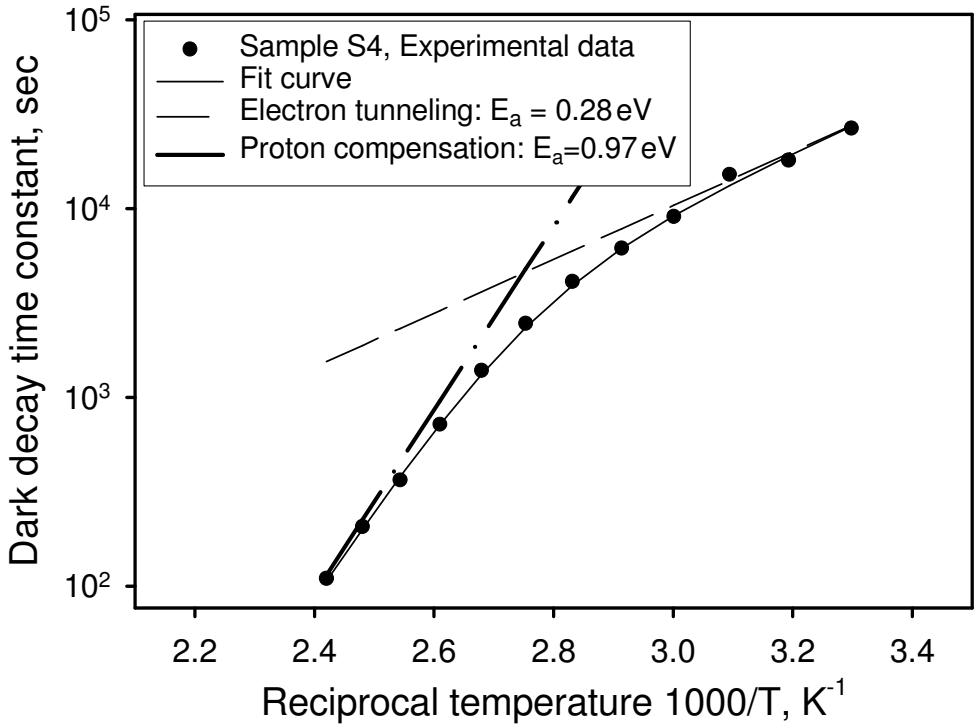

Fig. 3-14. Fig. 7. Dark decay time constant versus reciprocal temperature of sample S8. The solid line is a fit of equation $\tau_d = \tau_p(T)\,\tau_e(T)/(\tau_p(T) + \tau_e(T))$ to the experimental data.

3.5 Conclusions and discussions

In conclusion, two mechanisms of the dark decay, proton compensation and electron tunneling with activation energies of 1.0 eV and 0.28 eV, respectively, have been identified. In crystals with doping levels less than 0.05 wt% Fe_2O_3, proton compensation dominates the dark decay and extrapolation of lifetimes by an Arrhenius law to room temperature is valid. The time constant of this type of dark decay is inversely proportional to the proton concentration. For crystals with doping levels as high as 0.25 wt% Fe_2O_3, elec-

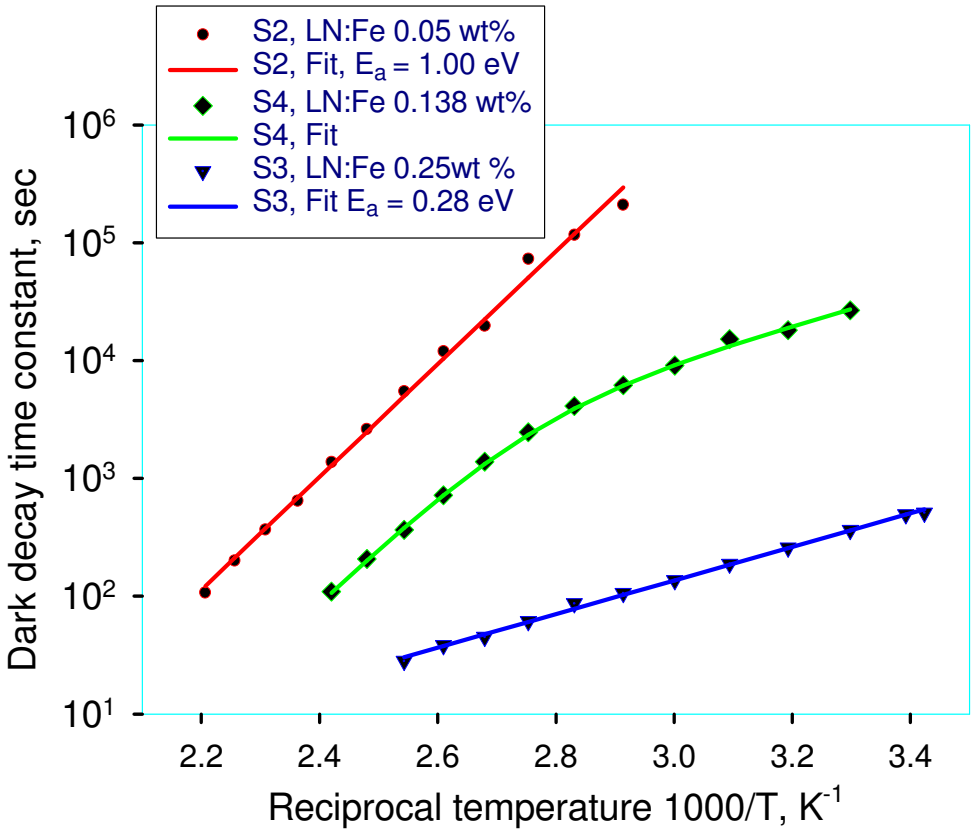

Fig. 3-15. In crystals with low doping levels, proton compensation dominates the dark decay. In crystals with high doping levels, electron tunneling dominates the dark decay. For crystals with medium doping levels, both proton compensation and electron tunneling contribute significantly to the dark decay, and the single Arrhenius law does not hold with a single activation energy.

tron tunneling dominates the dark decay. This type of dark decay also limits the highest practical doping level in $LiNbO_3$ crystals in, e.g., holographic storage systems and optical narrow-band wavelength filters. For crystals with medium doping levels, e.g., between 0.05 wt% Fe_2O_3 and 0.25 wt% Fe_2O_3, both proton compensation and electron tunneling contribute significantly to the dark decay and the single Arrhenius law does not hold anymore with a single activation energy. Caution is required in extrapolating the lifetime of room temperature holograms from the experimental data obtained at high temperatures.

If the dark decay is due to proton compensation, we can always slow the dark decay by reduction of proton concentration. The projected lifetime at room temperature of S2, one proton-reduced crystal, is about 3 years. We expect longer lifetimes if we reduce the proton concentration further. In practice, we always want high doping level to get high sensitivity and dynamic range. But in crystals with high doping levels, the dominant dark decay mechanism is electron tunneling and the lifetimes are very short, for example, about 10 minutes of S3 at room temperature.

In reality, it is good to have crystals with high doping levels and the dark decay still dominated by proton compensation. The question is: how to achieve this? Since electron tunneling is characterized by dopant, we can do this by using other kind of dopant. Actually, Figure 3-16 shows the measured dark decay time constants of two crystals with high doping levels. One is an iron-doped lithium niobate crystal, another is an Mn-doped lithium niobate crystal. Although the doping levels of these two crystals are comparable, the dark decay in the Mn-doped crystal is still dominated by proton compensation, while the dark decay in the iron-doped crystal is still dominated by electron tunneling. Actually, this is the topic of Chapter 4.

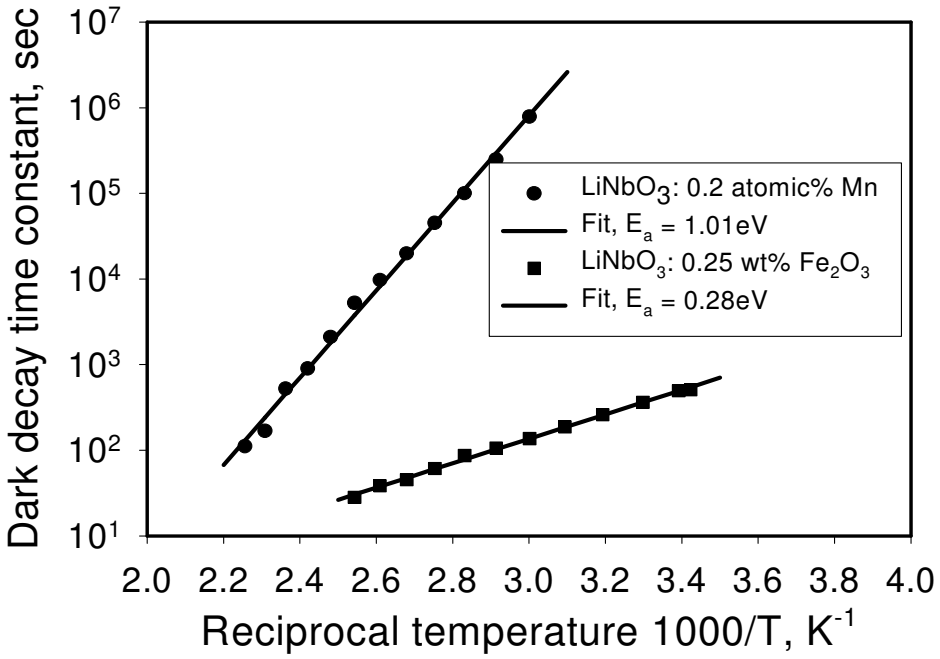

Fig. 3-16. Measured dark decay time constants for two crystals with high doping levels. One is an iron-doped lithium niobate crystal, another is an Mn-doped lithium niobate crystal. Although the doping levels in these two crystals are comparable, the dark decay in the Mn-doped crystal is still dominated by proton compensation, while the dark decay in the iron-doped crystal is dominated by electron tunneling

References

[3-1] D. Psaltis and F. Mok, "Holographic Memories", Sci. Am. **273**, 70-76 (1995).

[3-2] H. J. Coufal, D. Psaltis and G. T. Sincerbox, *Holographic Data Storage*, Springer 2000.

[3-3] V. Leyva, G. A. Rakuljic, and B. O'Conner, "Narrow bandwidth volume holographic optical filter operating at the Kr transition at 1547.82 nm", Appl. Phys. Lett. **65**, 1079-1081 (1994).

[3-4] R. Müller, M. T. Santos, L. Arizmendi, and J. M. Cabrera, "A narrow-band interference filter with photorefractive $LiNbO_3$", J. Phys. **D 27**, 241-246 (1994).

[3-5] S. Breer, H. Vogt, I. Nee, and K. Buse, "Low-crosstalk WDM by Bragg diffraction from thermally fixed reflection holograms in lithium niobate", Electron. Lett. **34**, 2419-2421 (1998).

[3-6] J. J. Amodei and D. L. Staebler, "Holographic pattern fixing in electro-optic crystals", Appl. Phys. Lett. **18**, 540-542 (1971).

[3-7] F. Micheron and G. Bismuth, "Electrical control of fixation and erasure of holographic patterns in ferroelectric materials", Appl. Phys. Lett. **20**, 79-81 (1972).

[3-8] D. von der Linde, A. M. Glass, and K. F. Rodgers, "Multiphoton photorefractive processes for optical storage in $LiNbO_3$", Appl. Phys. Lett. **25**, 155-157 (1974).

[3-9] K. Buse, A. Adibi, and D. Psaltis, "Non-volatile holographic storage in doubly doped lithium niobate crystals", Nature **393**, 665-668 (1998).

[3-10] Y. Yang, I. Nee, K. Buse, and D. Psaltis, "Ionic and electronic dark decay of holograms in $LiNbO_3$: Fe crystals", Appl. Phys. Lett. **78**, 4076-4078 (2001).

[3-11] Y. Yang, K. Buse, and D. Psaltis, "Photorefractive recording in $LiNbO_3$: Mn", Opt. Lett. **27**, 158-160 (2002).

[3-12] E. Krätzig and R. Orlowski, "$LiTaO_3$ as Holographic Storage Material," Appl. Phys. **15**, 133-139 (1978).

[3-13] D. Kip, J. Hukriede, and E. Krätzig, "Holographic Measurement of Dark Conductivity in $LiNbO_3$:Ti:Fe Planar Optical Waveguides," Phys. Status Solidi. **A 168**, R3-R4 (1998).

[3-14] I. Nee, M. Müller, K. Buse, and E. Krätzig, "Role of iron in lithium-niobate crystals for the dark-storage time of holograms," J. Appl. Phys. **88**, 4282-4286 (2000).

[3-15] D. L. Staebler and J. J. Amodei, "Thermally fixed holograms in $LiNbO_3$," Ferroelectrics **3**, 107-113 (1972).

[3-16] B. I. Sturman, M. Carrascosa, F. Agullo-Lopez, and J. Limeres, "Theory of high-temperature photorefractive phenomena in $LiNbO_3$ crystals and applications to experiment," Phys. Rev. B: Condens. Matter **57**, 12792-12805 (1998).

[3-17] S. Kapphan and A.Breitkopf, "PE-Layers and Proton Diffusion Profiles in $LiNbO_3$ Investigated with Fourier-IR and Second Harmonic Generation," Phys. Status Solidi. **A 133**, 159-166 (1992).

[3-18] A. Yariv and S. Orlov, "Holographic storage dynamics in lithium niobate: theory and experiment," J. Opt. Soc. Am. **B 13**, 2513-2523 (1996).

4 Holographic storage using manganese-doped lithium niobate crystals

4.1 Introduction

This chapter describes the experimental investigations of the suitability and superiority of manganese-doped lithium niobate crystals for holographic storage. The idea to use manganese-doped lithium niobate crystals for holographic storage is the direct result of the understanding of dark decay mechanisms discussed in Chapter 3. Several crystals with two different doping levels: 0.2 atomic% Mn and 0.5 wt% $MnCO_3$, are investigated. The organization of this chapter is as follows: First, the motivations of investigating manganese-doped lithium niobate crystals are presented. Then a system that was designed and built for the demonstration of holographic storage is described. The experimental results of dark decay, sensitivity, M/#, multiplexing, thermal fixing, and holographic scattering for lithium niobate crystals doped with 0.2 atomic% Mn and lithium niobate crystals doped with 0.5 wt% $MnCO_3$ are presented. The experimental results show that manganese-doped lithium niobate crystals are well suited for holographic storage.

4.2 Motivations

Photorefractive lithium niobate is a promising material which has found many applications in the fields of optics, optoelectronics and acoustics such as holographic data storage[4-1] and narrow-band wavelength filters for optical telecommunications.[4-2]-

[4-4] Two of the most important properties of photorefractive $LiNbO_3$ crystals are dopant and doping level. Usually, transition metal dopants, such as Fe, Cu, Ce and Mn, are added to the melt as oxides to improve the photorefractive effect. Among all kinds of dopants, Fe has been investigated extensively, while Mn has been less popular and its role in $LiNbO_3$ is not understood completely. It is known that in $LiNbO_3$ crystals the Mn center is deeper than the Fe center and doubly-doped $LiNbO_3$:Fe:Mn crystals have been used to achieve non-volatile holographic storage.[4-5]

For holographic storage system, the most important system metrics are dynamic range, i.e., M/#, and recording sensitivity. Larger M/# and higher sensitivity give the holographic storage system larger storage capacity, better signal to noise ratio (SNR), and fast recording speed, therefore, better overall system performances. In order to get large dynamic range and sensitivity, highly-doped crystals are desirable. Although $LiNbO_3$:Fe crystals have been widely used, one of the drawbacks is the fast dark decay in crystals with doping levels above 0.1 wt% Fe_2O_3. For example, the lifetimes of non-fixed holograms in $LiNbO_3$ doped with 0.25 wt% Fe_2O_3 at room temperature are several minutes, which is generally too short for practical applications.[4-6][4-7] It is desired to have highly-doped crystals with acceptable dark decay.

From Chapter 3, we have already known that, in general, both proton compensation and electron tunneling contribute to the dark decay in $LiNbO_3$ crystals. In crystals with low doping levels, proton compensation dominates the dark decay and the time constant of this type of dark decay is inversely proportional to the proton concentration. For crystals with high doping levels, e.g., 0.25 wt% Fe_2O_3, electron tunneling dominates the dark decay. This type of dark decay also limits the highest practical doping level in $LiNbO_3$ crystals in,

e.g., holographic storage systems and optical narrow-band wavelength filters. For crystals with medium doping levels, e.g., between 0.05 wt% Fe_2O_3 and 0.25 wt% Fe_2O_3, both proton compensation and electron tunneling, contribute significantly to the dark decay, and the single Arrhenius law does not hold anymore with a single activation energy.[4-7] If the dark decay is due to proton compensation, we can always slow the dark decay by reducing the proton concentration. In practice, we always want high doping level to get high sensitivity and dynamic range. But in crystals with high doping levels, the dominant dark decay mechanism is electron tunneling and the lifetimes are very short. It is desirable to have crystals with high doping levels and the dark decay still dominated by proton compensation, that is, to reduce the effect of electron tunneling in highly-doped lithium niobate crystals.

Electron tunneling is characterized by dopant and the probability of electron tunneling through a square potential barrier is:

$$p = \frac{16E(V-E)}{V^2}\exp\left(-\frac{4\pi L}{h}\sqrt{2m(V-E)}\right), \qquad (4\text{-}1)$$

where h is the Plank's constant, m is the mass of the particle, E is the energy of the particle, V is the height of the barrier and L is the width of the barrier, as shown in Figure 3-3. Increasing the doping levels is equivalent to decreasing the average distance between nearby dopant sites, which can be considered as the width of the barrier of electron tunneling. From Equation 4-1, we can see that the probability of electron tunneling is strongly dependent on the height of the barrier, the higher the barrier, the smaller the probability of electron tunneling. By using dopant with deeper energy level in lithium niobate crystals, we can increase the height of the barrier of electron tunneling, therefore, decrease the effect of electron tunneling. Figure 4-1 shows the relative energy level positions of different

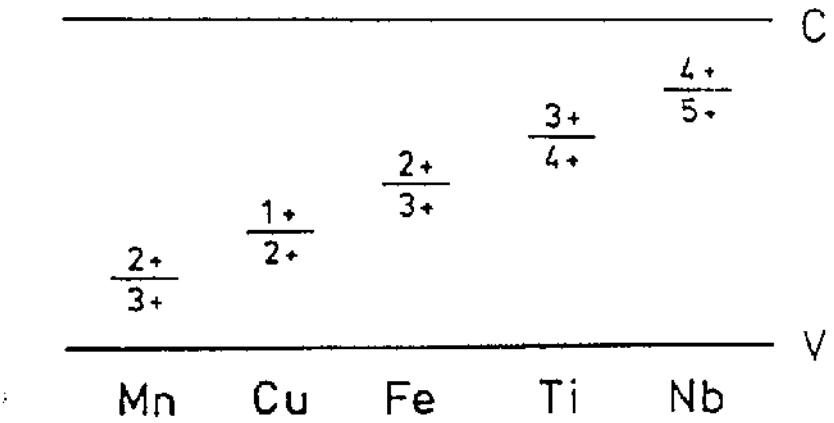

Fig. 4-1. Relative energy level positions in the gap of $LiNbO_3$. For comparison $Nb^{5+/4+}$, which is lying 0.8 eV (this is the polaron binding energy) below the conduction band of the rigid lattice, is included.[4-8]

dopants in the band gap of $LiNbO_3$.[4-8] We can see that the Mn center is deeper than the Fe center, thus the height of the barrier of Mn center should be larger than that of the Fe center. We would expect that the electron tunneling effect in $LiNbO_3$:Mn crystals is smaller. Therefore, it is possible to use manganese-doped lithium niobate crystals with higher doping levels for holographic storage to get larger M/# and sensitivity.

4.3 Experimental setup

The experimental setup for measuring dark decay time constants in manganese-doped lithium niobate crystals was the same as that shown in Figure 3-4 in Chapter 3. The recording light source was an Argon-ion laser operating at 514nm. Extraordinary polarization was used for both recording and readout. The crystals were placed on a heatable plate of a commercial cryostat whose temperature was controlled within 0.1^{o}C accuracy. Recording was always performed at room temperature. Afterwards, the crystals were

heated to a certain temperature in dark and a weak laser beam of 514nm was used to monitor the dark decay of holograms by measuring the holographic diffraction efficiency.

The optical setup for holographic recording is similar to that for measuring the dark decay, except that the cryostat was replaced by a rotation stage. In the experiments that recorded the hologram to the saturation, another red readout beam with the wavelength of 633nm and ordinary polarization was added to monitor the diffraction efficiencies to get a better idea how the strength of the grating evolves.

4.4 Holographic recording in $LiNbO_3$: 0.2 atomic% Mn

After we decided to test manganese-doped lithium niobate crystal, we checked the availability of $LiNbO_3$:Mn in our labs. The available doping levels are 0.015 wt% MnO, 0.05 wt% MnO, 0.2 atomic% Mn, and 0.5 wt% $MnCO_3$. Considering that the highest practical doping level of $LiNbO_3$:Fe is 0.06 wt% Fe_2O_3, we started with $LiNbO_3$: 0.2 atomic% Mn.

We have found that the dark decay time constants of non-fixed holograms in $LiNbO_3$: 0.2 atomic% Mn crystals at room temperature are several orders of magnitude larger than those of $LiNbO_3$:Fe crystals with comparable doping levels. The dominant dark decay mechanism in these crystals is still proton compensation. 100 holograms have been multiplexed in one of these crystals and the M/# and sensitivity for different oxidation states have been measured. The measured sensitivity in these $LiNbO_3$:Mn crystals is 0.5 cm/J (extraordinary light polarization, light wavelength 458nm) and is independent of oxidation states, which is unusual for $LiNbO_3$:Fe crystals, while the largest M/# obtained in $LiNbO_3$: 0.2 atomic% Mn crystals is 12/mm for strong oxidation.

4.4.1 Lifetimes of non-fixed holograms

First of all, we need to check the dark decay in lithium niobate crystals doped with 0.2 atomic% Mn because the doping level is relatively high and we want to make sure that the lifetimes in these crystals are long enough so that the crystals are practically usable.

The dark decay of one of the $LiNbO_3$ crystals doped with 0.2 atomic% Mn, S1, in the temperature range from room temperature to 180 ^oC was measured. For comparison, we also measured the dark decay of a $LiNbO_3$:Fe crystal doped with 0.25 wt% Fe_2O_3, S2. The dimensions of the samples S1 and S2 are 4.5X4.0X1.0 mm^3 and 5.0X3.0X1.0 mm^3, respectively. The c-axes for both S1 and S2 are parallel to the longest directions. Both of the crystals are proton-reduced by being heated at 1000 ^oC in vacuum for several hours. In the measurements of the dark decay, the crystals were placed on a heatable plate inside the cryostat that was temperature-controlled within 0.1° C accuracy. An Argon-ion laser beam with the wavelength of 514 nm was used to record holograms. The laser beam was split into two extraordinarily polarized beams of equal intensity, which were expanded to cover the whole crystal during recording. Recorded holograms had a grating period of 1.3 μm and were written with the grating vector oriented along the c-axis. Recording was performed at room temperature. Afterwards, the crystals were heated to a certain temperature in the dark and a weak laser beam of 514 nm was used to monitor the holographic diffraction efficiency. The weak readout light illuminated the crystal only from time to time, and the intervals between two measurements were long enough to keep the erasure of the holograms by the probing beam negligible. After each experiment the crystal was heated to 230° C and kept at this temperature under uniform illumination for about 45 minutes to erase the gratings completely.

The experimental results of dark decay are shown in Figure 4-2. We can see that the dark decay time constants in both samples, S1 and S2, obey an Arrhenius-type dependence on the absolute temperature T, but with two different activation energies, 1.0 eV and 0.28 eV. The different activation energies explicitly indicate two distinct dominant dark decay

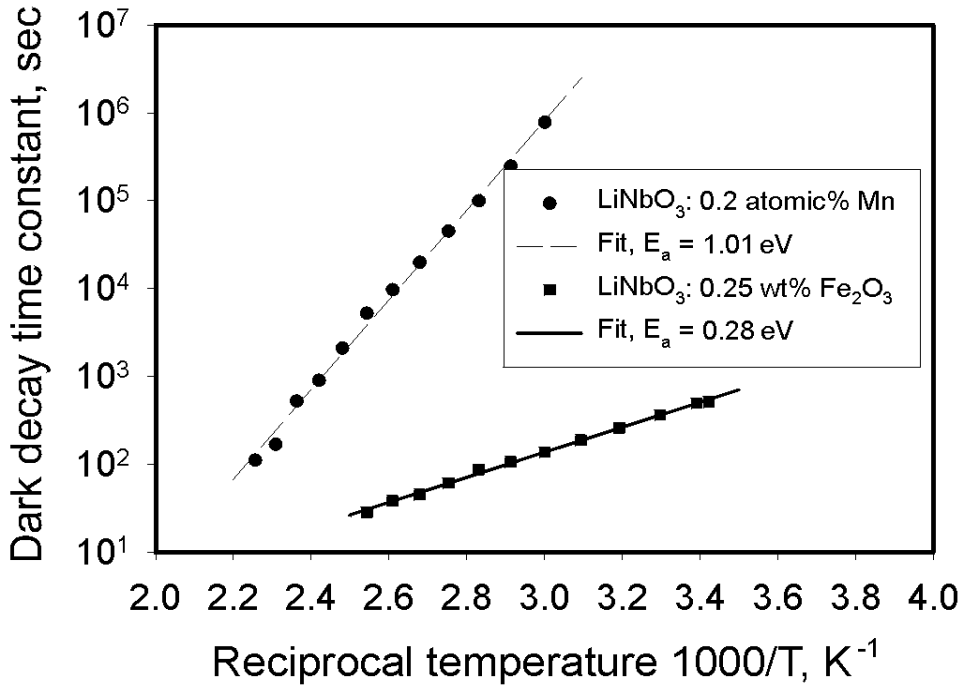

Fig. 4-2. Arrhenius plots of the dark decay time constants of non-fixed holograms stored in sample S1: $LiNbO_3$ doped with 0.2 atomic% Mn, and in sample S2: $LiNbO_3$ doped with 0.25 wt% Fe_2O_3.

mechanisms, which have been identified as proton compensation[4-9]-[4-11] and electron tunneling,[4-6][4-7] respectively. Generally, both of these two mechanisms contribute to the dark decay in $LiNbO_3$ crystals, but for $LiNbO_3$ crystals with low doping levels, electron

tunneling is very weak and the dark decay is dominated by proton compensation. With an increase of the doping levels, the effect of electron tunneling becomes stronger and stronger. In $LiNbO_3$:Fe crystals with doping levels above 0.1 wt% Fe_2O_3, the effect of electron tunneling becomes the dominant dark decay origin and limits the highest practical doping level below 0.1 wt% Fe_2O_3. The probability of electron tunneling through a square potential barrier is proportional to $\exp[-CL(V-E)^{1/2}]$, where L is the width of the barrier, V is the height of the barrier, and E is the energy of the electrons, C is a constant (see Equation 4-1). Since the Mn center is deeper than the Fe center, the height of the barrier between Mn sites should be larger than that between the Fe sites.[4-8] We would expect that the electron tunneling effect in $LiNbO_3$:Mn crystals is smaller. Figure 4-2 shows exactly what we expect. The effect of electron tunneling in sample S1 is negligible and the dark decay is still dominated by proton compensation. The activation energy 1.0 eV is typical for this process.[4-9]-[4-11] Actually, we extrapolated dark decay time constants of non-fixed holograms in sample S1 at room temperature to be about 3 years, while the measured lifetime of non-fixed holograms in sample S2 is just several minutes at room temperature.

It is worthwhile to note here that there are two possible reasons for that the dark decay in S1 is dominated by proton compensation. One is that, as we expected, the real doping level of S2 is 0.2 atomic% Mn and the effect of electron tunneling in $LiNbO_3$:Mn is less than that in $LiNbO_3$:Fe. The second possible reason is that the real doping level of S1 is less than the nominal doping level, i.e., 0.2 atomic% Mn, and the dominant mechanism of proton compensation is just the result of the fact that the real doping level of S1 is low. In order to make sure which one is the real reason, the real doping level of S1 must be determined. Actually, this is one of the topics in Chapter 5. According to the results of

Chapter 5, the distribution coefficient of $LiNbO_3$:Mn, which is defined as the ratio of the real doping level and the nominal doping level, is about 1, which means that the doping level 0.2 atomic% Mn is real.

4.4.2 M/# and sensitivity

The main purpose of investigating the photorefractive properties is to see if we can use $LiNbO_3$:Mn with higher doping levels to obtain larger M/# and sensitivity. The Mn center is deeper than the Fe center. In order to make full use of the gain of doping level in $LiNbO_3$:Mn for boosting M/# and sensitivity, it is reasonable to use laser light with shorter wavelength. In our experiments of measuring M/# and sensitivity, an Argon-ion laser beam with the wavelength of 458 nm was used to record and to erase holograms. The crystal was placed on a rotation stage. The laser beam was split into two extraordinarily polarized beams of equal intensity, which were expanded to cover the whole crystal during recording and erasure. The intensity of each beam was about 10 mW/cm^2, and the grating vector was aligned along the c-axis with a period length of 1.1 mm. During recording, one beam was blocked from time to time to measure the holographic diffraction efficiency. We used Bragg-mismatched erasure, i.e., during erasure the sample was rotated away from the Bragg-matched position and illuminated by the same two beams that were used to record the holograms. In order to avoid building another very strong hologram and fanning, the sample was rotated 0.02 degrees every 10 seconds during erasure. At the end of each period of erasure, the diffraction efficiency was measured by scanning over some range of angle which covered the Bragg-matched position with only the reference beam on and finding the Bragg-matched diffraction efficiency. The typical recording and erasure curves for sample

S1 is shown in Figure 4-3. From single-hologram recording and erasure, we obtain a sen-

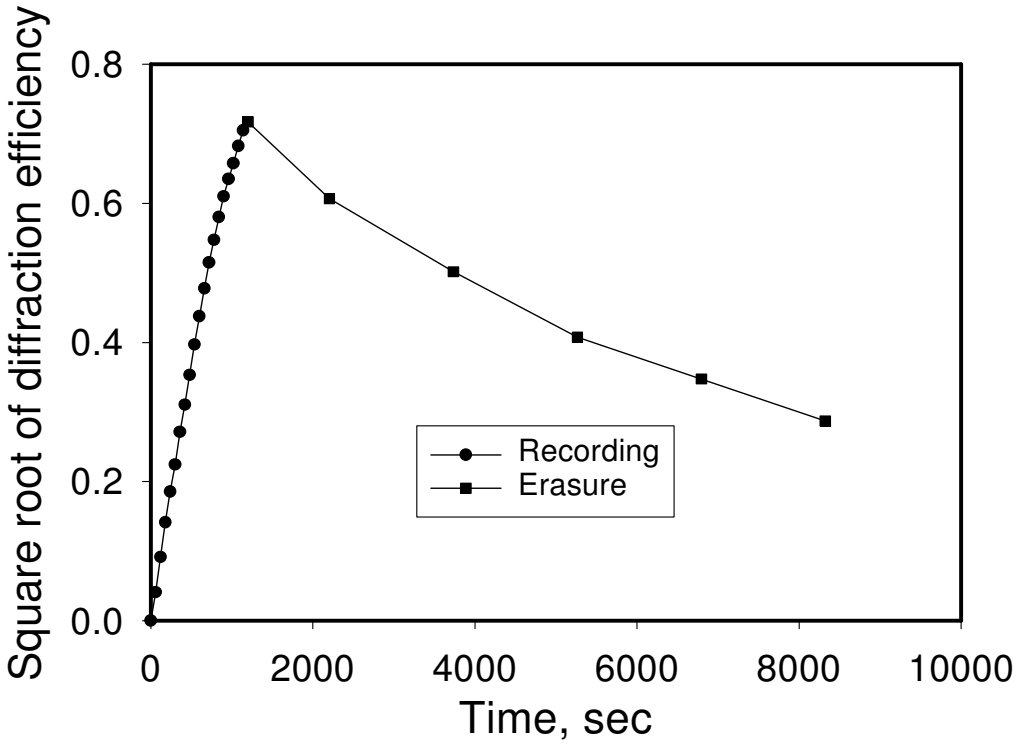

Fig. 4-3. Typical recording and erasure curves for sample S1: $LiNbO_3$ doped with 0.2 atomic% Mn. The wavelength of laser beam for recording is 458nm and extraordinary polarization is used. The recording intensity per beam is about 10 mW/cm^2.

sitivity of about 0.5 cm/J and an M/# of 6.5/mm. Here the sensitivity is defined as

$$S = \left(\frac{d}{dt} \sqrt{\eta} \Big|_{t=0} \right) / (IL), \tag{4-2}$$

and the M/# is defined as

$$M/\# = \left(\frac{d}{dt} \sqrt{\eta} \Big|_{t=0} \right) \times \tau_e, \tag{4-3}$$

where η is the diffraction efficiency calculated as $I_{diffracted}/I_{incident}$, L is the thickness of the crystal, I is the total intensity of the recording beams, and τ_e is the erasure time constant.[4-12] Notice that both, S and M/#, are pretty high compared to the typical values of $LiNbO_3$:Fe.

4.4.3 Multiplexing of 100 holograms

In order to verify that the M/# is real and achievable for practical applications, 100 holograms have been multiplexed in sample S1 (extraordinary light polarization, light wavelength 458 nm). Figure 4-4 shows the comb function of the 100 multiplexed holo-

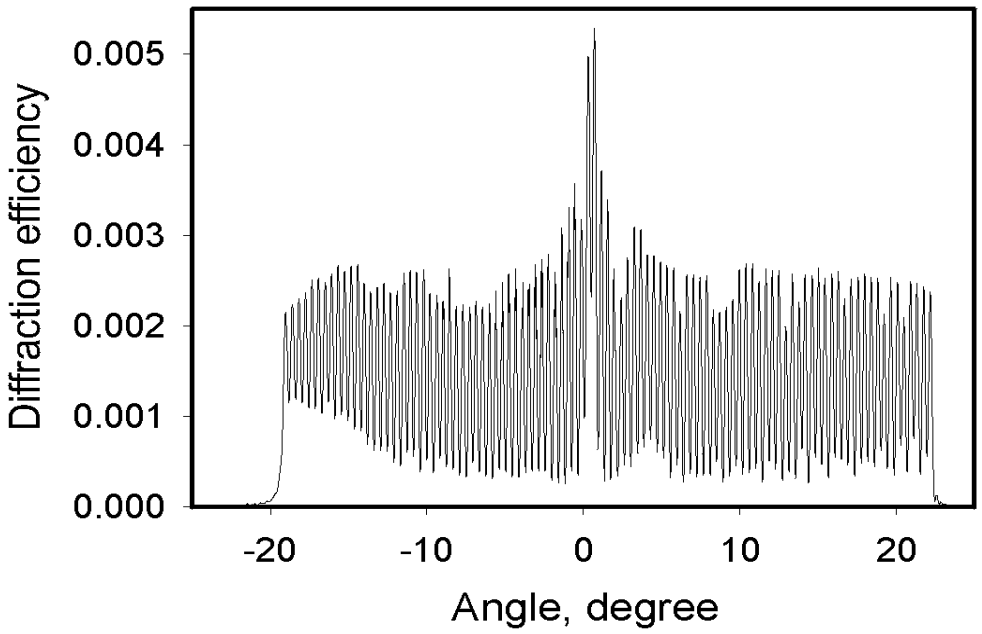

Fig. 4-4. Comb function of multiplexing 100 holograms in sample S1: $LiNbO_3$ doped with 0.2 atomic% Mn. The M/# calculated from this comb function is 5.

grams. We used a pre-calculated exposure schedule to equalize the diffraction efficiency. The selectivity of holograms is about 0.185^{o} and we chose the angle between two neighboring holograms to be 0.4 degrees. The M/# we got from this multiplexing, which was calculated by

$$M/\# = \sum_{n} \sqrt{\eta_n}, \tag{4-4}$$

is 5.0/mm, where η_n is the diffraction efficiency of the nth hologram. The loss of some M/# is due to the non-ideal exposure schedule.[4-12] The larger diffraction efficiencies around the center of the comb function are due to some back reflection. The M/#'s obtained from both -- single-hologram recording and erasure, and multiplexing -- agree very well.

4.4.4 M/# and sensitivity vs. oxidation state

The oxidation state of $LiNbO_3$ crystals can be changed by annealing at elevated temperature in appropriate atmosphere, typically oxygen for oxidation and argon for reduction. It is well known that M/# and sensitivity in $LiNbO_3$:Fe crystals are strong functions of oxidation state. Typically, the more the crystal is reduced, the larger the sensitivity and the smaller the M/#, and vice versa. We also measured M/# and sensitivity in sample S3, a

Table 4-1. Summary of thermal treatments of sample S3.

Oxidation state	Thermal treatment
State 1	Highly-oxidized, starting with state 6, in oxygen at 930°C for 24 hours.
State 2	Starting with state 1, in argon at 780°C for 1 hour.
State 3	Starting with state 2, in argon at 780°C for 3 hours.
State 4	Starting with state 3, in argon at 780°C for 4 hours.
State 5	Starting with state 4, in argon at 780°C for 11 hours.
State 6	Highly-reduced, in vacuum at 1000°C for 14 hours, then in oxygen at 925°C for 4 hours.

$LiNbO_3$ crystal doped with 0.2 atomic% Mn, with different oxidation states. Sample S3 was cut from the same boule as S1 and was also proton-reduced and with the same size as sample S1. Table 1 contains information about the thermal treatment for each oxidation state of S3. The method of quantitatively calibrating the oxidation/reduction state of $LiNbO_3$:Mn is still missing, therefore the ratio $C_{Mn^{2+}}/C_{Mn^{3+}}$ could not be determined for each oxidation state. The measured M/#'s and sensitivities for different oxidation states are shown in Figure 4. Surprisingly, the sensitivity in sample S3 is almost the same, 0.5 cm/J,

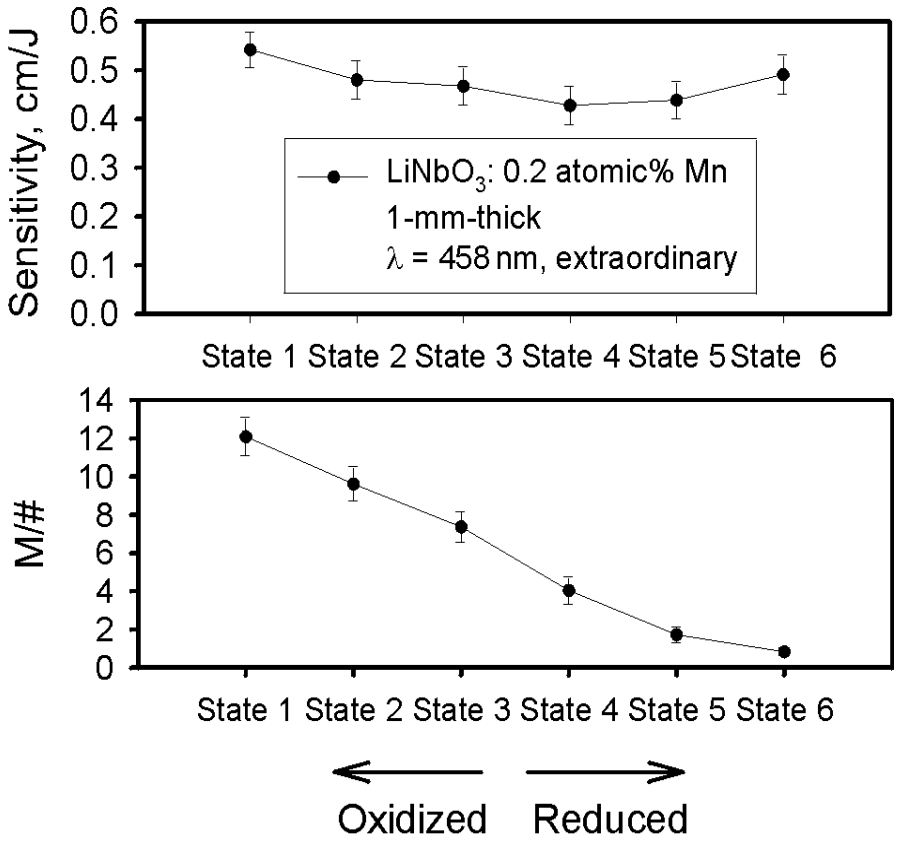

Fig. 4-5. Measured sensitivity and M/# vs. oxidation state in sample S3: $LiNbO_3$ doped with 0.2 atomic% Mn.

and it is almost independent of the oxidation states, while the M/# drops by a factor of 15 from the highly oxidized to the highly reduced state. The highest M/# was obtained for the highly-oxidized state. This independence of sensitivity on the oxidation state in $LiNbO_3$:Mn is in strong contrast to the trade-off between M/# and sensitivity in $LiNbO_3$:Fe and is good for holographic applications.

One possible way to account for the lack of a trade-off between M/# and sensitivity in the $LiNbO_3$:Mn crystal is by assuming that a large majority of the Mn traps are occupied by electrons even in highly oxidized crystals. Therefore the sensitivity, which is proportional to the filled trap density, does not change much when the $LiNbO_3$:Mn crystal is oxidized and a small percentage change in the Mn^{2+} concentration takes place. On the other hand, the percentage change of Mn^{3+} is large, which leads to the increase in M/# as the crystal is oxidized. Since we assume most of the Mn traps are Mn^{2+}, considering the doping level (0.2 atomic% Mn), the sensitivity could be high. Nevertheless, this assumption and the one-center model are not self-consistent. In Chapter 5 an alternative charge transport model will be proposed to explain all the photorefractive phenomenon of $LiNbO_3$:Mn crystals.

4.5 Holographic recording in $LiNbO_3$: 0.5 wt% $MnCO_3$

We have shown that the dark decay in manganese-doped lithium niobate crystals with doping level as high as 0.2 atomic% Mn is still dominated by proton compensation. The measured M/# and sensitivity in $LiNbO_3$: 0.2 atomic% Mn are pretty large compared to those we got from $LiNbO_3$:Fe. Now we would like to know what the limit is, i.e., what is the highest practical doping level in $LiNbO_3$:Mn for the application of holographic stor-

age, and what kind of M/# and sensitivity we can obtain from these crystals. Fortunately, we have several manganese-doped lithium niobate crystals with doping level of 0.5 wt% $MnCO_3$ available in our labs. It turned out that the highest practical doping level in manganese-doped lithium niobate for holographic storage is about 0.5 wt% $MnCO_3$. The largest M/# and sensitivity measured in these crystals are 90/cm and 1.4cm/J with the wavelength of 458nm and extraordinary polarization and the optimal oxidation state for these crystals is highly oxidized. Moreover, some other advantages of manganese-doped lithium niobate crystals for holographic storage, such as excellent recording stability and repeatability, no holographic scattering, have been observed.

4.5.1 Lifetimes of non-fixed holograms

As usual, we first check the dark decay issue. The lifetimes of non-fixed holograms in one of the $LiNbO_3$: 0.5 wt% $MnCO_3$ crystals, S4, were measured. The dimension of sample S4 is 5.5X4.5X0.8 mm^3 with the c-axis along the longest direction, which means S4 is x-cut. The oxidation state of S4 is as grown. The experimental setup and method for measuring the dark decay time constants are the same as described previously. Figure 4-6 shows the measured dark decay time constants of non-fixed holograms in S4 with different temperatures. For the purpose of comparison, the experimental data of dark decay of sample S2 were also included in Figure 4-6. From Figure 4-6 we can see that the dependence of dark decay time constants in S4 on temperature is similar to that of $LiNbO_3$: 0.138 wt% Fe_2O_3, which is shown in Figure 3-13 in Chapter 3. The single Arrhenius law does not hold for S4 in the temperature range we used here. This means that both proton compensation and electron tunneling contribute to the dark decay in S4. Nevertheless, the effect of electron tunneling in S4 is still very small. If we fit the data obtained from S4 to Arrhenius

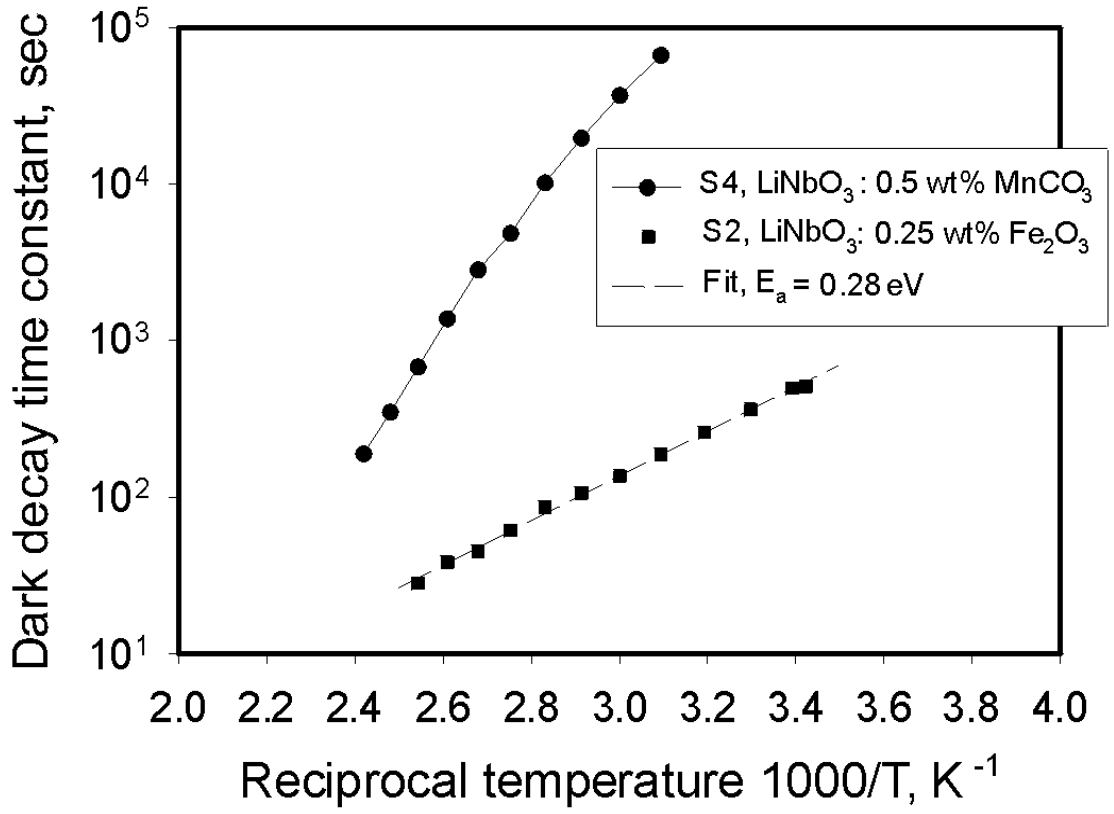

Fig. 4-6. Arrhenius plots of the dark decay time constants of non-fixed holograms stored in sample S4: $LiNbO_3$ doped with 0.5 wt% $MnCO_3$, and in sample S2: $LiNbO_3$ doped with 0.25 wt% Fe_2O_3.

law, we get the quasi activation energy of S4 in the temperature range we used here as 0.75 eV. The quasi activation energy of S4, i.e., 0.75 eV, is smaller than that of proton compensation, which is about 1.0 eV, but still much larger than that of electron tunneling of $LiNbO_3$:Fe, 0.28 eV. Fitting the data of S4 to Equation 3-9 gives us the activation energy of electron tunneling in $LiNbO_3$:Mn to be 0.52 eV and the lifetime of non-fixed holograms in S4 at room temperature as about 17 days. Although this kind of lifetime is not suitable for some applications such as optical add/drop filter for optical telecommunications, it is still acceptable for write/re-write holographic memories.

The experimental results of dark decay in S4 show that the effect of electron tunneling in $LiNbO_3$:Mn is much smaller than that in $LiNbO_3$:Fe. By using Mn instead of Fe, we can increase the highest practical doping level, which is limited by dark decay due to electron tunneling, to 0.5 wt% $MnCO_3$. Although electron tunneling comes into the picture for $LiNbO_3$: 0.5 wt% $MnCO_3$, the effect of electron tunneling is still very small and the lifetime of non-fixed holograms at room temperature in these crystals, which is estimated to be about 17 days, is acceptable for holographic storage systems such as write/re-write memories.

4.5.2 M/# and sensitivity

The doping level of $LiNbO_3$: 0.5 wt% $MnCO_3$ is about 5 times as large as that of S3, of which the doping level is 0.2 atomic% Mn. We would expect to obtain larger M/# and sensitivity with $LiNbO_3$: 0.5 wt% $MnCO_3$. Figure 4-7 shows the typical recording and erasure curves for sample S5: $LiNbO_3$ doped with 0.5 wt% $MnCO_3$. Sample S5 was cut from the same boule of sample S4 with the same dimension: 5.5X4.5X0.8 mm^3. The thermal treatments of S5 were: from the state as grown, at 1000^{o}C in oxygen for 62 hours, then at 720^{o}C in argon for 0.5 hours. The wavelength of laser beam for recording was 458nm and extraordinary polarization was used.The recording intensity was about 6.8 mW/cm^2. From the recording and erasure curve, we calculated a sensitivity and an M/# as 1.4cm/J and 7.3, respectively. Notice that the sensitivity of S5 is much larger than that of S3, while the M/# is comparable to that of S3.

It has been already experimentally shown that for $LiNbO_3$: 0.2 atomic% Mn, the largest M/# can be obtained from the highly-oxidized state, while the sensitivity of different

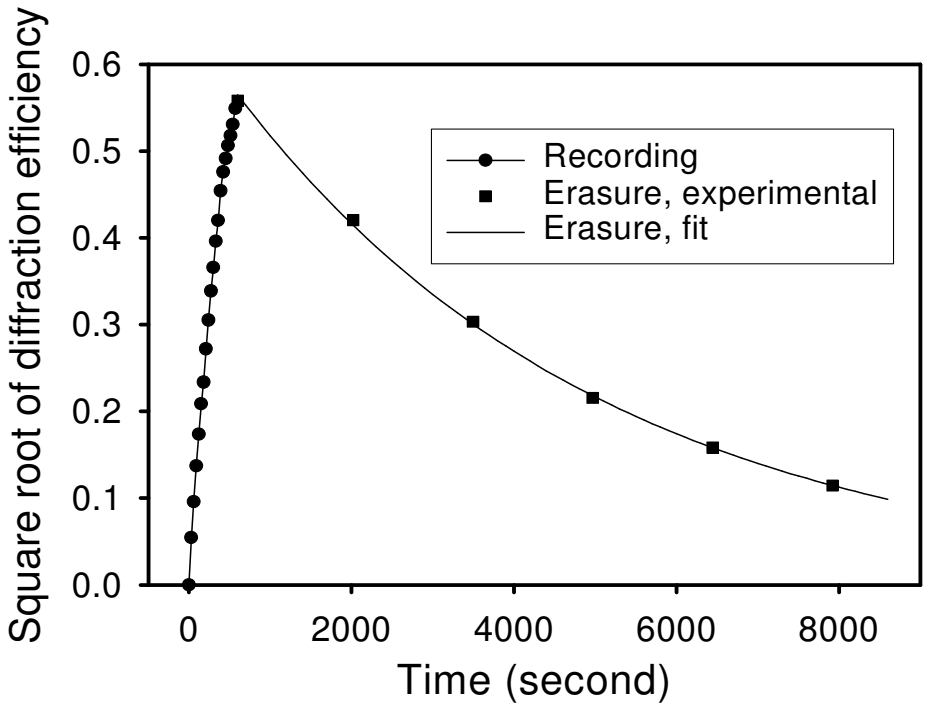

Fig. 4-7. Typical recording and erasure curves for sample S5: $LiNbO_3$ doped with 0.5 wt% $MnCO_3$. The wavelength of laser beam for recording is 458nm and extra-ordinary polarization is used.The recording intensity per beam is about 6.8 mW/cm^2.

oxidation states are almost the same. This means the optimal oxidation state for S3, in terms of M/# and sensitivity, is highly oxidized. We also measured the M/# and sensitivity in another $LiNbO_3$: 0.5 wt% $MnCO_3$, S6, with different oxidation states. Sample S6 was also cut from the same boule of S4 and with the same dimension as S4. Table 4-2 shows the measured M/#'s and sensitivities of S6 with different oxidation states. The M/#'s measured from $LiNbO_3$: 0.5 wt% $MnCO_3$ follow the similar trend on oxidation state as that of $LiNbO_3$: 0.2 atomic% Mn, that is, the more oxidized, the larger the M/# measured, but the change of M/# is not so dramatic. For sample S6, the measured sensitivity is also larger for

more oxidized state, which is different for S3. Nevertheless, in terms of M/# and sensitivity, the optimal oxidation state for both S3 and S6 is highly oxidized.

Table 4-2. Measured M/# and sensitivity of S6: $LiNbO_3$: 0.5 wt% $MnCO_3$ with different oxidation states. Laser beam with the wavelength of 458 nm and extraordinary polarization were used.

Oxidation state/Thermal treatments	M/# (/0.08mm)	Sensitivity (cm/J)
State 1: as-grown	4.5	0.8
State 2: starting from state 1, at 1000°C in oxygen for 16 hours	7.8	1.1
State 3: starting from state 2, at 1000°C in oxygen for 46 hours	7.6	1.4
State 4: starting from state 3, at 720°C in argon for 0.5 hours	7.3	1.3

4.5.3 Multiplexing of 100 holograms

The touchstone for M/# experimentally measured from single-hologram recording and erasure is the diffraction efficiencies of multiplexed holograms. For the multiplexing with M holograms multiplexed, the M/# is calculated by Equation 4-4. By using the appropriate recording schedule,[4-12][4-14] equalized diffraction efficiencies for these *M* holograms can be achieved. Ideally, the equalized diffraction efficiency of each hologram (η) is related to M/# measured from single hologram recording and erasure as[4-12][4-14]

$$\eta = \left(\frac{M/\#}{M}\right)^2. \tag{4-5}$$

Non-ideal recording schedule and some realistic limitations always result in smaller M/# from multiplexing than that from single-hologram recording and erasure.

Before multiplexing, we need to know the selectivity of hologram to determine the space between the neighboring holograms. Figure 4-8 shows the experimentally measured and theoretically calculated selectivity curves for sample S5. The outside angle between the

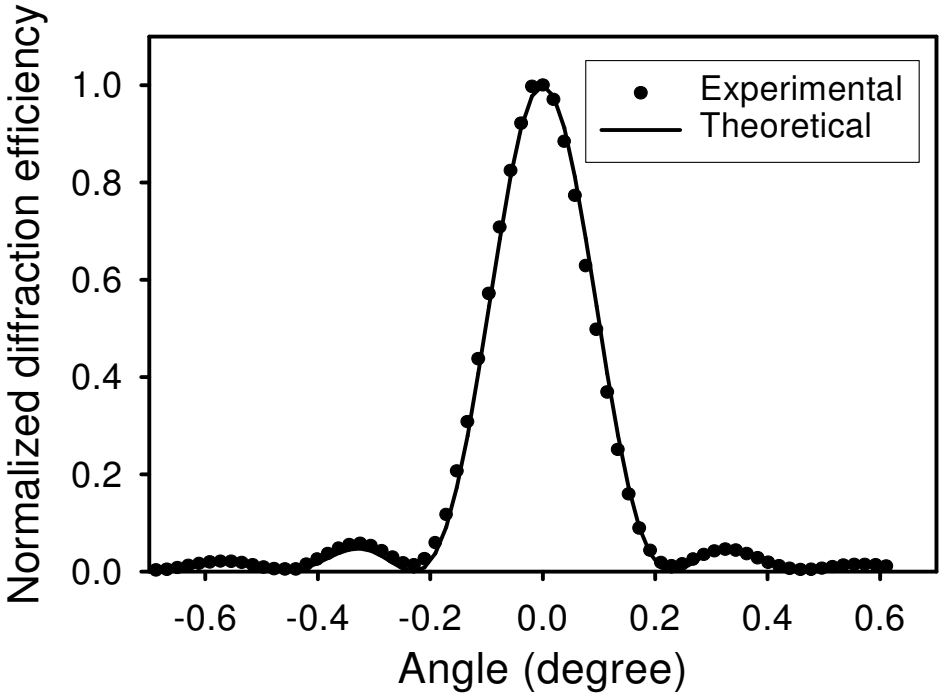

Fig. 4-8. Experimentally measured and theoretically calculated selectivities for sample S5.

two recording beams is 18.7°. From Figure 4-8 we can see that the experimentally measured selectivity curve agrees with the theoretically calculated one very well. The theoretical selectivity, which is calculated by Equation 2-16, is 0.2297°, while the measured selectivity is about 0.23°.

100 holograms have been multiplexed in sample 5. Figure 4-9 shows the comb function of these 100 multiplexed holograms in S5. The angle between neighboring holograms is 0.4°. The M/# calculated from this comb function using Equation 4-4 is 4.7. Note that the M/# measured from single hologram recording and erasure is 7.3.

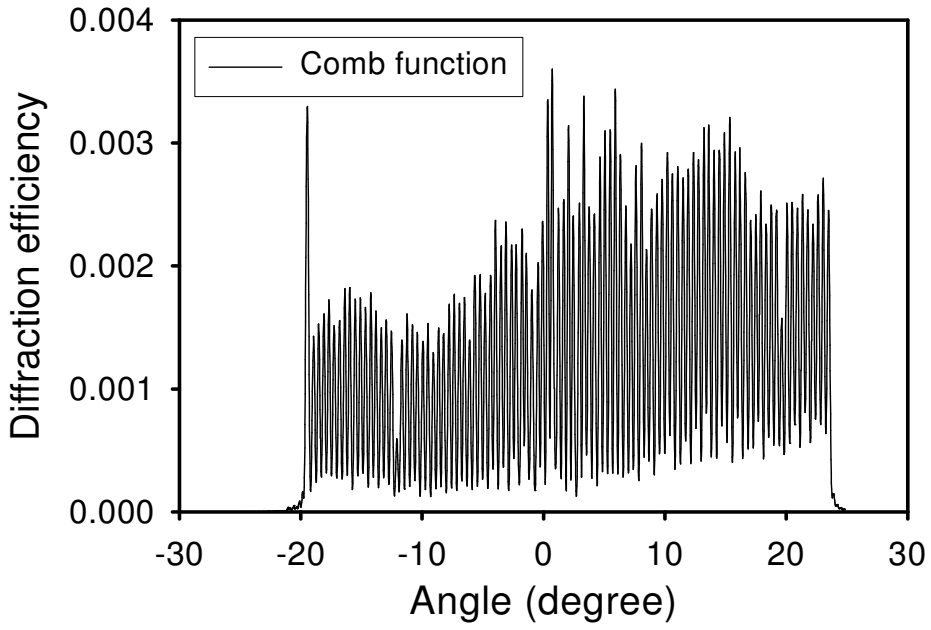

Fig. 4-9. Comb function of multiplexing 100 holograms in sample S5: $LiNbO_3$ doped with 0.5 wt% $MnCO_3$. The M/# calculated from this comb function is 4.7.

4.5.4 Recording over the humps

One of the advantages we found in manganese-doped lithium niobate crystals for holographic storage is the excellent recording repeatability. Figure 4-10 shows the experimental data of two recording curves of S5. We can see that repeatability of this two recordings is very good, considering that the recording durations are relatively long. Especially, the initial parts of these two recording curves are almost overlapped. The disparity between these two recording curves after 15 minutes was probably due to the fluctuation of recording intensities. Another interesting observation from Figure 4-10 is the oscillating behavior of the recording curves: the diffraction efficiency goes up to some maximum value, then drops down to some minimum value, then it goes up and drops down again.

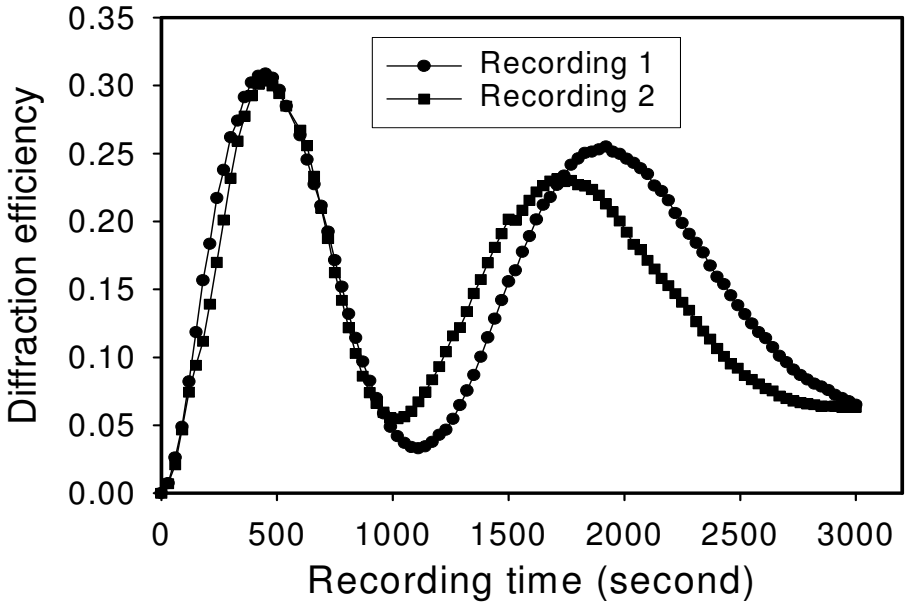

Fig. 4-10. Two recording curves for sample S5. The repeatability is very good, especially for the initial parts of the recording curves. The recording intensity is 11.5 mW/cm^2 per beam.

There are two possible origins of this oscillation of recording curves. One is the complex recording time constant due to the phase shift between intensity pattern and refractive index change pattern. The other is the over-the-hump behavior due to the large refractive index change.[4-13] In order to sort out the real origin behind the oscillating behavior, another red readout beam was added to monitor the evolution of grating strength. Figure 4-11 shows the recording and erasure curves of sample S5. Here we modify the definition of diffraction efficiencies as:

$$\eta' = \frac{I_{diffracted}}{I_{diffracted} + I_{transmitted}}. \qquad (4\text{-}6)$$

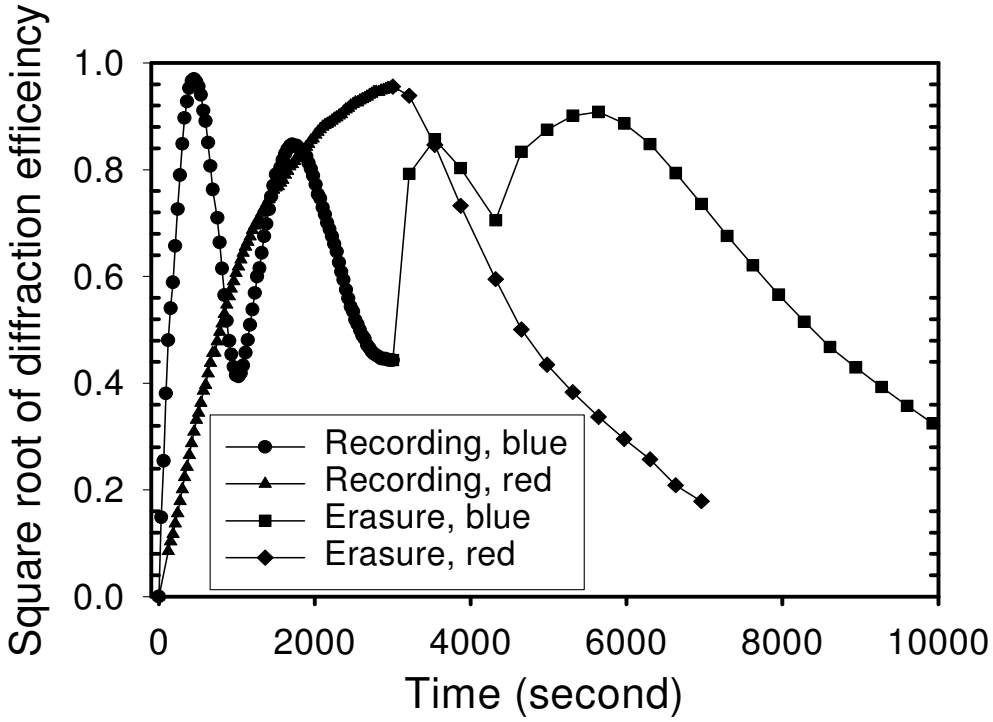

Fig. 4-11. Recording and erasure curves for sample S5. The recording and erasure beams are two plane waves with the wavelength of 458 nm and extraordinary polarization. Another red beam with the wavelength of 633nm and ordinary polarization was added to monitor the evolution of the refractive index change. The recording intensity is 11.5 mW/cm^2 per beam.

The recording and erasure beams were two plane waves with the wavelength of 458 nm and extraordinary polarization. The recording intensity is 11.5 mW/cm^2 per beam. During the recording and erasure, another red readout beam with the wavelength of 633nm and ordinary polarization was added to monitor the evolution of the refractive index change. Figure 4-11 explicitly shows that the oscillating behavior of the recording curves is simply caused by the over-the-hump behavior instead of the complex recording time constant. This is because if the oscillating behavior is due to complex recording time constant, then we should also see the oscillation from the recording curve read out by the red beam. In fact,

the diffraction efficiency just kept growing during the recording even when the diffraction efficiency read out by blue beam decreased. That the diffraction efficiency read out by blue of the first hump is close to 100% also suggests the over-the-hump behavior.

Using the coupled-wave theory, we can obtain the diffraction efficiency in symmetric transmission geometry as:

$$\eta = \exp\left(-\frac{\alpha L}{\cos\theta}\right)\sin^2\left(\frac{\pi L \Delta n}{\lambda \cos\theta}\right), \tag{4-7}$$

where α is the intensity absorption coefficient, L is the thickness of the crystal, θ is the incident angle inside the crystal, λ is the wavelength outside the crystal, and Δn is the amplitude of refractive index change.[4-13] If we use the modified definition of diffraction efficiency η', then we have:

$$\eta' = \sin^2\left(\frac{\pi L \Delta n}{\lambda \cos\theta}\right). \tag{4-8}$$

The recording curve read out by blue beam in Figure 4-11 is over two humps and reaches the second minimum at the end of recording. From the recording curve read out by blue beam, we can estimate the amplitude of the refractive index change for blue beam, Δn_b, at the end of recording as:

$$\Delta n_b = \frac{2\pi \times \cos(4.1°) \times 458 \times 10^{-9}}{0.08 \times 10^{-2} \times \pi} = 1.14 \times 10^{-3}. \tag{4-9}$$

The final modified diffraction efficiency read out by red beam is 0.9556. With this value we can calculate the amplitude of refractive index change for read beam as:

$$\Delta n_r = \frac{\text{asin}(0.9556)\cos(4.1°) \times 633 \times 10^{-9}}{0.08 \times 10^{-2} \times \pi} = 3.12 \times 10^{-4}. \tag{4-10}$$

Notice that the polarization of red beam is ordinary, while the polarization of blue beam is extraordinary. The electrooptic coefficient of $LiNbO_3$ for extraordinary polarization is about 3.22 times as large as that for ordinary polarization.[4-15] The refractive index change is proportional to the electrooptic coefficient. If we multiply Δn_r by 3.22, we get $1.01X10^{-3}$, which is very close to Δn_b.

The time evolution of amplitude of refractive index change, Δn, follows the so-called exponential rise to saturation, that is:

$$\Delta n(t) = \Delta n_0[1 - \exp(-t/\tau_r)] , \tag{4-11}$$

where Δn_0 is the saturation value of Δn, τ_r is the recording time constant. The grating strength A, which is defined as:

$$A = \frac{\pi L \Delta n}{\lambda \cos\theta}, \tag{4-12}$$

can be calculated from the square root of the modified diffraction efficiency and is proportional to Δn. Therefore the grating strength should also follow the so-called exponential rise to saturation:

$$A(t) = A_0[1 - \exp(-t/\tau_r)] . \tag{4-13}$$

Figure 4-12 shows the grating strength in S5, which is calculated from the measured diffraction efficiency read out by red beam, vs. recording time. Fitting the experimentally measured data in Figure 4-12 to Equation 4-13 gives us the saturation value of grating strength for red beam as $A_{0r} = 1.6654$ and the recording time constant as $\tau_r = 2100$ seconds. Fitting the erasure curve in Figure 4-11 to exponential decay gives us the erasure time constant as 2321 seconds. We can see that the erasure time constant is almost equal to recording time constant, which means that there is little asymmetry between recording and erasure.

This again confirms that the oscillating behavior of recording in S5 is due to the over-the-hump behavior instead of complex recording time constant.

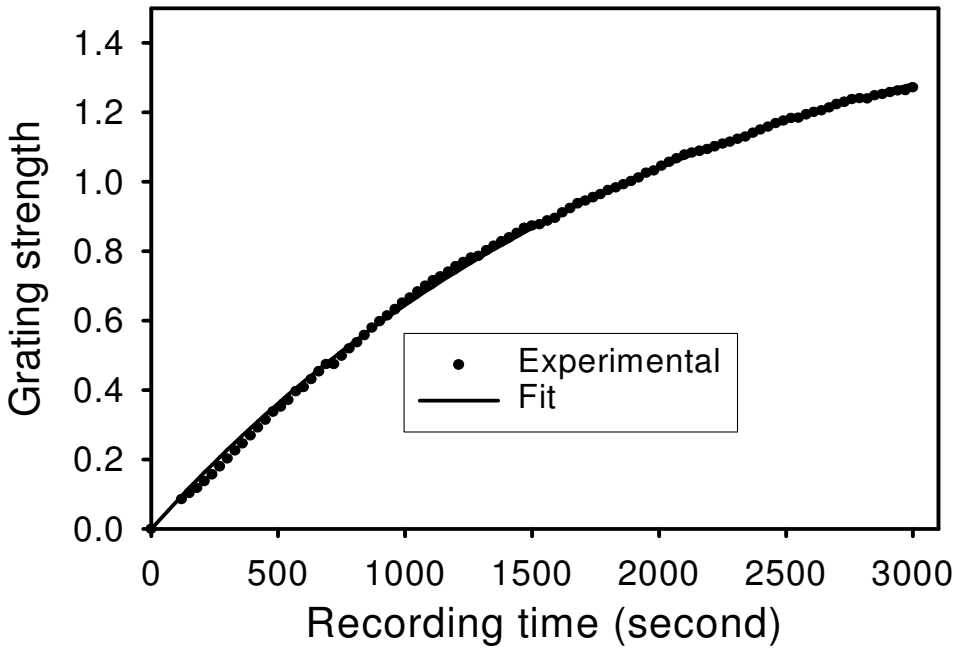

Fig. 4-12. Grating strength vs. recording time in S5 for red readout beam.

4.6 Extraordinary vs. ordinary polarization

One of the advantages of transmission tenantry is that in transmission geometry we can use extraordinary polarization to boost the M/# and sensitivity by a factor of about 3. Anyway, we measured the M/# and sensitivity in S5 with ordinary polarization. Figure 4-13 shows the typical recording and erasure curves in S5 with the wavelength of 458 nm and ordinary polarization. The intensities of reference and signal beams are the same, 6.5 mW/cm^2. From the single hologram recording and erasure, we calculate the M/# and

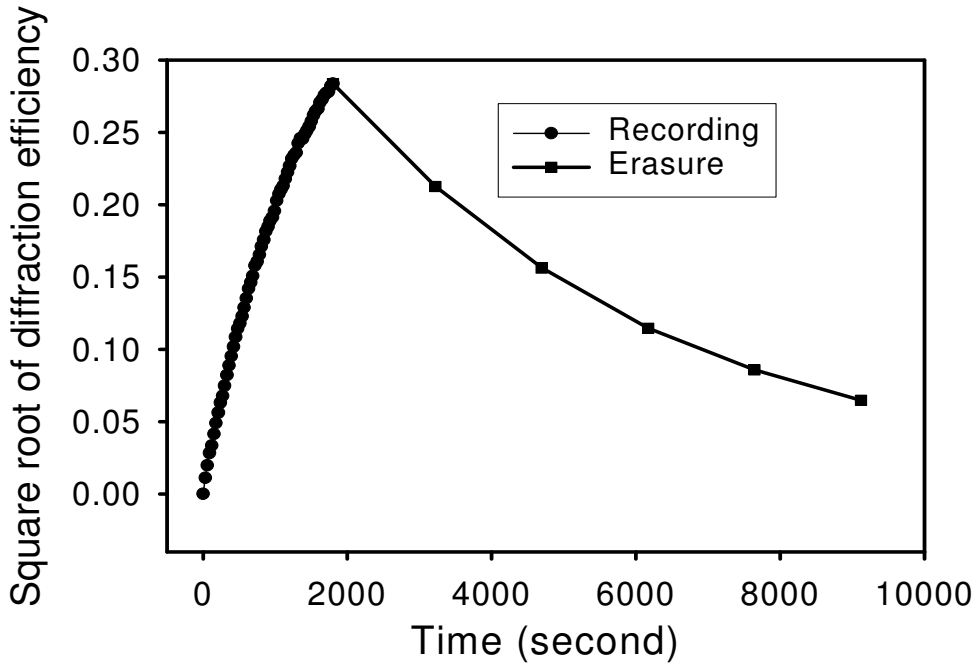

Fig. 4-13. Recording and erasure curves for S5 with the wavelength of 458 nm and ordinary polarization.

sensitivity as 1.6 and 0.28cm/J. Compared to the measured M/# and sensitivity in S5 with extraordinary polarization, which are 7.3 and 1.4cm/J, both the M/# and sensitivity with ordinary polarization drop by a factor of about 5 instead of 3. The extra drop in M/# and sensitivity with ordinary polarization is due to the larger absorption for ordinary polarization light. Figure 4-14 shows transmitted spectrum of S5 for ordinary and extraordinary polarizations. The disparity between the absorption coefficients of ordinary and extraordinary polarizations, which is called dichroism, is very large in S5.

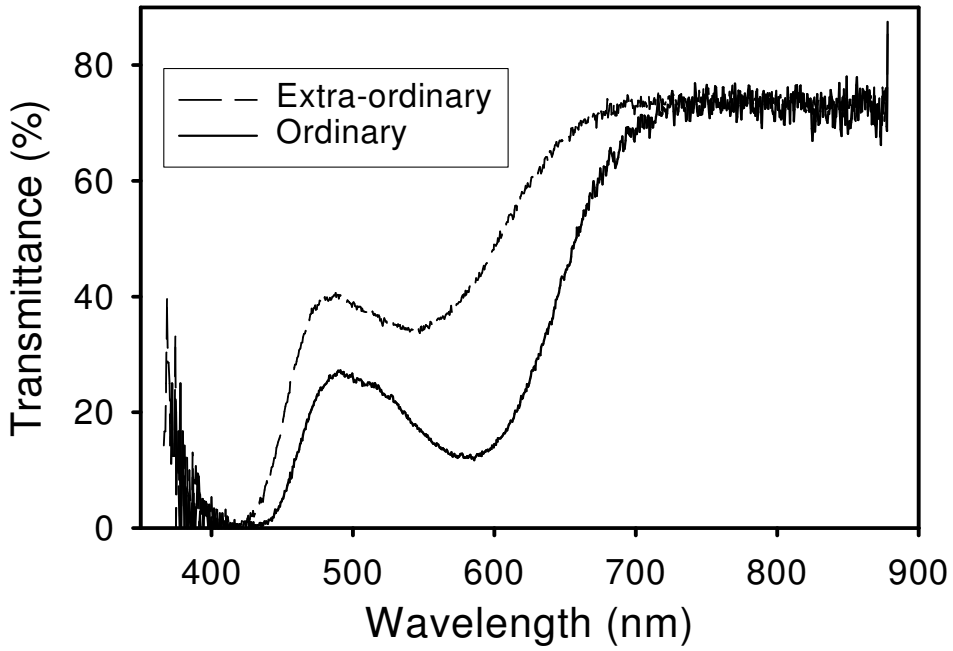

Fig. 4-14. Transmitted spectra of S5 for ordinary polarization and extraordinary polarization.

4.7 Thermal fixing in manganese-doped lithium niobate

Stabler etc. found that holograms can be "thermally fixed" in some electrooptic materials, such as $LiNbO_3$ crystals, by heating the crystals during or after normal recording. The fixed holograms can then be read out non-destructively at room temperature. It is believed that proton plays a key role in thermal fixing. The mobility of proton obeys the so-called Arrhenius law with an activation energy of 1.0-1.2 eV in the temperature range 20-300^{o}C. From room temperature to enhanced temperature, the mobility of proton increases exponentially. At enhanced temperature the electric space charge-field gratings are compensated by protonic gratings because protons become mobile at enhanced temperature.

After cooling the crystal down to room temperature homogeneous illumination is used to develop the fixed protonic gratings by erasing the electric gratings. The mobility of proton at room temperature is very small, which leaves the protonic gratings at room temperature non-destructive to the illumination of readout beam.

Depending on whether the recording is performed at room temperature or enhanced temperature, we can define the strategy of thermal fixing as low-high-low or high-low. For the strategy of low-high-low, the process is as follows:

- Normal recording at room temperature, either single hologram or multiple holograms;
- Heat the crystal to elevated temperature, say 160^{o}C, and keep the crystal at this elevated temperature for some time;
- Quickly cool the crystal down to room temperature, then use homogeneous illumination to develop the stored refractive index pattern.

For the low-high-low, the most important issue is the thermal fixing efficiency, which is defined as the ratio of diffraction efficiency after and before thermal fixing. Up to more than 90% thermal fixing efficiencies have been reported in $LiNbO_3$:Fe.

We also successfully performed the low-high-low thermal fixing in $LiNbO_3$:Mn crystals. Figure 4-15 shows the thermal fixing in one of the manganese-doped lithium niobate crystal with doping level of 0.2 wt% MnO, S7. The horizontal axis is the normalized diffraction efficiency with the diffraction efficiency just after normal recording normalized to 1. The recording was performed at room temperature using two plane waves with the wavelength of 458 nm and extraordinary polarization. After recording, a red beam was used to scan over some angle range which covers the Bragg-matched position to find the maximum diffraction efficiency. Then the crystal was put into an oven with temperature pre-set

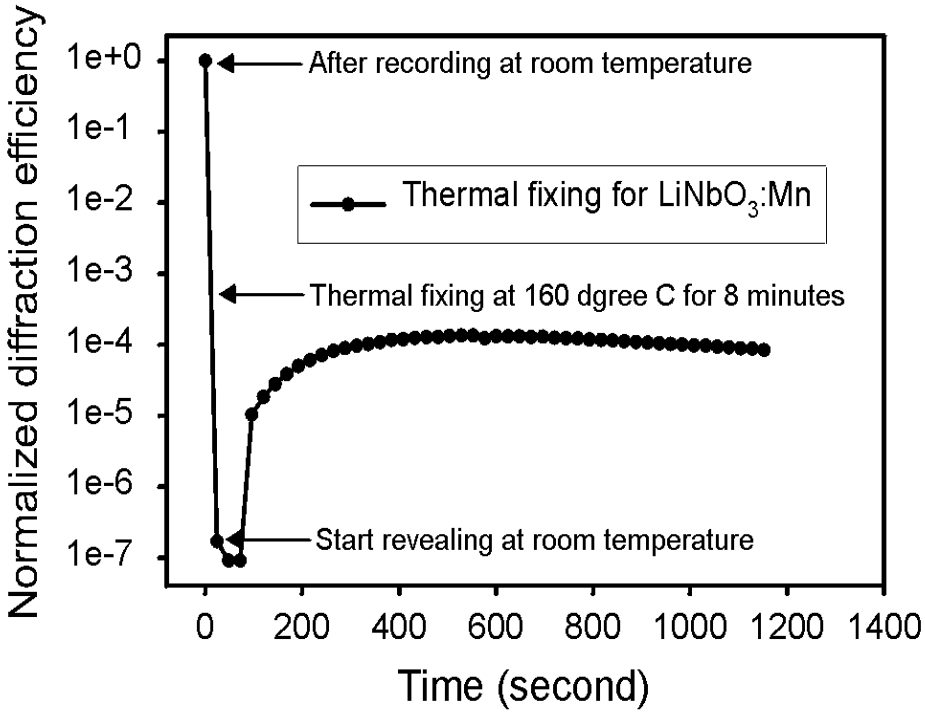

Fig. 4-15. Thermal fixing in S7: $LiNbO_3$: 0.2 wt% MnO. The thermal fixing efficiency is about 0.014%.

to 160^{o}C for 8 minutes. Afterwards, the crystal was taken out of the oven and cooled down to room temperature in the air. The homogeneous illumination of blue light was used to develop the fixed hologram. Simultaneously, a red readout beam was used to scan some angle range to find the Bragg-matched diffraction efficiency.

From Figure 4-15 we can see that at the beginning of revealing the diffraction efficiency is very low. The electric grating was compensated by protonic grating. The reason we see the decrease of the diffraction efficiency at the beginning of the developing is that the compensation was not completed. The electric grating was still stronger than the pro-

tonic grating after thermal fixing. At the beginning, the developing illumination erased the electric grating, causing the diffraction efficiency to decrease. When the electric grating strength was exactly equal to the protonic grating strength, we got minimum diffraction efficiency. Further homogeneous illumination of blue light erased the remaining electric grating and revealed the protonic grating, until some equilibrium was obtained.

Although we showed that we could successfully perform thermal fixing in $LiNbO_3$:Mn crystals, the thermal fixing efficiency was very low, for example, the fixing efficiency in S7 is only 0.014%, and this low thermal fixing efficiency is consistent with $LiNbO_3$:Mn with other doping levels. We got thermal fixing efficiencies of 0.08% and 0.052% from one of $LiNbO_3$: 0.05 wt% MnO and one of $LiNbO_3$:0.1 wt% MnO, respectively. The low thermal fixing efficiency is one drawback of manganese-doped lithium niobate crystals.

4.8 Holographic scattering

Holographic scattering or fanning in lithium niobate can build up during recording or readout as parasitic holograms. In general, fanning is a serious problem for holographic storage systems using photorefractive lithium niobate crystals because it is unpredictable and if allowed to build up for a long time eventually it leads to complete deterioration of the performance. It is well known that this is the reason that many of the large scale demonstrations of holographic memories were done in the 90-degree geometry where fanning is less of a problem.[4-14] In the previous sections we have already shown that we can obtain larger M/# and sensitivity in $LiNbO_3$:Mn by using transmission geometry and extraordinary polarization. It is also known that $LiNbO_3$:Fe crystals with high sensitivity is prone to fanning. Considering the high sensitivity we measured in $LiNbO_3$:Mn crystals,

one may argue that fanning is a serious problem. Nevertheless, experimentally, we observed little holographic scattering of $LiNbO_3$:Mn crystals during the recording and readout.

We performed an experiment to quantitatively assess the fanning behavior of several $LiNbO_3$:Mn and $LiNbO_3$:Fe crystals that had approximately the same thickness. The optical setup is shown in Figure 4-16. One plane wave with extraordinary polarization was

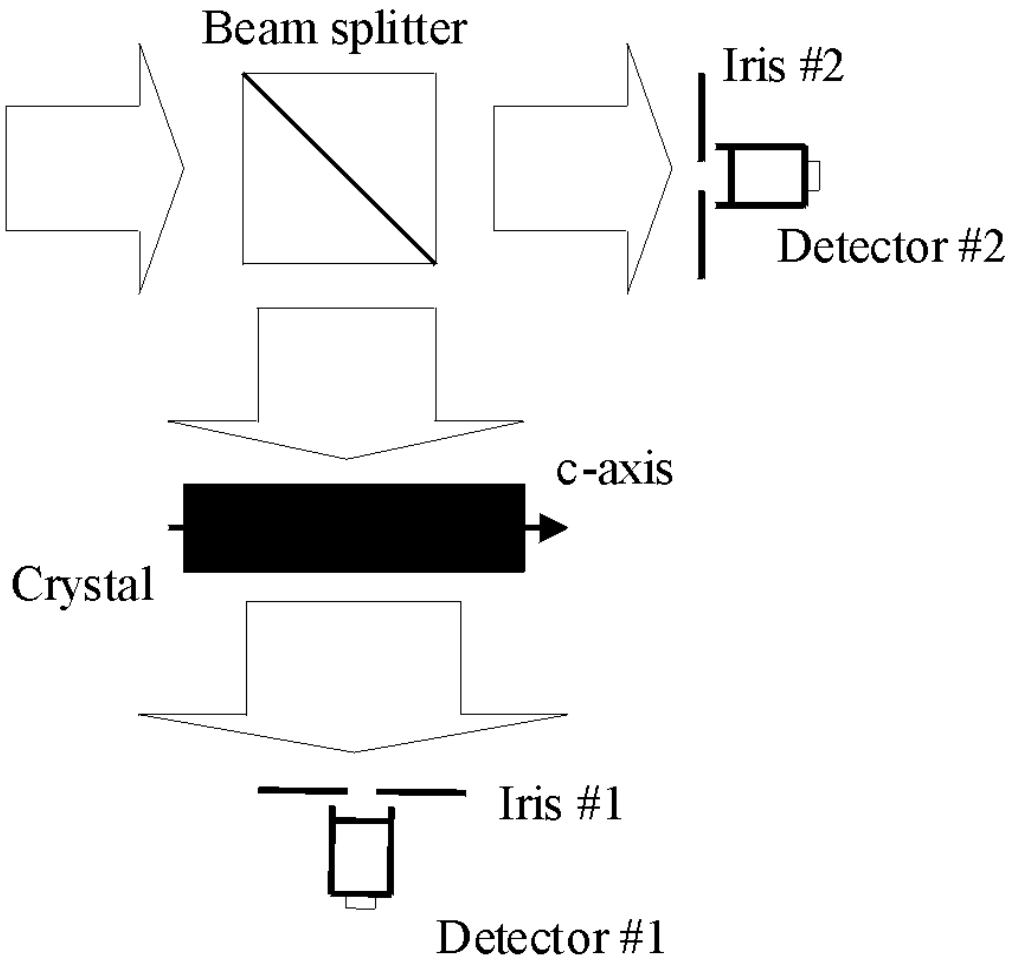

Fig. 4-16. Optical setup for the measurements of fanning in $LiNbO_3$ crystals.

split by a beam splitter into two beams, one of which was directed to the crystal with normal incidence, the other was directed to a detector and as the reference beam. The power of the transmitted beam after the crystal was measured from time to time. We used the laser beams with wavelengths of 458 nm for $LiNbO_3$:Mn and 488 nm for $LiNbO_3$:Fe, and the average intensities in all the cases were the same, 7 mW/cm^2. In Figure 4-17 we plot the normalized

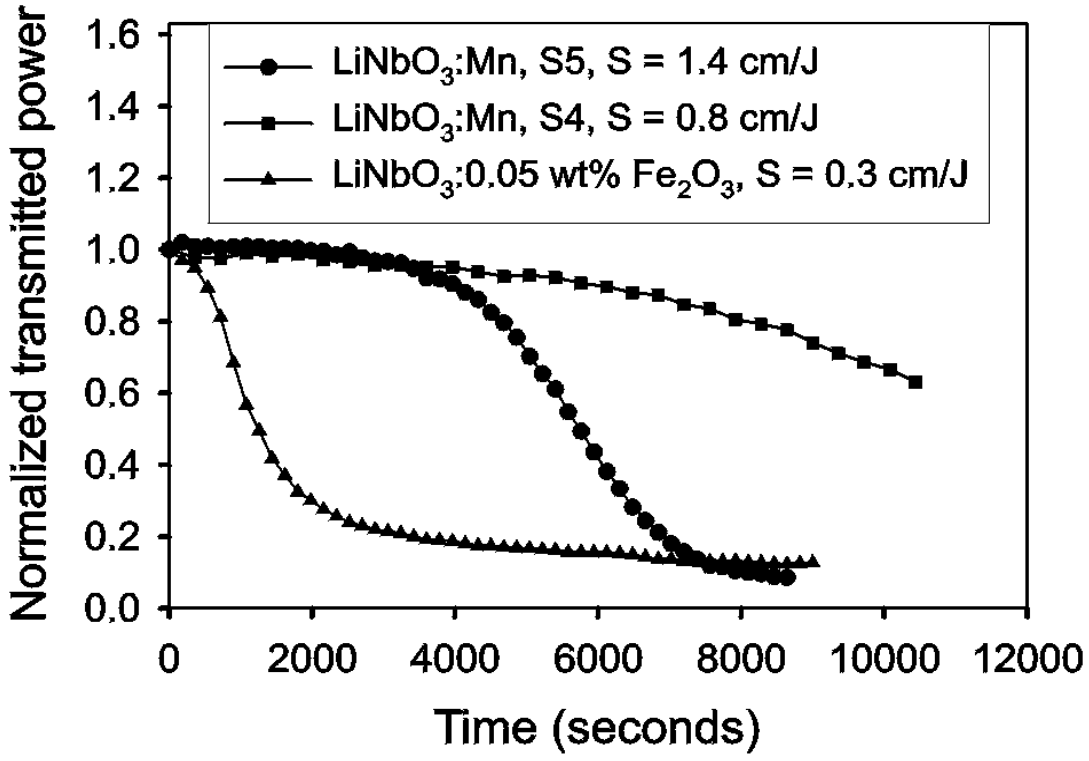

Fig. 4-17. Light power that is transmitted through the crystal during the fanning measurements.

transmitted power as a function of time. Clearly, from the very beginning the holographic scattering in $LiNbO_3$:Fe built up very quickly whereas $LiNbO_3$:Mn crystals remain almost unaffected after one hour. Note that the sensitivities of $LiNbO_3$:Mn crystals we used in this experiment are much higher than those of the $LiNbO_3$:Fe crystal and the buildup speeds of

fanning in $LiNbO_3$:Mn crystals are much slower. In fact, with this intensity 7 mW/cm^2, we can record holograms to almost saturation in S5 within an hour, just before fanning could build up. From these measurements we see that indeed fanning is dramatically reduced in $LiNbO_3$::Mn crystals for recording with blue light.

4.9 Conclusions

In summary, we have shown that manganese-doped lithium niobate crystals are well suited for holographic storage. The electron tunneling effect in $LiNbO_3$:Mn is small because the center of Mn is deep, which allows high practical doping levels. The measured sensitivity of one of the $LiNbO_3$ crystals doped with 0.2 atomic% Mn is 0.5 cm/J and almost independent of the oxidation state, while the largest M/# measured is 12/mm for strong oxidation. The largest M/# and sensitivity obtained from $LiNbO_3$: 0.5 wt% $MnCO_3$ are 90 /cm and 1.4 cm/J, respectively, with the highly oxidized state. Low-high-low thermal fixing has been successfully performed in $LiNbO_3$: Mn crystal although the fixing is low. The repeatability of recording in $LiNbO_3$: Mn is very good and we can easily record the gratings to the saturation. The maximum refractive index change in $LiNbO_3$: 0.5 wt% $MnCO_3$ crystals for extraordinarily polarized laser beam with the wavelength of 458 nm is $1.5X10^{-3}$. The fact that during the recording and erasure there is little holographic scattering may contribute to the excellent recording repeatability. Considering the advantages of $LiNbO_3$: Mn such as large M/# and sensitivity, little holographic scattering, excellent recording repeatability, and working in blue wavelength range, $LiNbO_3$: Mn crystals are well suited for the application of holographic storage.

References

[4-1] H. J. Coufal, D. Psaltis and G. T. Sincerbox, *Holographic Data Storage*, Springer 2000.

[4-2] V. Leyva, G. A. Rakuljic, and B. O'Conner, "Narrow bandwidth volume holographic optical filter operating at the Kr transition at 1547.82 nm", Appl. Phys. Lett. **65**, 1079-1081 (1994).

[4-3] R. Müller, M. T. Santos, L. Arizmendi, and J. M. Cabrera, "A narrow-band interference filter with photorefractive $LiNbO_3$," J. Phys. **D 27**, 241-246 (1994).

[4-4] S. Breer, H. Vogt, I. Nee, and K. Buse, "Low-crosstalk WDM by Bragg diffraction from thermally fixed reflection holograms in lithium niobate," Electron. Lett. **34**, 2419-2421 (1998).

[4-5] K. Buse, A. Adibi, and D. Psaltis, "Non-volatile holographic storage in doubly doped lithium niobate crystals," Nature. **393**, 665-668 (1998).

[4-6] I. Nee, M. Müller, K. Buse, and E. Krätzig, "Role of iron in lithium-niobate crystals for the dark-storage time of holograms," J. Appl. Phys. **88**, 4282-4286 (2000).

[4-7] Y. Yang, I. Nee, K. Buse, and D. Psaltis, "Ionic and Electronic Dark Decay of Holograms in $LiNbO_3$:Fe Crystals," Appl. Phys. Lett., **78**, 4076-4078 (2001).

[4-8] O. Thiemann and O. F. Schirmer, "Energy levels of several 3d impurities and EPR of Ti^{3+} in $LiNbO_3$," SPIE **1018**, 18-22 (1988).

[4-9] D. L. Staebler and J. J. Amodei, "Thermally fixed holograms in $LiNbO_3$," Ferroelectrics **3**, 107-113 (1972).

[4-10] A. Yariv and S. Orlov, "Holographic storage dynamics in lithium niobate: theory and experiment," J. Opt. Soc. Am. **B 13**, 2513-2523 (1996).

[4-11] I. B. Barkan, A. V. Vorob'ev, and S. I. Marennikov, "Transient optical storage in lithium niobate crystal," Sov. J. Quantum Electron. **9**, 492-494 (1979).

[4-12] F. Mok, G. Burr, and D. Psaltis, "System metric for holographic memory systems," Opt. Lett. **21**, 896-898 (1996).

[4-13] H. Kogelnik, "Coupled wave theory for thick hologram gratings," Bell Sys. Tech. J. **48**, 2909-2945 (1969).

[4-14] G. Burr, *Volume holographic storage using the 90-degree geometry*, Ph.D. thesis, California Institute of Technology, 1997.

[4-15] R. S. Weis and T. K. Gaylord, "Lithium niobate: summary of physical properties and crystal structure," Appl. Phys. **A 37**, 191-203 (1985).

5 Charge transport model for manganese-doped lithium niobate crystals

5.1 Introduction

One of the reasons that holographic storage systems still remain in the phase of experimental R&D is that there has been a lack of suited materials as the recording medium. The ideal photorefractive recording material should have properties such as high sensitivity, large dynamic range, low holographic scattering, and working in the blue spectral region. In Chapter 4 we have experimentally demonstrated that manganese-doped lithium niobate crystals are highly suited for holographic storage. The electron tunneling effect in $LiNbO_3$:Mn is small because the center of Mn is deep, which allows high practical doping levels.[5-1][5-2] For $LiNbO_3$:Mn, the highest practical doping level is about 0.5 wt% $MnCO_3$ and M/# as large as 90/cm and sensitivity as high as 1.4 cm/J have been obtained using laser beam with extraordinary polarization and wavelength of 458 nm. In terms of both, dynamic range (or refractive index change) and sensitivity, the optimal oxidation state is highly oxidized. Another advantage of manganese-doped lithium niobate crystals is that there is little fanning even in transmission geometry using extraordinary polarization, which makes the recording of multiple holograms more predictable and the exposure schedule easier. Also, as we showed in Chapter 4, the optimal wavelength for the applica-

tion of holographic storage using $LiNbO_3$:Mn crystals is 458nm, which is in blue range and gives higher possible storage capacity.[5-3][5-4]

In order to tailor $LiNbO_3$:Mn crystals for applications such as holographic storage and optical add/drop filters for optical telecommunications, a full quantitative description of the photorefractive properties using appropriate photorefractive charge transport model is needed. While the role of Fe in $LiNbO_3$ crystals has been investigated extensively, Mn has been less popular and only a few literatures have addressed the photorefractive properties of $LiNbO_3$:Mn.[5-5]-[5-10] The one-center model[5-11] has been successful in predicting the photorefractive phenomenon in $LiNbO_3$:Fe and $LiNbO_3$:Cu crystals at continuous wave (cw) intensities.[5-12]-[5-15] Another charge transport model possible for $LiNbO_3$:Mn is the three-valence model.[5-14]-[5-19] In this chapter, the photorefractive properties of lithium niobate crystals doped with manganese (Mn) have been investigated. Material parameters, such as the distribution coefficient, are determined. Absorption measurements are used to obtain some information about several charge transport parameters. The dynamic range (M/#) and sensitivity for crystals of different doping levels, different oxidation states, and for different light polarizations have been measured.

5.2 Samples and experimental methods

The photorefractive properties of several Mn-doped $LiNbO_3$ crystals with different doping levels are investigated. Table 5-1 shows some material parameters of these samples. The dimensions of the samples are defined as $a \times b \times c$, where c is the length along the c-axis and b is the thickness. Thermal treatments were used to change the oxidation state of

some of the samples. The temperature, duration, and atmosphere of thermal treatment are controlled to obtain the desired oxidation state.

Table 5-1. Summary of parameters of Mn-doped lithium niobate samples.

Sample	Doping level	C_{Mn}($\times 10^{24} m^{-3}$)	Dimension (mm^3)	Oxidation state
S1	0.20 wt% MnO	78	$15.0 \times 2.0 \times 20.0$	As grown
S2	0.05 wt% MnO	20	$15.0 \times 2.0 \times 20.0$	As grown
S3	0.50 wt% MnO	196	$15.0 \times 2.0 \times 20.0$	As grown
S4	0.50 wt% $MnCO_3$	122	$4.0 \times 0.84 \times 5.0$	Highly oxidized
S5	0.50 wt% $MnCO_3$	122	$4.0 \times 0.84 \times 5.0$	Highly reduced

Two key parameters of photorefractive lithium niobate crystals are dopant and doping level. Knowing the actual doping level in the crystal is the starting point for all investigation of photorefractive properties. Usually, certain amount of transition metal dopants, such as Fe, Cu, Ce and Mn, are added to the melt as oxides during the growth of crystals. The nominal doping level is measured in weight percentage to the mixture of Li_2O and Nb_2O_5 or in mole percentage to $LiNbO_3$. In some cases, the actual doping level inside lithium niobate crystals is different from the nominal doping level. The ratio between the actual doping level and nominal doping level is called “distribution coefficient”. In order to measure the distribution coefficient of manganese-doped lithium niobate, several samples with different nominal doping levels, 0.05, 0.1, 0.2, 0.5, and 1.0 wt% MnO, have been investigated. Two different methods were applied for all the crystals by independent parties. One method is Neutron Activation Analysis (NAA),[5-20] the other is Inductively Coupled Plasma Optical Emission Spectroscopy (ICP-OES).[5-21] The method of NAA yields a distribution coefficient of 1.1, while the method of ICP-OES yields a distribution coefficient of about 0.85. The average distribution coefficient obtained from these two

methods is about 1. Considering all the possible uncertainties, it is reasonable to take the distribution coefficient of manganese-doped lithium niobate crystals as 1.

In our experiments of measuring M/# and sensitivity, an argon-ion laser beam with the wavelength 458 nm was used to record and to erase holograms. The crystal was placed on a rotation stage. The laser beam was split into two equal-intensity beams. The grating vector was always aligned along the c-axis. During recording, one beam was blocked from time to time to measure the holographic diffraction efficiency as the ratio of diffracted and incident light intensities. We used Bragg-mismatched erasure, i.e., during erasure the sample was rotated far away from the Bragg-matched position (by at least 50 times of the selectivity) and illuminated by the same two beams that were used to record holograms. This guaranteed that the spurious gratings recorded during erasure would have little effect on the measurement of M/# and sensitivity. Moreover, in order to avoid building strong spurious holograms and fanning as well as the non-uniform erasure due to the interference pattern inside the samples, the sample was rotated 0.02 degree every 10 seconds during erasure. At the end of each period of erasure, the diffraction efficiency was measured by scanning over an adequate range of angle (which covered the Bragg-matched position) and finding the maximum diffraction efficiency with only the reference beam on. M/# and sensitivity were calculated according to

$$M/\# = \left(\frac{d}{dt}\sqrt{\eta}\Big|_{t=0}\right)\times \tau_e , \tag{5-1}$$

$$S = \left(\frac{d}{dt}\sqrt{\eta}\Big|_{t=0}\right)/(IL) . \tag{5-2}$$

As an alternative, recording and erasure of the holographic gratings with the blue light (wavelength 458 nm) was monitored with an additional ordinarily polarized red beam (wavelength 633 nm). The red light yields a smaller diffraction efficiency because of the ordinary polarization and the longer wavelength. However, we calibrated this difference based on experimental data and were in the following able to deduce M/# and recording sensitivity for blue light from the readout with red light. Several experiments were performed with both methods (reading with blue/red light) and the obtained M/# and sensitivity values were always in perfect agreement.

5.3 Experimental results

In this section the obtained absorption data, dynamic ranges and sensitivity data, and holographic scattering data are presented.

5.3.1 Absorption measurements

Absorption measurement is a very important method to characterize the material parameters of photorefractive lithium niobate crystals. Usually, the characteristic absorption band and absorption coefficient are used to calibrate the concentration of the corresponding absorption center. The absorption spectra of $LiNbO_3$:Mn crystals in the wavelength range of 0.3-3μm were obtained using a Varian Cary-500 Spectrometer. Figure 5-1 shows a typical absorption spectrum of one $LiNbO_3$:Mn crystal, S1, for ordinary light polarization. The nominal doping level of sample S1 is 0.2 wt% MnO, that is, the Mn concentration is $78 \times 10^{24} m^{-3}$, and the thickness of the crystal is 2mm with the oxidation state as grown. There are three apparent absorption bands in the wavelength range of 0.3-3μm. One is around 2.87μm, which is the characteristic absorption band of OH^-.[5-22]

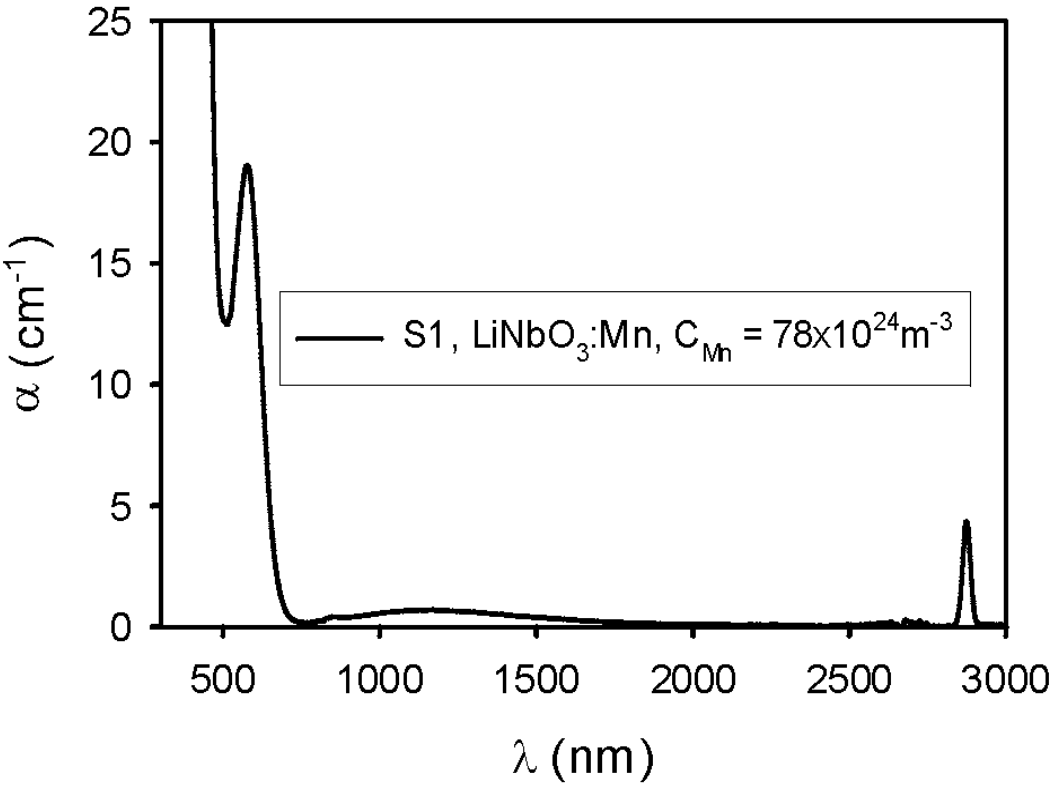

Fig. 5-1. Absorption coefficient α vs. light wavelength λ for an as grown $LiNbO_3$:Mn crystal for ordinary light polarization.

This absorption band is independent of dopant and doping level and can be used to calculate the concentration of protons in $LiNbO_3$ crystals. Another apparent absorption band is the wide band centered around 1.2μm. Presumably, this is due to small polarons.[5-23] The third apparent absorption band is around 577nm, and some researchers attributed this absorption to a crystal field transition of Mn^{3+} or Mn^{4+}.[5-6] Figure 5-2 shows the absorption spectra of three $LiNbO_3$:Mn crystals with different doping levels, S1-S3, for ordinary polarization in the wavelength range of 400nm to 1500nm. The oxidation states of all the three crystals are as grown. From Figure 5-2 we can see that the absorption band around 577nm of $LiNbO_3$:Mn is related to the doping level, the higher the doping level, the larger the absorption coefficient at 577nm. Another observation from Figure 5-2 is that the

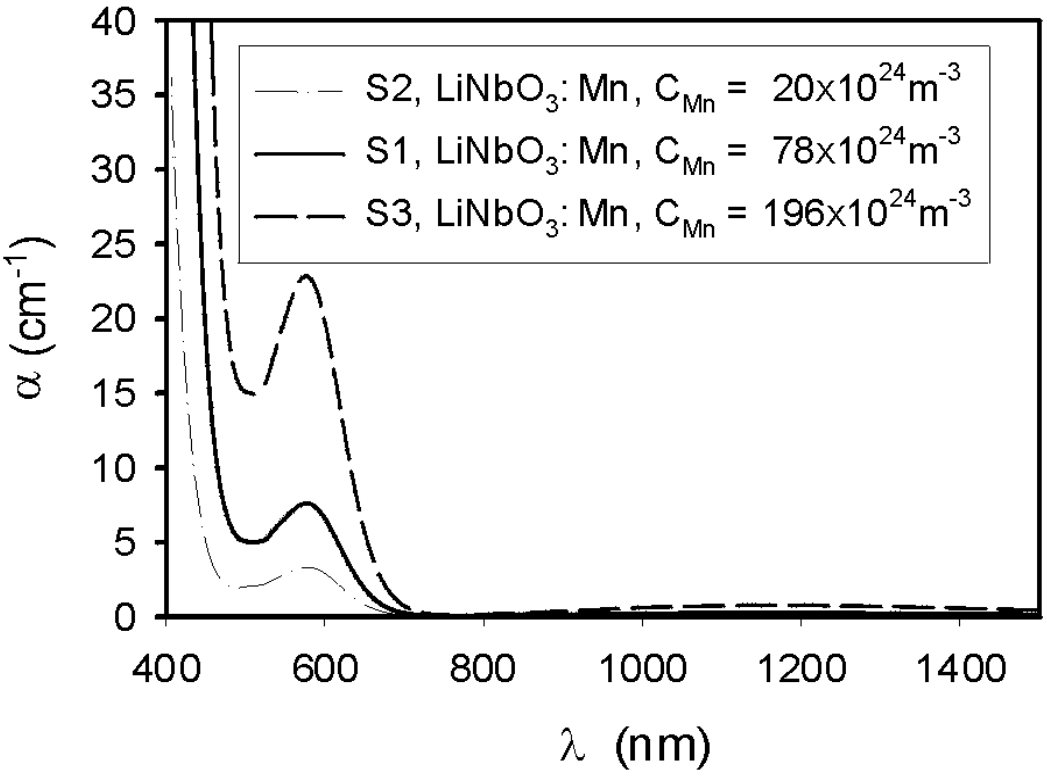

Fig. 5-2. Absorption coefficient α vs. light wavelength λ for three as grown $LiNbO_3$:Mn crystals with different doping levels for ordinary light polarization.

absorption edge, which is typically determined by the energy needed for band-to-band absorption, shifts from shorter wavelength to longer wavelengths with the doping level increasing. One possible explanation of this phenomenon is that there is another broad absorption band of Mn dopants in the range of wavelengths 300 nm to 500 nm, and the shifting of the edge is the result of the combination of the band-to-band absorption and this broad absorption band. Anyhow the absorption spectrum of $LiNbO_3$:Mn crystals for wavelengths below 450 nm does not give much information about the photorefractive parameters of $LiNbO_3$:Mn.

The absorption band around 577 nm is very interesting. First, unlike the absorption band around 477 nm in $LiNbO_3$:Fe, which is due to the transition of electrons from Fe^{2+} to

the conduction band and that can be used to calibrate the concentration of Fe^{2+}, this absorption band around 577 nm in $LiNbO_3$:Mn is not due to the transition of electrons from Mn^{2+} to the conduction band, because the more oxidized the $LiNbO_3$:Mn crystal is, the higher the absorption peak of this band becomes. Figure 5-3 shows the spectra of two $LiNbO_3$

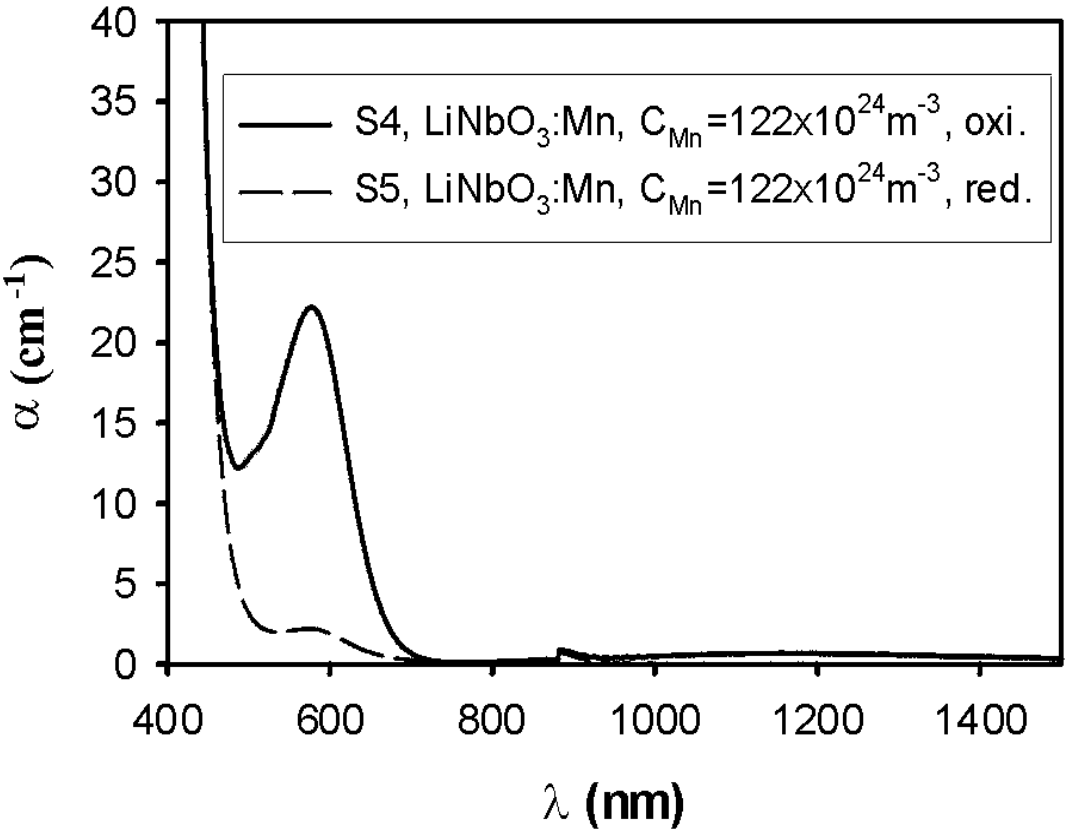

Fig. 5-3. Absorption coefficient a vs. light wavelength l for two $LiNbO_3$ crystals doped with 0.5 wt% $MnCO_3$ for ordinary light polarization. One was oxidized and the other one was reduced.

crystals doped with 0.5 wt% $MnCO_3$, S4 and S5, which were cut from the same boule. S4 was highly oxidized and S5 was highly reduced. We can see that the wavelengths of the absorption peaks of these two crystals are the same, around 577 nm, with the absorption peak coefficient of the highly oxidized crystal much larger than that of the highly reduced.

We can use the absorption coefficient of this band to quantify the oxidation state. Furthermore, this absorption band is not photorefractive, that is, the absorption at 577 nm will not help the photorefractive process. It is generally assumed that Mn traps exist in $LiNbO_3$ as Mn^{2+} and Mn^{3+}, or even as Mn^{4+}. Since the more oxidized, the more absorptive around 577 nm, this absorption band around 577 nm should be related to the concentrations of Mn^{3+} or Mn^{4+}.

Another interesting phenomenon about the absorption spectrum of $LiNbO_3$:Mn is the large dichroism. The dichroism is defined as the difference between the absorption coefficients for ordinary and for extraordinary light polarizations. Figure 5-4 shows the

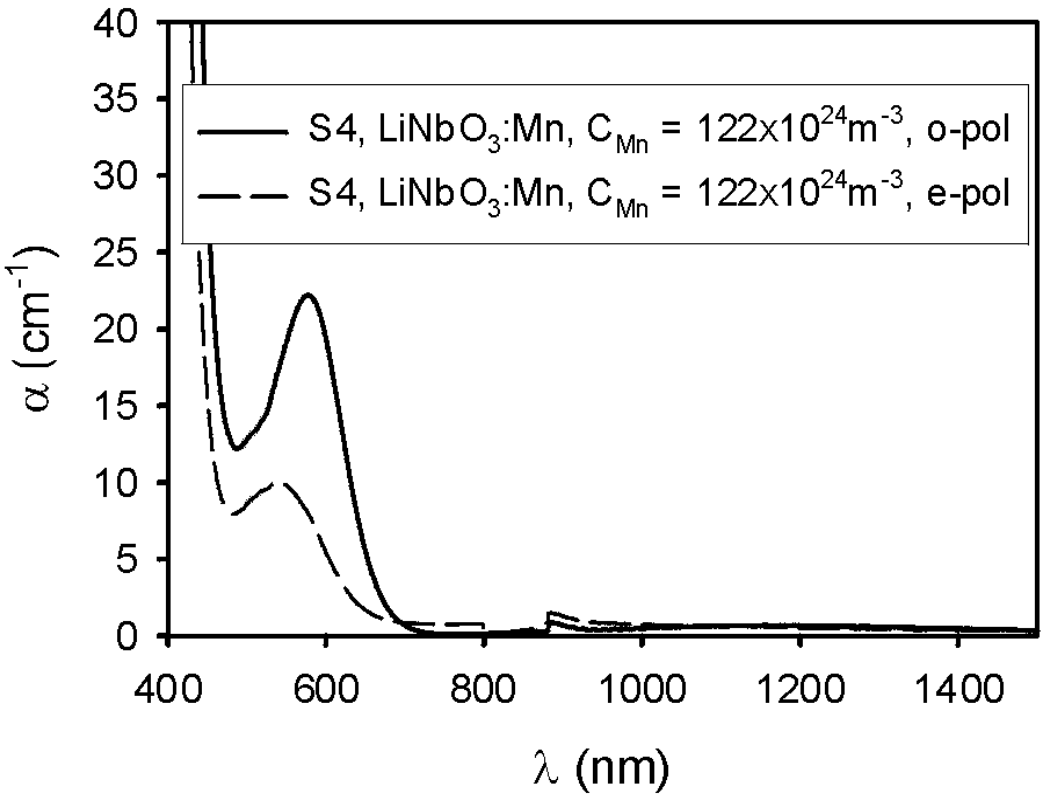

Fig. 5-4. Absorption coefficient α vs. light wavelength λ for a $LiNbO_3$:Mn crystal for ordinary and extraordinary light polarizations.

measured absorption spectra of one $LiNbO_3$:Mn crystal, S4, for ordinary and extraordinary light polarizations. From Figure 5-4 we can see that in the visible range the absorption coefficient for ordinary polarization is larger than that for extraordinary polarization. Around the absorption edge, this dichroism is equivalent to a shift of the edge. Since the absorption edge is very steep, the dichroism around the absorption edge is very large even though the shift due to the dichroism is small. The dichroism of the absorption band around 577 nm is consistent with attribution to a crystal field transition. The absorption peak of this band for extraordinary light shifts to shorter wavelength. Later we will show that the fact that the absorption of extraordinary polarization is less than that of ordinary polarization makes the optimal polarization for $LiNbO_3$:Mn crystal to be extraordinary.

5.3.2 Dynamic range and sensitivity

Dynamic range and sensitivity are two of the most important system metrics for holographic storage systems, which are relevant for almost all the system parameters. One of the key considerations for holographic storage systems is the selection of the recording wavelength. Typically, the optimal recording wavelength is the center wavelength of the absorption band corresponding to the photorefractive excitation of electrons from donors. We can see from Section 5.3.1 that there is no apparent absorption peak due to the photorefractive excitation. Nevertheless, we experimentally found that, in terms of dynamic range and sensitivity, the optimal recording wavelength for $LiNbO_3$:Mn crystals is 458 nm among all the wavelengths of laser sources available in our lab, which include 401 nm, 458 nm, 477 nm, 488 nm, 514 nm, and 633 nm. In the following experiments of photorefractive recording, laser beams with wavelength of 458 nm are used.

Dynamic range or M/# of a holographic storage system is proportional to the maximum refractive index change, Δn_s, that can be achieved in the recording material. In transmission recording geometry using lithium niobate crystals, although the local recording speeds vary inside the crystal over the thickness because of the different recording intensities due to absorption, the saturation value of the refractive index changes Δn_s is the same for the whole crystal, if the effect of self-diffraction can be ignored during recording. Therefore, if the recording time is long enough and the recording is so stable that we can record the grating everywhere inside the crystal to saturation, we can obtain a uniform volume holographic grating. Then the maximum refractive index change can be calculated from the measured saturation value of the diffraction efficiency by

$$\eta = (1-R)^2 \exp\left(-\frac{\alpha L}{\cos\theta}\right) \sin^2\left(\frac{\Delta n \pi L}{\lambda \cos\theta}\right), \tag{5-3}$$

where R is the reflectivity, α is the intensity absorption coefficient, L is the thickness of the crystal, θ is the incident angle inside the crystal, λ is the wavelength outside the crystal, and Δn is the amplitude of refractive index change.[5-24]

Figure 5-5 shows the measured maximum refractive index change $\Delta n_{s,o}$ of several Mn-doped lithium niobate crystals with different Mn concentrations. All the crystals are in the as grown state. Ordinary polarization is used. The recording is stabilized utilizing an active feedback system.[5-25] From Figure 5-5 we can see that a linear dependence of $\Delta n_{s,o}$ on the Mn concentration is still valid even for the highly-doped crystal with a Mn concentration of $122 \times 10^{24} m^{-3}$. Considering that the highest practical concentration of iron in Fe-doped lithium niobate crystals is about $40 \times 10^{24} m^{-3}$,[5-26] it is obvious that the electron tunneling effect, which is the limiting factor for the highest practical doping level of

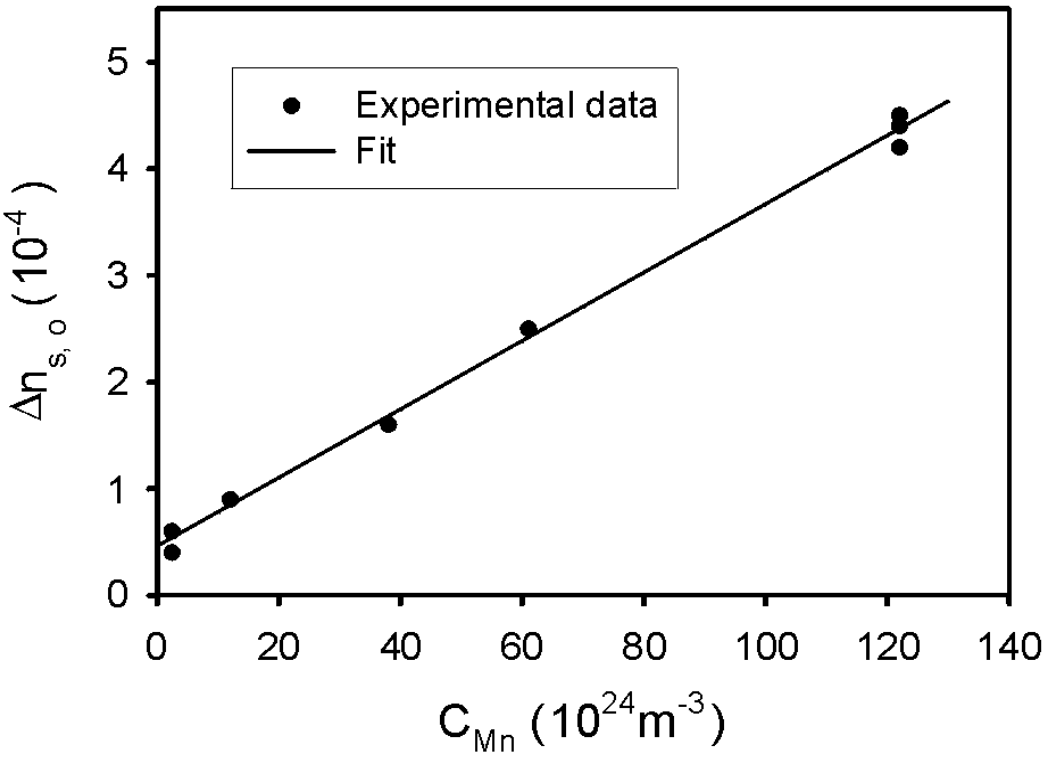

Fig. 5-5. Measured maximum refractive index change $\Delta n_{s,o}$ for several Mn-doped lithium niobate crystals with different Mn concentrations C_{Mn} (wavelength 458 nm, ordinary light polarization).

crystals, is much smaller in Mn-doped crystals than that in Fe-doped crystals. By using Mn instead of Fe as the dopant, we can increase the highest practical doping level by a factor of about 3. From Equation (4-1) we can deduce that for $V \gg E$ this yields a ratio of $(3^2)^{1/3} = 2.1$ between the heights of barriers for Mn-doped and Fe-doped crystals. This is very consistent with the ratio of the thermal activation energies of dark decay $0.52/0.28 = 1.8$ (Section 4.4.1 and 4.5.1 in Chapter 4). Notice that the magnitude of the largest Δn_s that can be obtained for Fe-doped and Mn-doped crystals are almost the same.[5-26] The reason that the maximum refractive index change in $LiNbO_3$:Mn is less than that in $LiNbO_3$:Fe with the same doping level is probably because the bulk photovoltaic coefficient of Mn is smaller than that of Fe in lithium niobate crystals.

The sensitivity is defined by Equation (5-2), that is, the initial recording slope normalized by the thickness of the crystal and the recording intensity. Figure 5-6 shows the

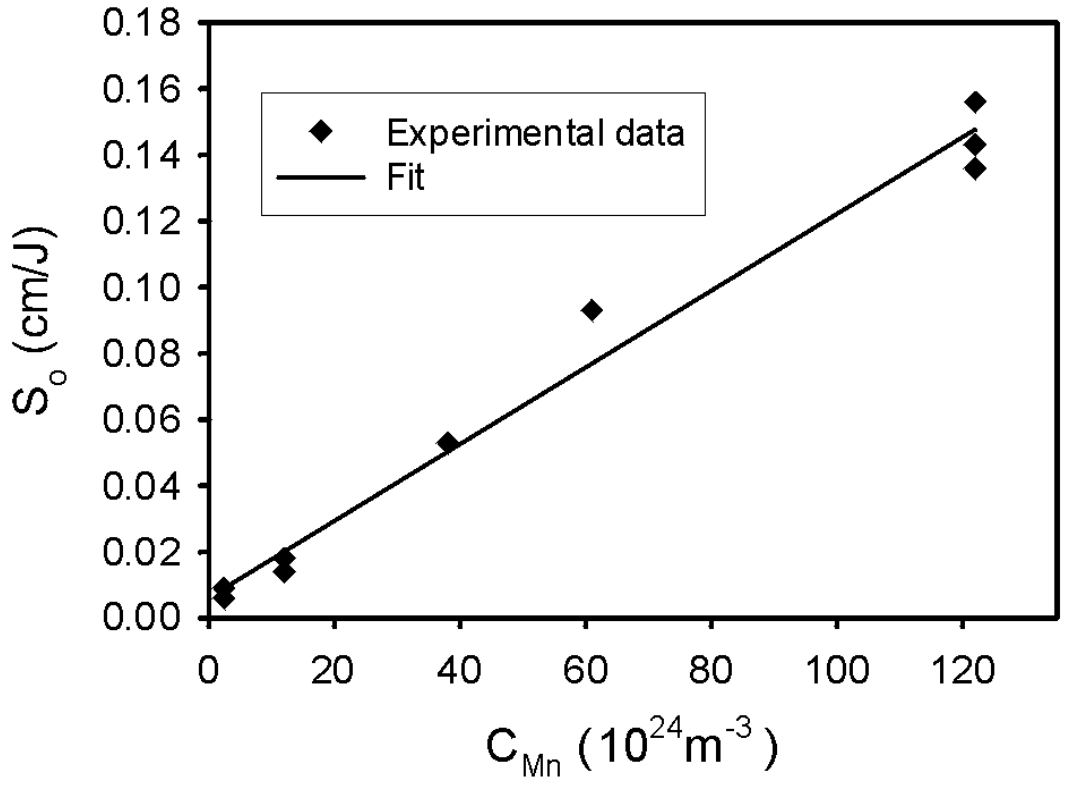

Fig. 5-6. Measured sensitivities S_o of the Mn-doped crystals with different Mn concentrations C_{Mn} for ordinary light polarization (wavelength 458 nm).

measured sensitivities of the Mn-doped crystals with different Mn concentrations for ordinary light polarization. The crystals are the same as we used for Figure 5-5. We can see that the sensitivity of Mn-doped lithium niobate crystals increases linearly with the doping level.

Δn_s is proportional to $\gamma_{eff}\, n_{eff}^3$ as

$$\Delta n_s = -\frac{1}{2}\gamma_{eff} n_{eff}^{\ 3} E_{sc}, \tag{5-4}$$

where E_{sc} is the space-charge field, γ_{eff} is the effective electro-optic coefficient, and n_{eff} is the effective refractive index.[5-27] M/# and sensitivity are proportional to Δn_s, hence M/# and sensitivity are proportional to $\gamma_{eff}\, n_{eff}^{\ 3}$. The electro-optic coefficient of $LiNbO_3$ for extraordinary light polarization is 3.2 times as large as that for ordinary light polarization. Then by using extraordinary polarization instead of ordinary polarization, we can boost M/# and sensitivity of a $LiNbO_3$-based holographic storage system by a factor of about 3. For $LiNbO_3$:Mn crystals, by using extraordinary polarization, extra gains of M/# and sensitivity will result from the large dichroism, that is, the smaller absorption coefficient for extraordinary light polarization. For example, using ordinary polarization, the measured M/# and sensitivity of one of the $LiNbO_3$:Mn crystals with a Mn concentration of $122 \times 10^{24} m^{-3}$, S4, are 1.1 and 0.2 cm/J, respectively, while using extraordinary polarization the measured M/# and sensitivity of this crystal are 7.3 and 1.3 cm/J, respectively. Both, M/# and sensitivity, gain a factor of about 6.6 for extraordinary polarization, instead of 3.

Inside the crystal the intensity is a function of depth and can be represented as:

$$I(x) = (1-R) I_0 \exp(-\alpha x / \cos\theta), \tag{5-5}$$

where R is the reflectivity, I_0 is the incident intensity outside the crystal, α is the absorption coefficient, x is the depth, and θ is the incident angle inside the crystal. The recording time constant τ is inversely proportional to the recording intensity, therefore the local grating strength during recording can be represented as a function of time and depth as following:

$$A(x) = A_0[1 - \exp(-t/\tau)] = A_0\{1 - \exp[-ctI(x)]\}, \tag{5-6}$$

where c is some constant. The initial recording slope can be calculated as:

$$\left.\frac{d\sqrt{\eta}}{dt}\right|_{t=0} = \exp\left(\frac{-\alpha L}{2\cos\theta}\right) \times \frac{d}{dt}\left(\int_0^L A(x)dx\right)\Big|_{t=0} \quad . \tag{5-7}$$
$$\propto \frac{\exp(-\alpha L/2\cos\theta) - \exp(-3\alpha L/2\cos\theta)}{\alpha}$$

For the crystal for which we measured M/# and sensitivity using both, ordinary and extraordinary polarization, S4, the thickness L is 0.84mm and the absorption coefficient for ordinary and extraordinary polarization are $20.9\,cm^{-1}$ and $11.4\,cm^{-1}$, respectively. Calculated from Equation (5-7), the factor of gain on M/# and sensitivity due to the dichroism of this crystal is 2.0. Multiplying this value with the ratio between the factor $\gamma_{eff}\, n_{eff}^3$ of extraordinary and ordinary polarizations, 3, gives us the theoretical factor of gains on M/# and sensitivity using extraordinary light polarization as 6, which agrees with the experimental result very well.

Another advantage that we found in manganese-doped lithium niobate crystals for holographic storage is the excellent recording repeatability, even without an active stabilization of the setup. The good repeatability and stability of recording in $LiNbO_3$:Mn crystals probably come from the high sensitivity and low holographic scattering.

The oxidation state of $LiNbO_3$ crystals can be changed by annealing at elevated temperature in appropriate atmosphere, typically oxygen for oxidation and argon for reduction. It's well known that M/# and sensitivity in $LiNbO_3$:Fe crystals are strong functions of the oxidation state. Typically, the more the crystal is reduced, the larger the sensitivity and the smaller the M/#, and vice versa. In Ref. 5-2 we reported the measured M/# and sensitivity in a $LiNbO_3$ crystal doped with 0.2 atomic% Mn with different oxidation states. We

found that the measured sensitivity in that sample is 0.5 cm/J and almost independent of the annealing state, while the M/# drops by a factor of 15 from the highly-oxidized to the highly-reduced state. Figure 5-7 shows the measured maximum refractive index change for ordinary polarization in the $LiNbO_3$ crystals doped with 0.2 atomic % Mn and with 0.5 wt % $MnCO_3$ having different oxidation states. We also measured the M/# and sensitivity of the highly doped $LiNbO_3$ crystal that contains 0.5 wt % $MnCO_3$ having different oxidation states using extraordinary light polarization. The thickness of the crystal is 0.84 mm. From the highly reduced to the highly oxidized state, the M/# increases from 4.5 to 7.3, while the measured sensitivity increases from 0.8 cm/J to 1.3 cm/J, that is, the more oxidized the crystal, the larger M/# and sensitivity we obtained. In the crystals with doping levels 0.2 atomic % Mn or 0.5 wt % $MnCO_3$, the optimal oxidation states in terms of both, M/# and sensitivity, are highly oxidized. The lack of the trade-off between M/# and sensitivity is good for, e.g., holographic storage systems.

In the one-center model for $LiNbO_3$:Mn, Mn^{2+} sites act as filled traps and electrons can be optically excited from Mn^{2+} sites to the conduction band. Mn^{3+} sites act as empty traps with which electrons in the conduction band can recombine. In all experiments, we use transmission geometry, for which the grating vector K is small and we would expect that

$$E_q \gg E_{ph} \gg E_d , \tag{5-8}$$

where the saturation field E_q, the photovoltaic field E_{ph}, and the diffusion field E_d are given by Equation (2-9), (2-10) and (2-11). Under these conditions, combining Equations (2-7)-(2-11) and

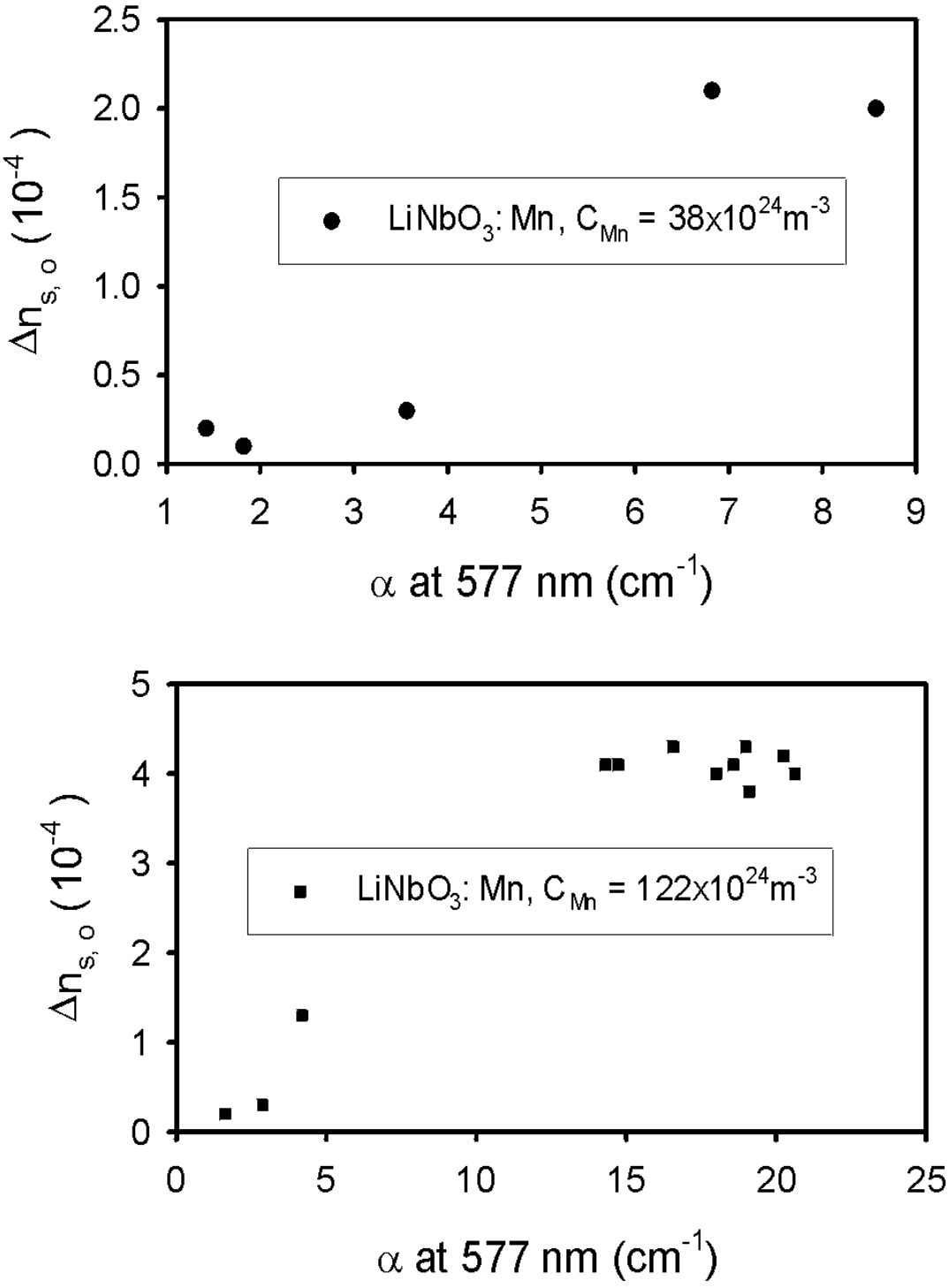

Fig. 5-7. Measured maximum refractive index change $\Delta n_{s,o}$ for ordinary light polarization in the $LiNbO_3$ crystals doped with 0.2 atomic% Mn and with 0.5 wt% $MnCO_3$ for different oxidation states that are quantified by the absorption coefficient at 577 nm.

$$\tau_e \cong \tau_{di} \equiv \frac{\varepsilon}{q\mu s I_0 (N_D - N_A)} \frac{\gamma_A N_A}{}, \tag{5-9}$$

we obtain:

$$M/\# \propto E_{sc} = E_q \frac{\sqrt{E_d^2 + E_{ph}^2}}{E_d + E_q} \cong E_{ph} \equiv \frac{p\gamma_A N_A}{q\mu s} \propto N_A, \tag{5-10}$$

$$S \propto \frac{M/\#}{\tau_e} \propto \frac{E_{ph}}{\tau_e} = \frac{pI_0(N_D - N_A)}{\varepsilon} \propto N_D - N_A. \tag{5-11}$$

One way to check the validity of conditions in Equation (5-8) is to record holograms with different grating vector or period length. The grating period in transmission geometry can be varied by changing the outside angle between the recording beams. Since the bulk photovoltaic field E_{ph} is independent of the grating period(Equation (2-10)), if the conditions in Equation (5-8) are valid, then the recording curves with different grating periods should not be different. Figure 5-8 shows two recording curves in sample S4 with different grating periods. We can see that those two recording curves are almost overlapped. This means that for $LiNbO_3$:Mn crystals in transmission geometry, it is the photovoltaic current that dominates the photorefractive effect and the M/# is proportional to the photovoltaic field E_{ph}.

5.4 Discussions

In the previous chapter we have experimentally shown that $LiNbO_3$:Mn crystals are highly suited for holographic storage. In order to tailor the material properties for holographic applications, a quantitative description of the photorefractive properties is needed. First, we will discuss the dominant charge driving force. Then we will concentrate on a

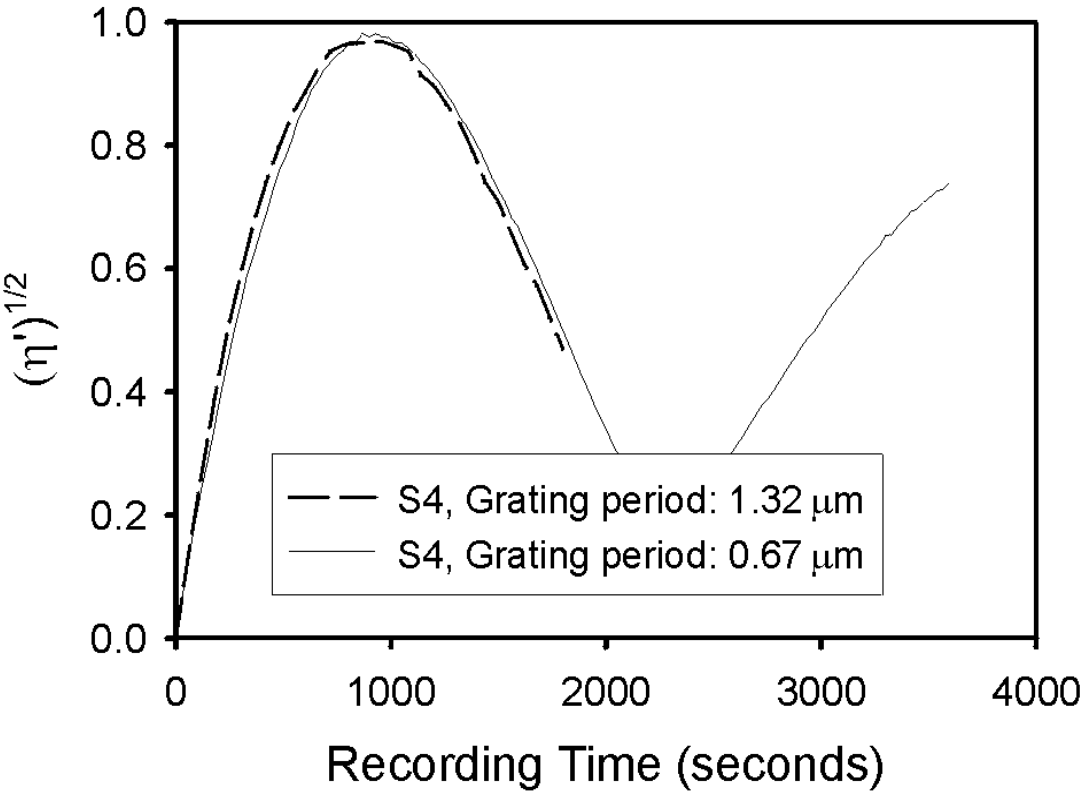

Fig. 5-8. Diffraction efficiency vs. time for recording of two gratings under identical conditions, except that the period length of the grating differs by a factor of 2 (wavelength 458 nm, extraordinary light polarization).

charge transport model for the crystals that are doped with up to 0.2 wt% MnO. Finally, we will discuss the behavior of crystals with higher doping levels.

5.4.1 Dominant charge driving force

For the case that the bulk photovoltaic effect is the dominant charge driving force, M/#, sensitivity, and also the temporal evolution of refractive--index changes and diffraction efficiencies should not depend on the period length of the grating. As Figure 5-8 shows, this is indeed the case. Furthermore, we have not seen any experimental evidence for space charge limiting effects. E.g., the curves in Figure 5-8 are identical because of lack

of space charge limitation. Thus, as we have already written it in Equation (5-10), the saturation space charge field E_{sc} should be equal to E_{ph}.

5.4.2 Charge transport model

Because the samples are doped with Mn, it is evident that Mn will be the dominant photorefractive center. It is known, that Mn occurs in $LiNbO_3$ in the valence states 2+ and 3+.[5-7] As we already pointed out, the results can be explained within a $Mn^{2+/3+}$ one-center charge transport model, assuming that the Mn centers are almost completely filled with electrons, i.e., $C_{Mn^{2+}} >> C_{Mn^{3+}}$.[5-2] This explains that on the one hand the M/# increases and on the other hand the sensitivity stays constant if one oxidizes the crystals (see Equation (5-10) and Equation (5-11)), because the M/# is proportional to $C_{Mn^{3+}}$ while the sensitivity is proportional to $C_{Mn^{2+}} = C_{Mn} - C_{Mn^{3+}}$. During oxidization $C_{Mn^{3+}}$ increases, but the much larger $C_{Mn^{2+}}$ stays almost constant.

We are now able to perform two quantitative tests of this model: Equation (2-10) in Chapter 2 yields

$$N_A = \frac{q\mu s E_{ph}}{p\gamma_A}. \tag{5-12}$$

We will do this for the oxidized crystal that contains $38 \times 10^{24} m^{-3}$ Mn (see Figure 5-7). Here we get a $\Delta n_{s,o}$ of 2.0×10^{-4}. With Equation (5-4) and with γ_{eff} = 12 pm/V and $n_{eff} = 2.35$ we get $E_{sc} = 2.6 \times 10^6$ V/m. All other parameters of the above mentioned equation to calculate N_A are available from literature.[5-28][5-29] However, in the referenced paper the parameters s and p were determined for light of the wavelength 366 nm. Anyhow, other authors showed before that the ratio s/p is reduced by only a factor of 2 if one moves from 366 nm to 458 nm.[5-7] Thus we end up with q = 1.6×10^{-19} As, μ = 7.4×10^{-5} m^2/

(Vs), $s/p = 1.6\times10^{27}$ V/(Jm), and $r_A = 2.4\times10^{-13}$ m^3/s. Plugging in the numbers yields $C_{Mn^{3+}} = N_A = 0.2 \times 10^{24} m^{-3}$. This is much less than $C_{Mn} = 38 \times 10^{24} m^{-3}$, verifying the statement $C_{Mn^{2+}} >> C_{Mn^{3+}}$. Anyhow, $C_{Mn^{3+}}$ is still large enough to avoid space--charge limiting effects. Calculation of E_q yields 20×10^6 V/m for a 1 µm period length of the grating.

The second test is the calculation of the absorption cross section at 458 nm. The crystal that is doped with $78 \times 10^{24} m^{-3}$ Mn (0.5 wt% $MnCO_3$) has at 458 nm an absorption of $\alpha = 2000\,m^{-1}$. Considering that $\alpha = s_{abs} C_{Mn^{2+}}$, we get for $C_{Mn^{2+}} \cong C_{Mn}$ the result $s_{abs} = 2.6 \times 10^{-23} m^2$. The photon absorption cross sections s_{abs} and s are related through $s = Qs_{abs}$, where Q is the quantum efficiency for excitation of an electron upon absorption of a photon. A typical value for this Q is 0.05.[5-30][5-31] Thus we end up with $s = 1.3 \times 10^{-24} m^2$. From spectroscopic investigations it is furthermore known that moving from 458 nm to 366 nm, the absorption cross section increases roughly by a factor of 10.[5-7] This yields $s = 1.3 \times 10^{-23} m^2$. From an independent investigation the value for s for this wavelength is known,[5-7] s was determined to be $1.9 \times 10^{-23} m^2$. Considering all uncertainties, this agreement is very good and indicates that the assumption $C_{Mn^{2+}} \cong C_{Mn}$ is valid.

The concentration ratio $C_{Mn^{2+}}/C_{Mn^{3+}}$ should, in analogy to $LiNbO_3$:Fe, not depend much on the overall doping level for as--grown crystals. Thus it is clear that both, $\Delta n_{s,o} \sim C_{Mn^{3+}}$ and $S \sim C_{Mn^{2+}}$, should grow linearly with the overall Mn concentration C_{Mn}. This is nicely confirmed by the data shown in the Figure 5-5 and Figure 5-67.

5.4.3 Calibration of the concentrations

The insights presented above allow now for everyone to quantify the Mn^{2+} and the Mn^{3+} concentrations if the following information is available: Mn concentration in the melt, and absorption coefficient $\alpha_{577\,nm,o}$ for ordinary light polarization at 577 nm.

The Mn concentration C_{Mn} in the crystal is identical to the Mn concentration in the melt, because we have proved that the distribution coefficient is one. The Mn^{2+} concentration is even after strong oxidization still in very good approximation given by $C_{Mn^{2+}} = C_{Mn}$. And the Mn^{3+} concentration can be deduced from the absorption band that is due to crystal field transition. In the above mentioned example we calculated $C_{Mn^{3+}} = 0.2 \times 10^{24}\,m^{-3}$. This crystal has an $\alpha_{577\,nm,o}$ of $2000\,m^{-1}$ thus yielding the relation $C_{Mn^{3+}} = 1 \times 10^{20}\,m^{-2} \times \alpha_{577\,nm,\,o}$.

5.4.4 Tailoring of crystal properties

The two key-properties are dynamic range and sensitivity. However, there are trade--offs with other properties such as absorption and dark decay. In general, on the one hand the doping level should be large enough and the crystal should be oxidized enough to satisfy the dynamic range and sensitivity requirements, but on the other hand it should not be doped or oxidized more than necessary to avoid absorption and accelerated dark decay. As a consequence, for particular applications that require special dynamic range and sensitivity, one needs to know which concentration and annealing state must be selected. With the experimental data provided in this paper and with the concentration calibrations presented above, this is possible:

The M/# is given by $M/\# = 4.5 \times 10^{-22} m^{-3} \times C_{Mn^{3+}}$ per cm and the sensitivity is $S = 1.25 \times 10^{-26} m^{-3} \times C_{Mn^{2+}}$ in cm/J for wavelength 458 nm and extraordinary light polarization.

5.4.5 Behavior of highly-doped crystals

All experimental data that is obtained with the crystals that are doped with up to 0.2 wt% MnO ($78 \times 10^{24} m^{-3}$) can be explained and understood within the one-center $Mn^{2+/3+}$ charge transport model. However, for crystals with doping levels of 0.5 wt% $MnCO_3$ ($122 \times 10^{24} m^{-3}$) deviations are observed. E.g., the sensitivity increases from 0.8 to 1.3 cm/J for oxidation of the crystal, although we would expect that the sensitivity stays constant. So far, we can only speculate where this comes from. The concentration where the deviation from the one--center behavior starts is the same where the tunneling dark decay mechanism becomes to be present. This may impact the results. Furthermore, for high doping levels it is possible that Mn occupies different lattice sites or that Mn occurs in more than two valence states. Only additional measurements, e.g. with electron paramagnetic resonance, can clarify the situation in theses crystals.

5.5 Conclusions

In conclusion, we have shown that $LiNbO_3$:Mn crystals are very promising for holographic recording. The distribution coefficient of Mn-doped lithium niobate crystal has been determined to be around 1. The effect of dark decay due to electron tunneling, which is the limiting factor for the highest practical doping level, is in $LiNbO_3$:Mn less than in $LiNbO_3$:Fe, and higher doping levels can be used in $LiNbO_3$:Mn to achieve larger dynamic range and sensitivity for holographic applications. The highest practical doping

level in $LiNbO_3$:Mn has been found to be around 0.5 wt% $MnCO_3$, and refractive index changes and sensitivities up to 1.5×10^{-3} and 1.4 cm/J are measured for extraordinarily polarized light of the wavelength 458 nm. It has been found that in terms of both, dynamic range (or refractive index change) and sensitivity, the optimal oxidation state is highly oxidized. The material is highly suited for holographic recording using blue light with extraordinary polarization because of a fast response, and low absorption. Furthermore, the hologram quality is outstanding because holographic scattering is much weaker compared to that in, e.g., iron-doped lithium niobate. Thermal fixing has been successfully demonstrated in $LiNbO_3$:Mn crystals.

References

[5-1] Y. Yang, I. Nee, K. Buse, and D. Psaltis, "Ionic and electronic dark decay of holograms in $LiNbO_3$: Fe crystals", Appl. Phys. Lett. **78**, 4076-4078 (2001).

[5-2] Y. Yang, K. Buse, and D. Psaltis, "Photorefractive recording in $LiNbO_3$:Mn," Opt. Lett. **27**, 158-160 (2002).

[5-3] H. J. Coufal, D. Psaltis and G. T. Sincerbox, *Holographic Data Storage*, Springer 2000.

[5-4] D. Psaltis and F. Mok, "Holographic memories," Sci. Am. **273,** 70-76 (1995).

[5-5] B. Dischler, J. R. Herrington, and A. Rauber, "Correlation of the photorefractive sensitivity in doped $LiNbO_3$ with chemically induced changes in the optical absorption spectra," Solid State Comm. **14**, 1233-1236 (1974).

[5-6] N. N. Sorota and V. P. Yarunichev, "Absorption spectrum of lithium niobate with transition metal impurities in the region 0.3-2.0 μ," J. Appl. Spectrosc. **25**, 1259-1261 (1976).

[5-7] E. Kratzig and H. Kurz, "Photo-induced currents and voltages in $LiNbO_3$," Ferroelectrics **13**, 295-296 (1976).

[5-8] L. Arizmendi, J. M. Cabrera, and F. Agullo-Lopez, "Defects induced in pure and doped $LiNbO_3$ by irradiation and thermal reduction," J. Phys. C: Solid State Phys. **17**, 515-529 (1984).

[5-9] O. Thiemann and O. F. Schirmer, "Energy levels of several 3d impurities and EPR of Ti^{3+} in $LiNbO_3$," SPIE **1018**, 18-22 (1988).

[5-10] A. Adibi, K. Buse, and D. Psaltis, "Two-center holographic recording," J. Opt. Soc. Am. **B 18**, 584-601 (2001).

[5-11] N. V. Kukhtarev, V. B. Markov, S. G. Odoulo, M. S. Soskin, and V. L. Vinetskii, "Holographic storage in electrooptic crystals. I. Steady state," Ferroelctrics **22**, 949-960 (1979).

[5-12] E. Kratzig, "Photorefractive effects and photoconductivity in $LiNbO_3$-Fe," Ferroelectrics **21**, 635-636 (1978).

[5-13] E. Kratzig and R. Orlowski, "Light-induced charge transport in doped LiNbO3 and LiTaO3," Ferroelectrics **27**, 241-244 (1980).

[5-14] K. Buse, "Light-induced charge transport processes in photorefractive crystals I: Models and experimental methods," Appl. Phys. B **64**, 273-291 (1997).

[5-15] K. Buse, "Light-induced charge transport processes in photorefractive crystals II: Materials," Appl. Phys. B **64**, 391-407 (1997).

[5-16] B. A. Wechsler and M. B.Klein, "Thermodynamic point-defect model of barium-titanate and application to the photorefractive effect," J. Opt. Soc. Am. **B 5**, 1711-1723 (1988).

[5-17] E. Possenriede, P. Jocos, H. Krose, and O. F. Schirmer, "Paramagnetic defects in $BaTiO_3$ and their role in light-induced charge transport - optical studies," Appl. Phys. **A 33**, 73-81 (1992).

[5-18] R. N. Schwartz and B. A. Wechsler, "Electron-paramagnetic-resonance study of transition-metal-doped BaTiO3 - effect of material processing on fermi-level position," Phys. Rew. **B 48**, 7057-7069 (1993).

[5-19] K. Buse and E, Kratzig, "3-valence charge-transport model for explanation of the photorefractive effect," Appl. Phys. **B 61**, 27-32 (1995).

[5-20] R. Verma, J. Arunachalam, S. Gangadharan, J. C. Vyas, G. P. Kothiyal, and M. K. Gupta, "Trace characterization of lithium niobate by neutron activation analysis," Fresenius Journal of Analytical Chemistry **344**, 261-264 (1992).

[5-21] G. Anil, M., Ramanaji, M. R. P. Reddy, A. Kumar, T. L. Prakash, and V. C. Sethi, "ICP-OES determination of Ta, Nb, Fe, Ti, Sn, Mn, and W in Indian tantalite-niobate ore concentration using microwave digestion," Atomic Spectroscopy **23**, 32-35 (2002).

[5-22] R. G. Smith, D. B. Fraser, R. T. Denton, and T. C. Rich, "Correlation of reduction in optically induced refractive index inhomogeneity with OH content in $LiTaO_3$ and $LiNbO_3$," J. Appl. Phys. **39**, 4600-4602 (1968).

[5-23] H. J. Reyher, R. Schulz, and O. Thiemann, "Investigation of the optical absorption bands of Nb^{4+} and Ti^{3+} in lithium niobate using magnetic circular-dichroism and optically detected magnetic resonance techniques," Phys. Rev. B **50**, 3609-3619 (1994).

[5-24] H. Kogelnik, "Coupled wave theory for thick hologram gratings," The Bell System Technical Journal **48**, 2909-2957 (1969).

[5-25] S. Breer, K. Buse, K. Peithmann, H. Vogt, and E. Kratzig, "Stabilized recording and thermal fixing of holograms in photorefractive lithium niobate crystals," Rev. Sci. Instr. **69**, 1591-1594 (1998).

[5-26] K. Peithmann, A. Wiebrock, and K. Buse, "Photorefractive properties of highly-doped lithium niobate crystals in the visible and near-infrared," Appl. Phys. B **68**, 777-784 (1999).

[5-27] P. Yeh, *Introduction to Photorefractive Nonlinear Optics*, John Wiley & Sons, Inc. 1993.

[5-28] G. C. Valley, "Erase rates in photorefractive material with 2 photorefractive species," Appl. Opt. **22**, 3160-3164 (1983).

[5-29] A. Adibi, K. Buse, and D. Psaltis, "Two-center holographic recording," J. Opt. Soc. Am. **B 18**, 584-601 (2001).

[5-30] W. Philips and D. L. Staebler, "Control of the Fe^{2+} concentration in iron-doped lithium niobate," J. Electr. Materials **3**, 601-617 (1974).

[5-31] K. Buse, A. Gerwens, S. Wevering, and E. Kratzig, "Charge-transport parameters of photorefractive strontium-barium niobate crystals doped with cerium," J. Opt. Soc. Am. B **15**, 1674-1677 (1998).